HARVARD
Kenneth C. Griffin

GRADUATE SCHOOL
OF ARTS AND SCIENCES

DISSERTATION ACCEPTANCE CERTIFICATE

The undersigned, appointed by the

Department of Chemistry & Chemical Biology

have examined a dissertation entitled:

Methods and tool development for robust biological voltage imaging

presented by: Frederick Phillips Brooks III

candidate for the degree of Doctor of Philosophy and hereby certify that it is worthy of acceptance.

Signature Adam E Cohen

Typed name: Professor Adam Cohen

Signature Hongkun Park

Typed name: Professor Hongkun Park

Signature Conor Evans

Typed name: Professor Conor Evans

Date: 7 May 2024

Methods and tool development for robust biological voltage imaging

A DISSERTATION PRESENTED
BY
FREDERICK PHILLIPS BROOKS III
TO
THE DEPARTMENT OF CHEMISTRY AND CHEMICAL BIOLOGY

IN PARTIAL FULFILLMENT OF THE REQUIREMENTS
FOR THE DEGREE OF
DOCTOR OF PHILOSOPHY
IN THE SUBJECT OF
CHEMISTRY

HARVARD UNIVERSITY
CAMBRIDGE, MASSACHUSETTS
MAY 2024

Dissertation Advisor: Professor Adam E. Cohen Frederick Phillips Brooks III

Methods and tool development for robust biological voltage imaging

Abstract

Electrical potential differences across membranes play important roles throughout biology, particularly in the brain, where propagating electrical waves called action potentials and smaller subthreshold perturbations carry information within neurons. These electrical signals can be measured at tissue-scale resolution by external electrodes or at a higher resolution by electrodes inserted into the brain. For the highest resolution measurements that avoid many of the problems associated with electrode insertion into the brain, the use of dyes or proteins that transduce the electrical signal into an optical readout is a rapidly maturing technique. While voltage imaging has already enabled significant scientific advances, I address in this dissertation several barriers that have stood in the way of broader use of voltage imaging.

First, I worked to overcome the loss of voltage sensitivity under two-photon imaging conditions hitherto seen in microbial rhodopsin voltage indicators. This class of genetically encoded voltage indicators (GEVIs) provides superior response kinetics under one-photon conditions but loses sensitivity under two-photon conditions. I experimentally characterized the photocycle of the Förster resonance energy transfer (FRET)-opsin GEVIs, Voltron1 and Voltron2, and used the results of these experiments to rationally design two-photon imaging conditions that restored voltage sensitivity. I demonstrated this technique for two-photon voltage imaging with Voltron2 in barrel cortex of a live mouse. These results open the door to high-speed two-photon voltage imaging of FRET-opsin

GEVIs *in vivo* and provide insight into the reporters' photocycle that is useful both for robust one-photon imaging and for future development of two-photon-optimized rhodopsin-based GEVIs.

Second, I bring together experimental and theoretical work to provide a set of well-characterized upper bounds to two-photon voltage imaging performance *in vivo*. While aspects of this have previously been addressed, there has not been a single work addressing these various limits with a specific focus on two-photon voltage imaging. As voltage imaging operates under different constraints than other more familiar types of functional imaging, this treatment is necessary to set realistic expectations, delineate the most productive avenues for optimization, and provide a common theoretical groundwork for comparing voltage imaging performance. Among other conclusions, we found that current technologies are limited to high quality imaging of <12 neurons under standard conditions at depths greater than 300μm *in vivo*.

Third, I present Luminos, an open-source MATLAB-based software package for highly synchronized control of high-speed microscopes. The distinct constraints of voltage imaging place distinct constraints on the required instrumentation. Existing general-purpose control libraries are inadequate for the speed and synchronization required for voltage imaging experiments involving complex electrical and optical stimulation and recording. Rather than produce control code narrowly-tailored to a specific microscope or experiment, our lab embarked on a project to develop a modular customizable control suite that is now used for data acquisition on all of the seven custom microscopes in our lab and has been publicly released with the aim of making voltage imaging instrumentation more accessible to the broader field.

Fourth, I performed a theoretical and experimental treatment of the calibration of intensity-based voltage indicators to an absolute voltage scale. Because of unknown expression levels, background, optical efficiency, and other factors, intensity-based imaging of a single reporter provides only relative signals that cannot be calibrated either to an external scale or across significant spatial or temporal extent. I mathematically and experimentally analyzed the feasibility of calibrating voltage

responses with a second independently expressed voltage indicator and found that a combination of a linear indicator with a nonlinear indicator tailored to the voltage range of interest can provide a resilient calibration to an absolute scale. Likely due to a publication bias towards reporting more linear indicators, high-performance nonlinear indicators are not currently available, but this theoretical treatment motivates their development and dissemination.

Finally, I discuss the technical outlook for voltage imaging in light of this work. By characterizing the performance limits of two-photon voltage imaging, uncovering the mechanism of two-photon voltage insensitivity in opsin-GEVIs, and proposing a method for dual indicator absolute voltage imaging, I provide insight into the most productive directions for future voltage indicator development. Both the demonstration of two-photon voltage imaging with Voltron2 and the release of the Luminos software are important steps towards making voltage imaging more broadly useful and accessible. Important work remains in further optimizing opsin-GEVIs for two-photon imaging and in making voltage imaging hardware more accessible.

Contents

List of figures

List of Tables

Quid habes quod non accepisti?

Acknowledgments

> *Unless the Lord builds the house, those who build it labor in vain. Unless the Lord watches over the city, the watchman stays awake in vain. It is in vain that you rise up early and go late to rest, eating the bread of anxious toil; for he gives to his beloved sleep.*
>
> **— Psalm 127:1-2 (ESV)**

I thank my Lord and Savior, Jesus, without whom all of this would be in vain. I thank him for giving me this work to do, surrounding me with the blessings of family, friends, and co-workers, and letting this time bear fruit in various ways.

Second only to God, I thank my lovely wife, Paula Brooks, PhD., who not only supported me emotionally and spiritually, put up with late nights of work, took the lead in caring for our daughters, and kept me fueled with nutritious food, but even typeset this entire dissertation in LaTeX! Overqualified, perhaps, but you could never be over-appreciated.

I also acknowledge my two beautiful daughters, Maria Andrea and Elizabeth Ann. You may not have contributed directly to my work, but your smiles and sweet times gave me the motivation I needed to make it to the finish line.

My deepest thanks go to my advisor, Adam Cohen. Your commitment to personally guiding each one of your trainees, holding our research to the highest standards of creative excellence, and pulling together a group of top-notch researchers who are also great people has made my time in your lab a more powerful shaping experience than I would have imagined when I entered. Was it harder than I expected? Yes. But with your help, guidance, and patience, I hope I have grown as a scientist and as a person in ways that will shape the rest of my life.

I also thank Hunter Davis, who, as a postdoc in the lab, was an irreplaceable mentor and friend. Your contribution to my PhD. went well beyond what is reflected in the author lists as you encouraged me in frustration and celebrated with me in success. Very little of this dissertation would have happened without you.

I also thank the professors who have helped improve my research by serving on my thesis committee (Hongkun Park and Conor Evans) and my qualifying examination committee (Hongkun Park, Kang-Kuen Ni, and Eric Heller).

I thank my parents, Roger and Ann Brooks, for the grounding in hard work, education, and Christianity that they gave me as a child and for the continued interest in my work and support in rough times of parenting and research. Thank you also to my parents-in-law, Omar and Maria Pacheco, for their support for me and my family.

I acknowledge my grandfather and namesake, Fred Brooks, Jr. I may not have followed his advice to write something towards my dissertation every day, but the knowledge that he had completed his PhD. on this same campus was a small inspiration to keep me working. More than that, I hope I may follow his example of a life lived for Christ whatever the context.

I thank my colleagues in the Cohen lab for the interesting scientific (and nonscientific) discussions, the countless hours of help and advice, and the treats left by the M112 fridge. Special thanks to the Spiking HEKs volleyball team for a fabulous summer of having fun!

I also thank Dave Song for encouraging me and giving me tips about how to apply for jobs, write a dissertation, and defend as we walked through those processes together. Go RNR! Thank you also to the rest of the Christians in CCB for your encouragement and prayer in our monthly meetings.

I am particularly grateful for the mentorship and encouragement in teaching that Lu Wang (PS11, PS10) and Khaled Abdelazim (Chem 160) offered, not only while I was teaching with them, but also afterwards. Working in the classroom with them developed both my love of teaching and my practical teaching skills. I look forward to putting these both to good use in my next job.

I thank my undergraduate advisor, Nozomi Ando, and my graduate student mentor, William Thomas, for giving me a first taste of exciting and difficult research. The lessons in washing glassware and pipetting will not be forgotten; nor, I hope, will the lessons in doing and communicating science.

I also thank all of my former professors and teachers who taught me not only a whole lot of facts, but also taught me how to think and work hard and gave me a love of teaching. Special thanks go to Michael Kelly at Princeton who has become a friend and remained a mentor in my teaching endeavors.

Thank you to all of our friends at Beacon Community Church for your support and encouragement in life and work for the past five years. We are glad we get to stay with you for the next chapter of life.

I thank the Mustard Seed Foundation for generous financial and community support through the Harvey Fellowship.

1

Introduction

Just as the diffusion and transport of small molecules and atoms can communicate information within and between cells, the propagation of electric potential differences along membranes is also a critical component of biological information flow. In neurons, electrical action potentials [1] and smaller sub-threshold voltage perturbations [2] are the primary high-speed carriers of information within the cell; electrical signals control and synchronize the action of muscles throughout the body [3]; and there is increasing evidence that membrane potential plays an important role both in co-

ordinating eukaryotic cell development and differentiation[4] and in microbiology[5]. These biological voltages are of interest to neuroscientists, physiologists, developmental biologists, and microbiologists.

The measurement of biological voltages requires fundamentally different techniques than the more common measurements of small molecules. At low resolution, the electric and magnetic fields created by large numbers of neurons firing synchronous action potentials can be detected outside the skull by electro-encephalography[6] and magneto-encephalography[7]. At higher resolution, microelectrodes[8,9] can be inserted into the brain to measure the extracellular electric fields that result when current rushes into a neuron during an action potential, though these measurements face difficulties in unmixing the signals from adjacent cells[10]. In order to measure the full spectrum of electrical activity within a cell, including sub-threshold perturbations that do not result in an action potential, electrodes that provide internal access to the cell must be used. Whole-cell patch clamping[11], the gold standard for electrophysiological measurements, is severely throughput-limited, while silicon-based intracellular nano-electrode arrays suitable for *in vivo* use are still the subject of active research.[12–14] All techniques that rely on insertion of solid electrodes face challenges of tissue damage upon insertion, motion-induced damage, and immune response to the electrodes.[8]

The challenges of electrode-based recording, in contrast to the relative ease of optical imaging of ions and small molecules, have inspired the development of transducers that convert biological membrane voltage into an optical signal. Optical imaging is not without its own set of limitations. Imaging depth is limited in scattering tissue, imaging time is often limited by photobleaching and phototoxicity, introducing optical voltage reporters requires either genetic or chemical modification of the sample, imaging requires bulky and expensive equipment, and imaging techniques often produce large volumes of data that present storage and analysis challenges. Yet optical voltage sensors provide a set of capabilities that are difficult or impossible to achieve with electrode-based techniques and therefore will increasingly be a powerful complement to traditional electrophysiology.

Alone, and in combination with channelrhodopsins[15], which transduce optical signals into membrane voltage perturbations, these optical voltage sensors have already enabled significant advances in neuroscience[16–21], developmental biology[22], cancer biology[23], and pharmacological screening[24], and form the basis for a rapidly expanding field[25,26]. Nevertheless, though the field of voltage imaging is no longer in its infancy, it is by no means mature. The aim of this dissertation is to develop methods and tools that will make voltage imaging more accessible to the broader scientific community.

1.1 A classification of optical voltage sensors

The two main classes of optical voltage reporters are voltage sensitive dyes and genetically encoded voltage indicators (GEVIs). Voltage sensitive dyes have very good photophysical properties and are simple to use but, without some genetically-targeted component, label all cells to which they are exposed, leading to excessive fluorescent background[27] and preventing targeting towards a specific neuronal subtype in the brain[28]. Voltage sensitive dyes can also be somewhat toxic and difficult to deliver past the blood-brain barrier into the brain.[29] Genetically encoded voltage indicators[30–34] allow precise genetic targeting of expression and are amenable to sparse expression via adeno-associated viral delivery[35], increasing their signal to background ratio. These properties are particularly advantageous in the dense and highly complex tissue of the brain.

Modern GEVIs can be divided into two classes based on the nature of their voltage sensitive domain. The class of Voltage-sensing domain (VSD) GEVIs transduce a voltage-responsive shift in a positively charged transmembrane helix into a fluorescent readout, through environmentally-sensitive fluorescence[36], Förster resonance energy transfer (FRET)[37], or disruption of the chromophore of a circularly permuted fluorescent protein[38]. This class has historically been limited by the slow kinetics of the mechanical signal transduction, but recently developed members, such as

JEDI-2P[38], show kinetics almost as fast as the second class. In addition, VSD-based GEVIs have historically been spectrally limited by the available fluorescent proteins, restricting their usage in the biologically advantageous red end of the visible spectrum, where scattering and hemoglobin absorption are smaller. Red VSD-GEVI imaging can be performed with a recently demonstrated chemigenetic VSD-GEVI, HASAP[39], which uses an environmentally sensitive dye bound to a Voltage-sensing domain, but this indicator requires the use of dyes with poor bioavailability *in vivo*.

Rhodopsin-based GEVIs are based on retinal-containing microbial rhodopsins, natural light-driven proton pumps whose absorption spectrum shifts based on the protonation of the retinal Schiff base.[40] A mutation of an aspartate residue to asparagine blocks the proton pumping pathway, allowing the rhodopsin to function as a pure sensor.[41] Early opsin GEVIs used intrinsic retinal fluorescence as the readout, but were limited by the low fluorescence quantum yield. The development of electrochromic FRET-opsin GEVIs, in which the voltage-sensitive retinal absorption shift causes variable quenching of a FRET donor, allowed voltage sensing with the brightness of common fluorescent proteins and the speed of the voltage sensitive opsin[42]. A subset of these FRET-opsin GEVIs are the chemigenetic indicators, such as the Voltron family[43,44], which provide even greater brightness and photostability by using a synthetic dye bound to a bio-orthogonal tag as the FRET donor. Some of these dyes can cross the blood-brain barrier, allowing for easy delivery via retro-orbital injection. These chemigenetic FRET-opsin GEVIs are the current state-of-the-art, allowing for subcellular neural recording[45,46] and promising simultaneous high-resolution recording from hundreds of neurons on the surface of live mouse brain.

1.2 The state-of-the-art in calcium imaging

To fully understand the promise and challenges of biological voltage imaging, it is useful to consider the current state-of-the-art in calcium (Ca^{2+}) imaging (see Grienberger et al.[47] for a recent

review of the field). Intracellular Ca^{2+} concentrations are typically very low but rise sharply in response to opening of Ca^{2+}-conductive channels, with many downstream effects including the release of neurotransmitters at the neuronal synapse, transcriptional regulation, and modulation of ion channels.[48,49] Like voltage imaging, Ca^{2+} imaging is a functional optical imaging technique used to study neuronal information processing, muscle activity, and developmental biology. There are several important differences between voltage imaging and Ca^{2+} imaging, whose implications for voltage imaging will be the subject of chapter 3, but the path by which the Ca^{2+} imaging techniques have become one of the dominant techniques in experimental neuroscience offers valuable lessons to the field of voltage imaging.

Like voltage, Ca^{2+} concentrations do not provide a direct optical readout and therefore require transduction of the biological feature to an optical response. As with voltage imaging, Ca^{2+} imaging began with synthetic small-molecule dyes,[50,51] then shifted towards genetically-encoded calcium indicators[52,53] (GECIs) once appropriate calcium-binding and fluorescent proteins became available. Any optical imaging technique, Ca^{2+} and voltage imaging included, is limited by light scatter and absorption to imaging only superficial layers in the brain[54]. The development of two-photon (2P) laser scanning microscopy[55] immediately suggested the use of this novel technique to significantly extend the depths at which functional Ca^{2+} imaging could be performed. A two-photon microscope produces very high instantaneous intensities of near-infrared pulsed laser light in order to produce simultaneous absorption of two photons by the fluorophore, exciting the fluorophore by approximately twice the energy of a single photon. This both provides intrinsic optical sectioning, because fluorescence is only excited in a very small focal spot, and allows use of near-IR excitation light, which both scatters less and is absorbed less than visible light in brain tissue[56,57]. Because of these advantages, two-photon imaging of genetically-encoded calcium indicators is currently one of the most broadly used techniques for studying brain activity *in vivo* at cellular and broader regional resolution.[47]

The maturation of Ca^{2+} imaging into a widespread and accessible technique has been enabled not only by significant scientific discoveries but also by development of widely available and robust hardware and software platforms for functional calcium imaging. While early application of 2P Ca^{2+} imaging[58] required significant customization of optics, the control system, and the analysis pipeline, a modern neuroscientist can purchase a complete microscope system designed for Ca^{2+} imaging from any of several vendors, and this microscope can be controlled either by vendor-supplied proprietary software or by a robust open-source microscope control library such as ScanImage[59].

1.3 Current challenges to widespread adoption of voltage imaging

The ability to measure membrane potentials at high spatial and temporal resolution from large populations of cells has been a dream of neuroscience for decades. Optical imaging of GEVIs has the potential to make this dream a reality. Yet there are currently three main barriers to achieving this full potential, which I will address in this dissertation.

Two-photon imaging offers the same advantages to voltage imaging as it offers to Ca^{2+} imaging. The increased depth-penetration would allow imaging of electrical activity through the deeper layers of the rodent cortex, while the optical sectioning capabilities would allow discrimination of signals from different subcellular compartments including the networks of thin dendrites that integrate inputs into each neuron. For reasons that were not well understood, however, the microbial rhodopsin GEVIs that offer the best kinetics for neural recording lose voltage sensitivity under standard two-photon imaging conditions.[30,60] Two-photon voltage imaging has therefore been limited to voltage sensitive dyes and VSD-GEVIs, which smooth and distort fast neural activity due to their slower kinetics. One possible solution would be to abandon the opsin-GEVIs for 2P voltage imaging, focusing on improving the kinetics of VSD-GEVIs. In fact, recently developed VSD-GEVIs,

like JEDI-2P[38], are approaching the speed of opsin-GEVIs. In chapter 2 of this dissertation, I pursue the second possibility—discovering the mechanism of opsin-GEVI loss of sensitivity under 2P conditions in order to enable 2P imaging from existing opsin-GEVIs and inform future rational development of 2P-optimized opsin-GEVIs.

The second barrier results from the important differences between Ca^{2+} imaging and voltage imaging. Due to the membrane localization of voltage indicators, the fast dynamics of neural electrical signals, and the small fractional fluorescence changes to be measured, voltage imaging requires significantly more advanced instrumentation, both in hardware and in software, than does Ca^{2+} imaging. I discuss the implications of these differences for the upper-bound performance of 2P voltage imaging in chapter 3 of this dissertation, and then in chapter 4 discuss our design and implementation of an open-source software package for customizable high-speed synchronized optical recordings, designed specifically to provide capabilities that are necessary for cutting-edge voltage imaging experiments but not provided by existing control libraries.

Finally, while the readout of uncalibrated relative voltage changes is sufficient for detection of action potentials, there are applications for which a readout calibrated to absolute voltage levels is necessary. These range from visualizing slow shifts in resting potential during tissue development to comparing fast voltage response levels on an absolute scale among different parts of the same cell or network. For slow signals, fluorescence lifetime imaging (FLIM) can provide a calibrated absolute readout[60], but FLIM faces fundamental obstacles to imaging at the near-kilohertz rates required to track neural spiking[61,62]. Chapter 5 presents a theoretical demonstration of how two appropriately chosen one-photon-excitable voltage indicators can provide absolute calibration of voltage imaging. Unfortunately, the high-sensitivity, highly nonlinear sensors required for this technique are not currently available, but this theoretical treatment may motivate their development and dissemination. The same technique could be used to provide calibration for Ca^{2+} and other functional imaging techniques.

This work brings forward the field of voltage imaging by rationally discovering the means of regaining 2P voltage sensitivity in opsin-GEVIs, defining the limits of 2P voltage imaging performance, providing a powerful software library for voltage imaging control, and proposing a new technique for calibration of optical voltage recordings. In chapter 6, I discuss the technical outlook for the field in light of this work. Within the limitations laid out in chapter 3, there is much room for further development of the technique. Both the experimental demonstration of 2P voltage sensitivity in an opsin-GEVI and the theoretical treatment of absolute voltage imaging provide insight into the most productive directions for future voltage indicator development. One critical area that this work does not address is the development of robust and accessible hardware for voltage imaging. While much effort is being directed towards advancing voltage imaging instrumentation [38,63–71], the field has now reached the stage at which effort should be directed towards making these voltage imaging hardware platforms more broadly usable and available.

2

Photophysics-informed two-photon voltage imaging using FRET-opsin voltage indicators

2.1 Abstract

Microbial rhodopsin-derived genetically encoded voltage indicators (GEVIs) are powerful tools for mapping bioelectrical dynamics in cell culture and in live animals. Förster resonance energy transfer (FRET)-opsin GEVIs use voltage-dependent changes in opsin absorption to modulate the fluorescence of an attached fluorophore, achieving high brightness, speed, and voltage sensitivity. However, the voltage sensitivity of most FRET-opsin GEVIs has been reported to decrease or vanish under two-photon (2P) excitation. Here we investigated the photophysics of the FRET-opsin GEVIs Voltron1 and 2. We found that the voltage sensitivity came from a photocycle intermediate, not from the opsin ground state. The voltage sensitivities of both GEVIs were nonlinear functions of illumination intensity; for Voltron1, the sensitivity reversed sign under low-intensity illumination. Using photocycle-optimized 2P illumination protocols, we demonstrate 2P voltage imaging with Voltron2 in barrel cortex of a live mouse. These results open the door to high-speed 2P voltage imaging of FRET-opsin GEVIs *in vivo*.

2.2 Introduction

Genetically encoded voltage indicators (GEVIs) are a powerful class of fluorescent probes for mapping bioelectrical signals.[72] These tools have been used in multiple species[16,40,44,73–75] and at levels of biological organization from sub-cellular[45,46,76] to organ-wide[22,77,78]. Microbial rhodopsin-based GEVIs have fast (sub-millisecond) responses to voltage steps, and good voltage sensitivity.[41,79] The first opsin-based GEVIs relied on the near infrared fluorescence of the retinal cofactor, but this signal was very dim.[40,41,80] In Förster resonance energy transfer (FRET)-opsin GEVIs, voltage-dependent changes in the opsin absorption spectrum modulate the efficiency of FRET from an attached fluorophore, leading to modulation of the fluorophore fluorescence (Fig. 2.1a).[42,81] This approach has been demonstrated with fusions of fluorescent proteins to microbial rhodopsins,[18,75] and with fusions of the HaloTag receptor, which can be covalently loaded with a small-molecule organic dye.[43,44] FRET-opsin GEVIs are fast, bright, and sensitive[42–44,82,83].

A key challenge in voltage imaging is to resolve signals within light-scattering tissues, such as the brain. Most applications of voltage imaging to-date have used one-photon (1P) excitation. While structured illumination, far-red excitation, and use of photo-activatable GEVIs[84] can partially reduce the background from scattered light, 1P voltage imaging is still limited to imaging the top $\sim$250 μm of brain tissue. Two-photon (2P) excitation has been transformative for calcium imaging *in vivo*, so there has been substantial interest in developing 2P voltage imaging systems.[38,64] The FRET-opsin GEVIs would be attractive targets for 2P voltage imaging, but, for reasons that have remained mysterious, most FRET-opsin GEVIs show little or no voltage sensitivity under typical 2P illumination conditions, even when the fluorescence count-rate is high enough that voltage-induced fluorescence changes should be detectable.[30,60] Furthermore, these same samples can return to showing voltage sensitivity under 1P illumination after 2P illumination.[60] These observations led us to explore the photophysical basis of voltage sensitivity in FRET-opsin GEVIs.

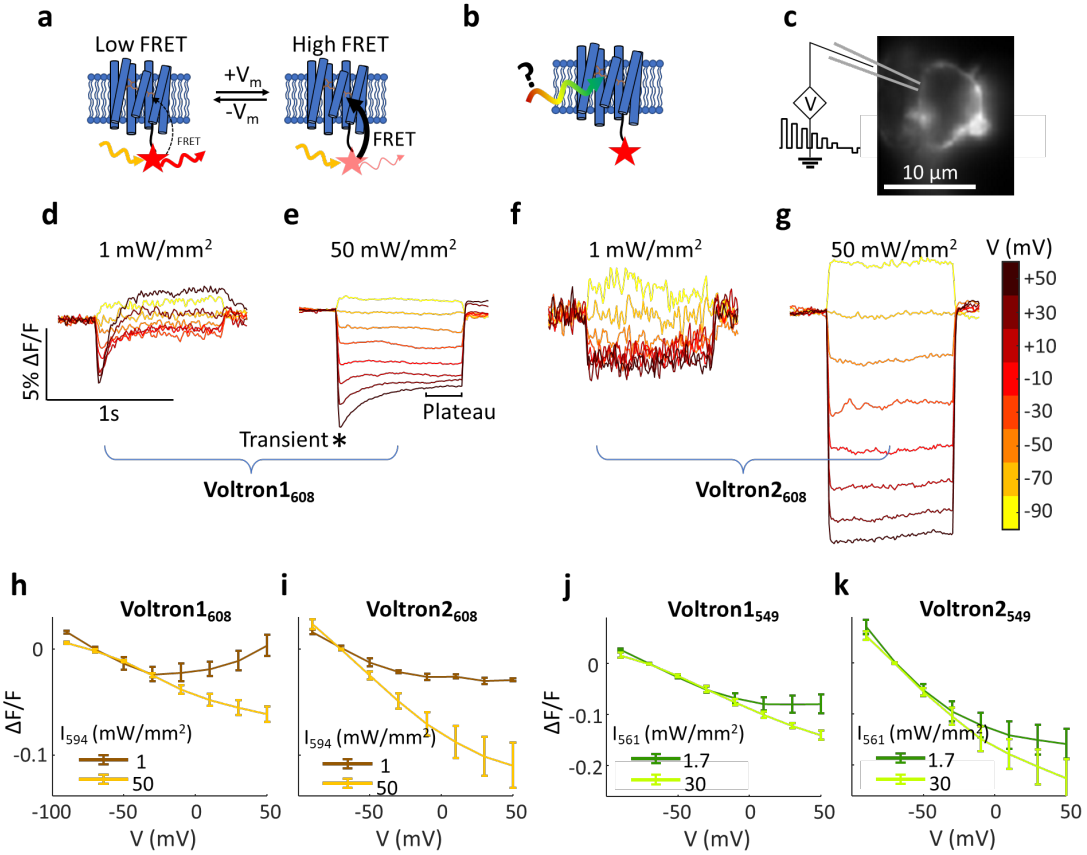

Figure 2.1: a) A simple model of a FRET-opsin GEVI. A fluorescent FRET donor is optically excited and can relax either by fluorescence or by FRET to the retinal chromophore. Voltage-dependent shifts in the retinal absorption spectrum modulate the fluorescence of the donor. b) The light used to excite the FRET donor may also excite the retinal directly, driving photo-transitions in the opsin and changing the voltage-sensing properties of the GEVI. c) Fluorescence image of a HEK-293T cell expressing Voltron2$_{608}$ and subject to voltage clamp. d,e) Voltage step responses from cells expressing Voltron1$_{608}$ at low (1 mW/mm^2) and high (50 mW/mm^2) illumination intensities, λ = 594 nm. Transient and plateau phases of the response are indicated. At low intensity, steady state fluorescence responses showed a non-monotonic dependence on membrane voltage. f,g) Same as (d,e) for Voltron2$_{608}$, with the same ΔF/F vertical scale. h-k) Plots of steady-state ΔF/F vs. V for (h) Voltron1$_{608}$, (i) Voltron2$_{608}$, (j) Voltron1$_{549}$ and (k) Voltron2$_{549}$. Each curve is plotted for dim (dark colors) and bright (light colors) illumination. For all reporter combinations, both the slope and the shape of the curve were sensitive to illumination intensity. Error bars represent s.e.m. from 3-6 cells.

In the simplest model of a FRET-opsin GEVI (Fig. 2.1a), a voltage-insensitive FRET donor is optically excited. The opsin FRET acceptor sits in a voltage-sensitive equilibrium between two states, one of which quenches the donor more efficiently than the other. This simple model produces two important predictions. First, the fractional response of the donor fluorescence to voltage (i.e. $\Delta F/F$ vs. V) should be a function only of voltage and not of any illumination parameters. Second, any excitation method (e.g., 1P or 2P) that produces the same donor excited state should produce the same voltage-sensitive fluorescence signal. The documented failure of 2P voltage imaging with FRET-opsin GEVIs suggests that this simple picture is inadequate.

The light used to excite the FRET donor can also interact with the opsin acceptor directly (Fig. 2.1b). Microbial rhodopsins have complex photocycles, with at least seven spectroscopically distinguishable states, and a variety of light- and voltage-modulated transitions.[85–90] Indeed, in wild-type Archaerhodopsin 3, voltage-sensitive retinal fluorescence comes from a photocycle intermediate termed the "Q state", and exciting this fluorescence requires sequential absorption of three photons.[88] The engineering of QuasAr1, QuasAr2 and the Archon variants caused the voltage sensitivity to appear as a 1-photon process, but this signal still arises from a complex photocycle involving multiple absorbing states[90–92].

The complexity of opsin photocycles has been harnessed to create light-gated voltage integrators,[93] light-gated voltage sample-and-hold motifs,[93] reporters of absolute voltage,[94] and photoactivated voltage indicators.[84] Thus we hypothesized that the voltage-sensing properties of FRET-opsin GEVIs might depend in a complex way on the intensity, wavelength(s), and time-course of illumination; and that an understanding of these dependencies might point to illumination protocols which would enable 2P voltage imaging.

2.3 Results

We expressed Voltron1 [43] or Voltron2 [44] in HEK-293T cells and labeled the samples with HaloTag ligand dye JF_{608} (Methods). We selected this dye because it has been useful in all-optical electrophysiology experiments with Voltron1 and 2. [45,46] We then used whole-cell voltage clamp to vary the membrane voltage and we recorded the fluorescence under continuous 594 nm 1P illumination at different intensities (Fig. 2.1c).

We first applied a series of voltage steps from a holding potential of -70 mV to voltages between -90 mV and +50 mV (Fig. 2.1d-g). At high illumination intensity (50 mW/mm^2), both GEVIs showed an approximately linear and negative-going dependence of steady-state fluorescence on membrane voltage, with slopes $\Delta F/F$ = -0.054 ± 0.007 per 100 mV (Voltron1, n = 4 cells) and $\Delta F/F$ = -0.11 ± 0.02 per 100 mV (Voltron2, n = 5 cells), where ΔF was measured relative to F at V = -70 mV (Fig. 2.1h, i). For depolarizations to > 0 mV, Voltron1 showed an initial transient fluorescence peak (Fig. 2.1e), but Voltron2 did not (Fig. 2.1g). These data are all consistent with prior reports [43,44].

At low illumination intensity (0.97 mW/mm^2), the voltage responses of both GEVIs changed dramatically. The initial transient fluorescence response of Voltron1 maintained its approximately linear negative-going dependence on voltage. However, the steady-state F vs. V response of Voltron1 became non-monotonic. For small depolarizations relative to -70 mV, the fluorescence decreased, as at high intensity. But for depolarizations to > -20 mV, the Voltron1 fluorescence increased as voltage increased, and at voltages > +30 mV, the steady-state fluorescence was actually brighter than at V = -70 mV (Fig. 2.1d, h).

For Voltron2 at low illumination intensity, the voltage step-response maintained its top-hat structure (Fig. 2.1f), but the overall voltage sensitivity decreased nearly twofold for small depolarizations around -70 mV and the voltage response leveled off for voltages > -20 mV. Qualitatively similar

intensity-dependent changes in the transient and steady-state voltage responses were observed when the two GEVIs were loaded with JF_{549} and excited at 561 nm (Fig. 2.1j, k).

To quantify the influence of illumination intensity on voltage sensitivity, we performed voltage-clamp experiments at 1P illumination intensities spanning nearly four orders of magnitude, from 0.06 mW/mm^2 to 100 mW/mm^2 (Fig. 2.2a,b). At each intensity, we clamped the voltage at -70 mV and then measured the fluorescence responses to a 100 mV depolarizing step to +30 mV. We plotted separately the initial and steady-state fluorescence responses, as marked in Fig. 2.1e (for Voltron2, initial and steady state fluorescence were indistinguishable).

The data showed several surprising features. For an idealized GEVI, one would expect both ΔF and F to be proportional to intensity, and their ratio ($\Delta F/F$) to be independent of intensity. We found that for both indicators, $\Delta F/F$ depended strongly on illumination intensity. This observation shows that statements of FRET-opsin voltage sensitivity are only meaningful if illumination intensity is specified. For both GEVIs, the voltage sensitivity was greatest (in absolute value), and the illumination intensity dependence leveled off, around 10-30 mW/mm^2. By good fortune, this intensity regime is typically used in neural recordings because it produces high enough per-cell count rates to observe neural dynamics over shot noise. This coincidence may explain why the low-intensity anomalous responses of these GEVIs were not previously reported.

These data also show the disparate effects of illumination intensity on different response timescales. At low illumination intensity, Voltron1 showed the unexpected inversion of sensitivity to 100 mV voltage steps (Fig. 2.2a). Further, at low intensity Voltron1 showed enhanced disparity between the transient and steady-state responses to 100 mV voltage steps. While the sensitivity of Voltron2 was in general superior to Voltron1, for illumination intensities between 1 – 10 mW/mm^2, the transient response of Voltron1 was larger than that of Voltron2. Thus, Voltron1 may outperform Voltron2 at spike detection under moderate illumination intensity.

We next sought to determine the kinetics with which voltage sensitivity increased under bright

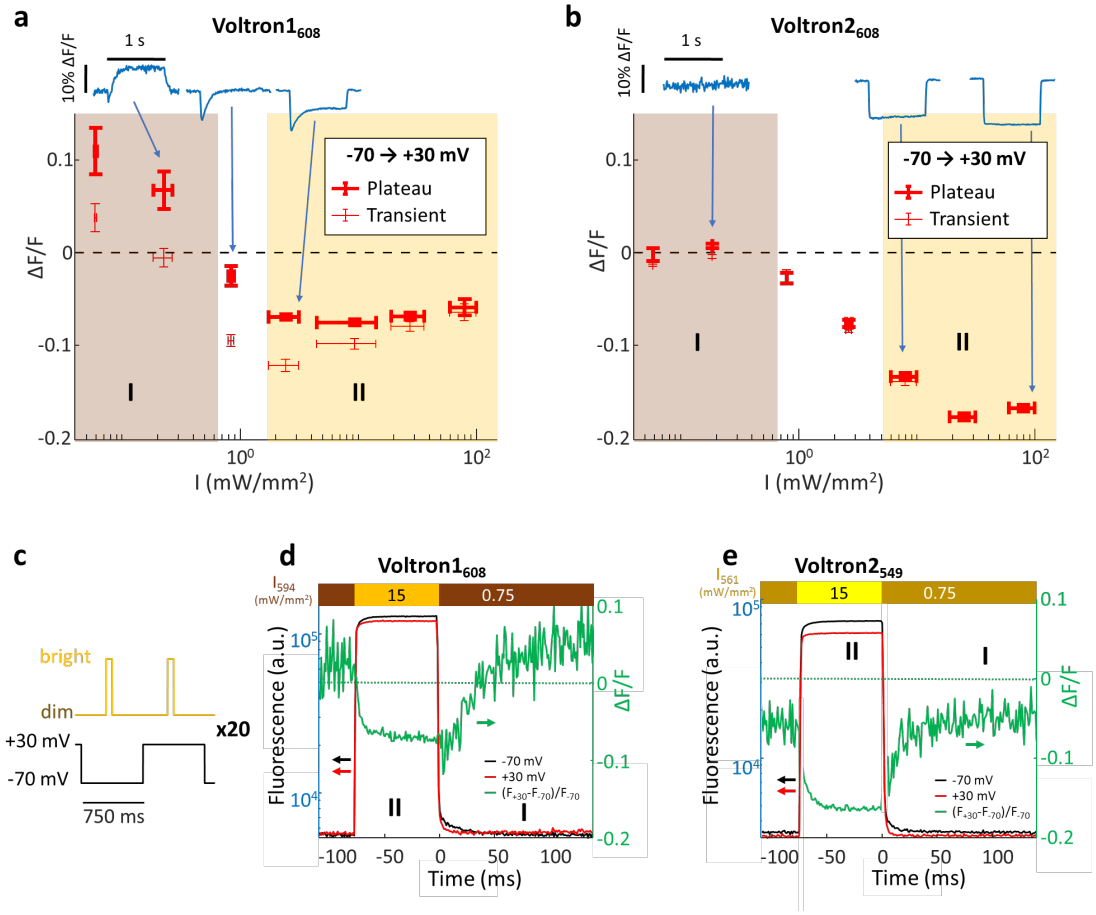

Figure 2.2: a) Fractional sensitivity (ΔF/F) of Voltron1$_{608}$ as a function of illumination intensity for a voltage step from -70 to +30 mV. Heavy markers denote the steady-state response, thin markers denote the initial transient response (*n* = 5 cells). Horizontal error bars denote the range of illumination intensities binned into one measurement; vertical error bars denote s.e.m. The traces in blue show representative step responses from dim, moderate, and bright illumination. Roman numerals **I** and **II** mark the insensitive and voltage-sensitive states, respectively (also in b,d,e). b) Same as panel (a), but for Voltron2$_{608}$. (*n* = 3 cells). c) Protocol for measuring dynamic GEVI responses to a change in illumination intensity. Dynamics in the "dark" were probed by very dim (0.75 mW/mm^2) illumination; bright pulses (75 ms, 15 mW/mm^2) transiently populated the voltage-sensitive stage. d) Fractional voltage sensitivity of Voltron1$_{608}$ (green, right axis) was calculated from the difference between the fluorescence at -70 mV (black, left axis) and at +30 mV (red, left axis). Sensitivity emerged with a time constant of 5 ms, reached a plateau during the light pulse, and then declined with a time constant of 46 ms after the bright pulse. e) Same as (d) for Voltron2$_{549}$. Sensitivity emerged with a time constant of 7 ms and declined with a time constant of 18 ms.

illumination and decreased under dim illumination. To measure these parameters, in HEK cells expressing either Voltron1$_{608}$ or Voltron2$_{549}$, we alternately clamped the voltage at -70 mV and +30 mV, and at each voltage we applied pulses of bright light (594 nm for JF$_{608}$, 561 nm for JF$_{549}$; 75 ms, 15 mW/mm^2) interleaved with dim light (675 ms, 0.75 mW/mm^2; Fig. 2.2c). By comparing the fluorescence at the two voltages during the dim-to-bright and bright-to-dim transitions, we measured the onset and decay of voltage sensitivity (Fig. 2.2d, e). For Voltron1$_{608}$, voltage sensitivity arose with a time-constant of 5 ms and decayed with a time-constant of 46 ms (Fig. 2.2d). For Voltron2$_{549}$, voltage sensitivity arose with a time-constant of 7 ms and decayed with a time-constant of 18 ms (Fig. 2.2e).

The appearance of the "normal" (i.e. previously reported) F vs. V behavior only at high illumination intensities, along with the finite time constants for voltage sensitivity to arise in response to a step-wise increase in illumination intensity, suggested that canonical Voltron voltage sensitivity might involve a photocycle intermediate, not the ground state (Fig. 2.3). Sufficient 1P illumination populates the voltage-sensitive state, which then thermally relaxes to the dark-adapted state.

2.3.1 Two-photon photophysics

We hypothesized that the previously reported poor 2P voltage sensitivity in opsin-based GEVIs[60,95] might arise from failure to populate voltage-sensitive photocycle intermediates (Fig. 2.3). This hypothesis is consistent with our observations that sufficient 1P illumination was required to observe 1P voltage sensitivity and with the much lower per-molecule excitation rate of 2P vs. 1P excitation[95].

JF$_{549}$ was the first dye reported for use with Voltron[43] and has a 2P excitation peak in the center of the 1030-1080 nm mid-IR window reachable by multiple femtosecond laser technologies. We expressed Voltron2$_{549}$ in HEK cells, clamped the voltage at -70 mV, and applied a series of voltage steps ranging from -90 mV to +50 mV. We first imaged the sample with donut-scanned 1040 nm

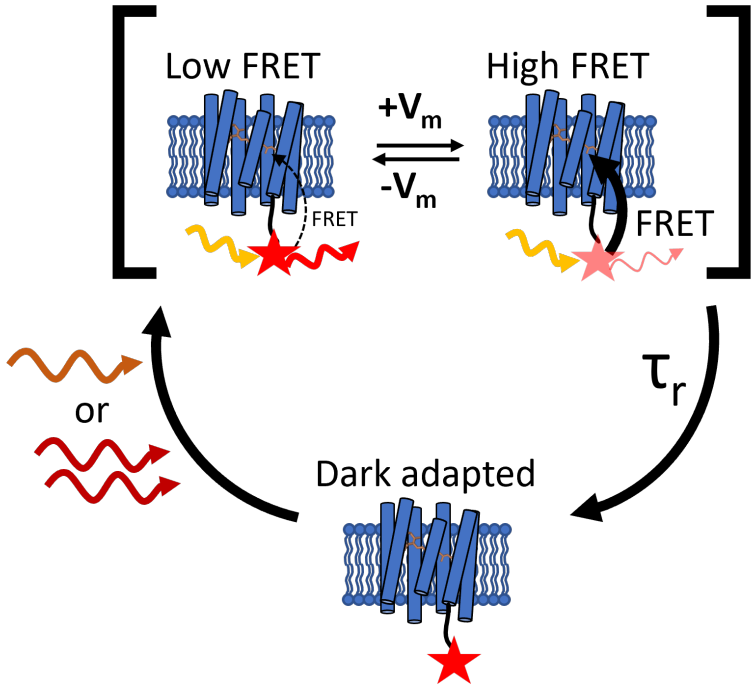

Figure 2.3: Dark-adapted Voltron2 does not show voltage-dependent FRET. Upon absorption of at least one photon with the proper energy (e.g. 594 nm or 1135 nm 2P), the opsin enters a voltage-sensitive equilibrium between high and low FRET states. The voltage sensitive equilibrium relaxes to the dark-adapted state with a time constant $\tau_r \sim 18$ ms. Voltage imaging requires concurrent measurement of the FRET donor fluorescence and optical pumping of the voltage-sensitive photocycle intermediate.

2P excitation (9.4 mW, 1 kHz scan repetition rate), and then applied the same voltage steps immediately afterwards under widefield 1P excitation (26 mW/mm^2, 532 nm). Under 2P illumination, the fractional voltage sensitivity was much smaller and the step-response kinetics much slower compared to 1P illumination of the same cell (Fig. 2.4a). At 9.4 mW/cell, the dye bleached with a time constant of 3 s (Fig. 2.4a, inset). The 2P voltage sensitivity was -0.036 ± 0.015 per 100 mV (n = 6 cells, mean ± s.e.m., Fig. 2.4d,e), significantly smaller than the 1P sensitivity of 0.10 ± .02 per 100

mV (n = 7 cells, mean ± s.e.m., Fig. 2.4e) from paired measurements on the same set of cells (p = 0.04; two-tailed t-test, one cell only had a 1P recording; Fig. 2.1e).

The 2P action spectrum for Voltron sensitization is not known, but prior work on 2P excitation of bacteriorhodopsin provides some guidance. For bacteriorhodopsin, 2P excitation of the S_1 first excited state transition peaks at 1140 nm, whereas 2P excitation of the S_2 second excited state transition (a symmetry-forbidden 1P transition) is a broad peak centered just under 1000 nm.[96] Retinal isomerization and initiation of the photocycle require excitation to S1, so we reasoned that 2P excitation to S_1 might favor voltage sensitivity while excitation to S_2 might be unproductive or even counteract sensitization. This reasoning suggested that 2P excitation around 1140 nm might favor population of voltage sensitive states. JF_{608} dye shows 2P excitation with a peak around 1135 nm,[97] so we reasoned that in $Voltron2_{608}$, 2P light at 1135 nm might drive opsin sensitization and simultaneously excite the FRET donor for voltage imaging.

Figure 2.4 *(following page)*: a) Comparison of Voltron2$_{549}$ voltage sensitivity under 2P vs. 1P illumination. A HEK-293T cell expressing Voltron2$_{549}$ was subjected to voltage steps from a holding potential of -70 mV. Fluorescence was recorded under 2P excitation and then under 1P excitation. The fractional changes in fluorescence were smaller and slower under 2P vs. 1P excitation. Inset shows magnified 2P fluorescence trace. Photobleaching was corrected before calculating ΔF/F. b) Same as (a), but with Voltron2$_{608}$. c) Voltage step response from the same Voltron2$_{608}$-expressing cell shown in panel (b). d) Voltage response under 2P excitation for Voltron2$_{549}$ and Voltron2$_{608}$, under dim (3-4 mW, dark colors) and bright (9.4-9.5 mW, light colors) illumination. Error bars s.e.m., *n* = 6-12 cells. e) Comparison of responses to 100 mV step (-90 to +10 mV) for Voltron2$_{549}$ and Voltron2$_{608}$ from matched samples and measurement conditions. Voltron2$_{549}$ 1P: 26 mW/mm^2, 532 nm, *n* = 7 cells; 2P: 9.4 mW, 1040 nm, *n* = 6 cells. Voltron2$_{608}$ 1P: 6 mW/mm^2, 594 nm, *n* = 11 cells; 2P: 9.5 mW, 1135 nm, *n* = 8 cells. Error bars mean ± s.e.m. 1P voltage sensitivity was significantly greater than 2P voltage sensitivity for Voltron2$_{549}$ (p = 0.04 two-tailed t-test), but not for Voltron2$_{608}$. f-j) 2P voltage imaging in acute brain slices co-expressing Voltron2$_{608}$ and CheRiff. f) Left: experimental protocol. Right: (top) once a neuron was located, a 2P donut scan was targeted to the soma (500 Hz, 5.5 mW, 1135 nm.). (bottom) Fluorescence image recorded on a camera with donut-scan 2P excitation. g) Fluorescence traces (left axis, ΔF/F; right axis, F) of from 1P (top) and 2P (bottom) epochs of a single recording. A ramp of blue light from 0 to 0.5 mW/mm^2 evoked spikes. h) Spike-triggered average traces from (g) were normalized and overlayed, demonstrating similar response kinetics for 1P and 2P recordings. i) Spike heights under matched 1P and 2P recordings were not significantly different (*n* = 10 cells, paired t-test). j) SNR vs. fluorescence (counts/cell/frame) for each recorded cell (*n* = 10 cells). The SNR and fluorescence show a power-law relationship with exponent b = 0.53 (95% confidence bounds: 0.35-0.72, R^2 = 0.68), consistent with shot-noise limited SNR (b = 0.5) with the same relative signal level for 1P and 2P excitation. The higher SNR of the 1P recording can be attributed to the brighter fluorescence.

Figure 2.4: (Continued)

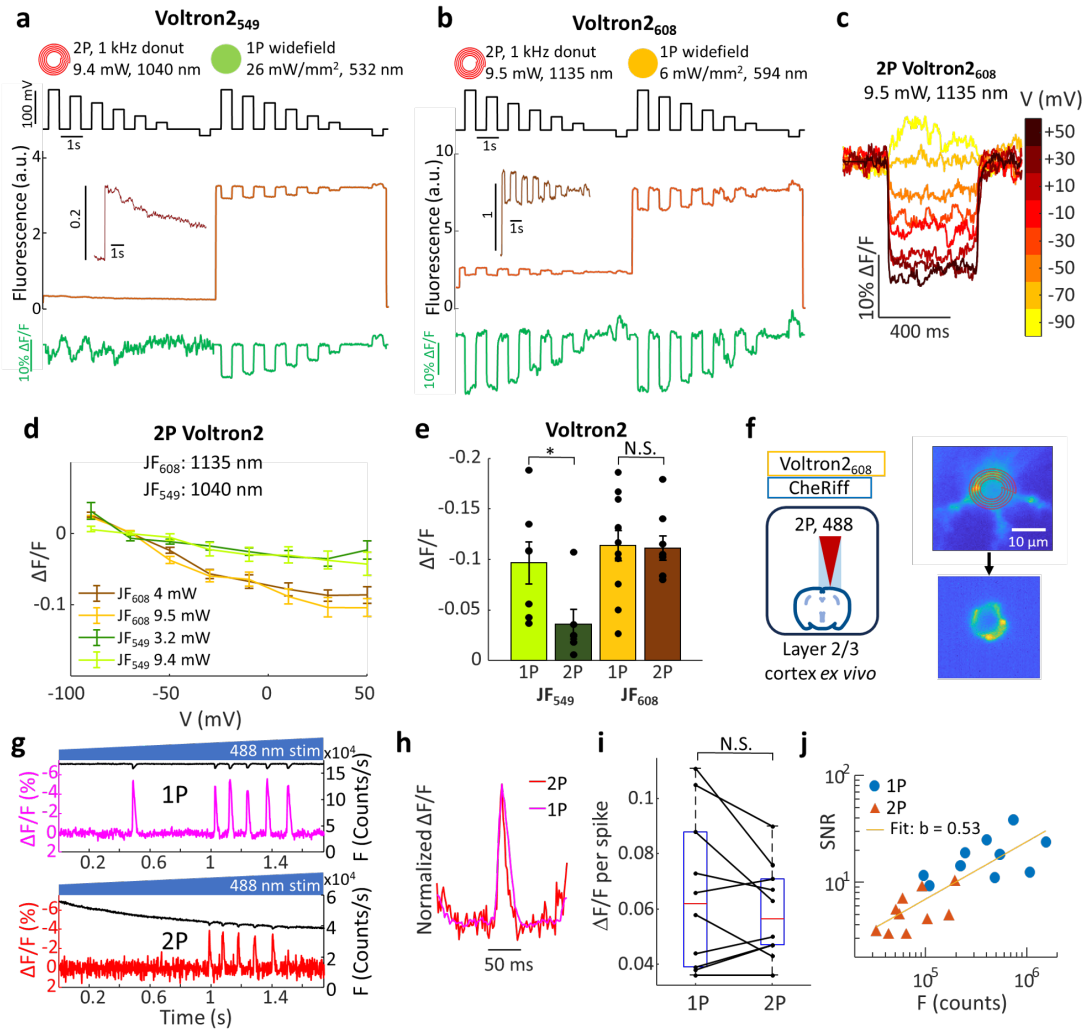

We expressed Voltron2$_{608}$ in HEK cells, clamped the voltage at -70 mV, and applied voltage steps ranging from -90 mV to +50 mV under either bright (9.5 mW) or moderate (4 mW) 2P excitation at 1135 nm (Fig. 2.4b-e). The laser scan traced the periphery of the cell membrane at 1000 Hz. We then repeated the voltage steps under moderate (6 mW/mm^2) 1P excitation at 594 nm (Fig. 2.4b). Under 2P excitation, Voltron2$_{608}$ showed much larger voltage sensitivity than Voltron2$_{549}$ (Fig. 2.4c-e), consistent with our hypothesis that long-wavelength 2P excitation was more effective at populating the voltage-sensitive photocycle intermediate.

For both Voltron2$_{549}$ and Voltron2$_{608}$, the voltage sensitivity under lower (3.2 - 4 mW) 2P power was similar to the sensitivity at 9.4 – 9.5 mW (Fig. 2.4d). This observation suggests that increasing 2P power beyond a few mW/cell would not increase the voltage sensitivity further, though the increase in overall brightness at higher laser power would increase the shot noise-limited SNR. Due to the low fluorescence signal under 2P conditions, we were not able to explore lower 2P powers.

We next explored 2P voltage imaging with Voltron2$_{608}$ in mouse acute brain slices. We co-expressed Voltron2 and CheRiff, a blue light-activated channelrhodopsin, in layer 2/3 cortical pyramidal neurons via in utero electroporation. We prepared acute brain slices and incubated the slices with JF$_{608}$ dye. We sequentially performed 1P (594 nm, 22 mW/mm^2) and 2P (1135 nm, 25 mW) imaging on the same cells while evoking neuronal spikes with dim ramping (0-0.5 mW/mm^2) 488 nm illumination (Fig. 2.4g). The spike-triggered average waveforms under 1P and 2P excitation matched closely, demonstrating that 1P and 2P recordings with Voltron2$_{608}$ have the same time resolution.

We performed the same paired 2P and 1P recording protocol on pyramidal cells from cortical layer 2/3 and from hippocampus CA1. We varied 1P excitation power (22 - 70 mW/mm^2) and 2P power (5.5 - 15 mW), to explore the effect of brightness in the sensitivity-saturated regime. Across 10 recordings (two recordings from each of 5 cells), we found no significant difference between 2P and 1P voltage sensitivity, $\Delta F/F$ per spike (Fig. 2.4i). For each recording, we also calculated the

SNR (ratio of spike height to baseline noise) and plotted this against the fluorescence counts per cell per frame (Fig. 2.4j). On a log-log plot, the 2P and 1P data fell along the same line, with a slope of 0.53 (95% confidence bounds: 0.35-0.72, $R^2 = 0.68$). This observation is consistent with both signals being shot-noise limited (slope = 0.5) with the same signal strength. Thus the greater SNR of the 1P recordings was attributed almost entirely to the increased fluorescence brightness under 1P conditions.

Finally, we tested 2P voltage imaging of Voltron2$_{608}$ *in vivo*. We injected a viral vector for cre-dependent bicistronic expression of Voltron2 and CheRiff into Layer 1 barrel cortex of Ndnf-Cre mice. We performed optical stimulation and voltage imaging of layer 1 interneurons through a surgically implanted window in an anesthetized mouse. We sequentially performed 1P (594 nm, 30 mW/mm^2) and 2P (1135 nm, 11-20 mW) imaging on the same cells while evoking neuronal spikes with pulses of 488 nm illumination of successively greater intensity (0.2-0.35 mW/mm^2; Fig. 2.5a). The spike-triggered average spike waveforms under 1P and 2P excitation matched closely, displaying identical millisecond-scale spike kinetics.

We compared statistics from four recordings (one from each of four cells). The 1P voltage sensitivity was better than the 2P sensitivity in three of the cells, but this did not reach statistical significance. The decreased 2P sensitivity may have been partially the result of bleaching at the higher 2P powers attained in these experiments. A log-log plot of SNR vs. fluorescence did not demonstrate a linear relationship ($R^2 = 0.18$). For both 1P and 2P recordings, the noise had substantial contributions from background fluorescence, motion artifacts, and blood flow, leading to cell-specific noise above shot noise.

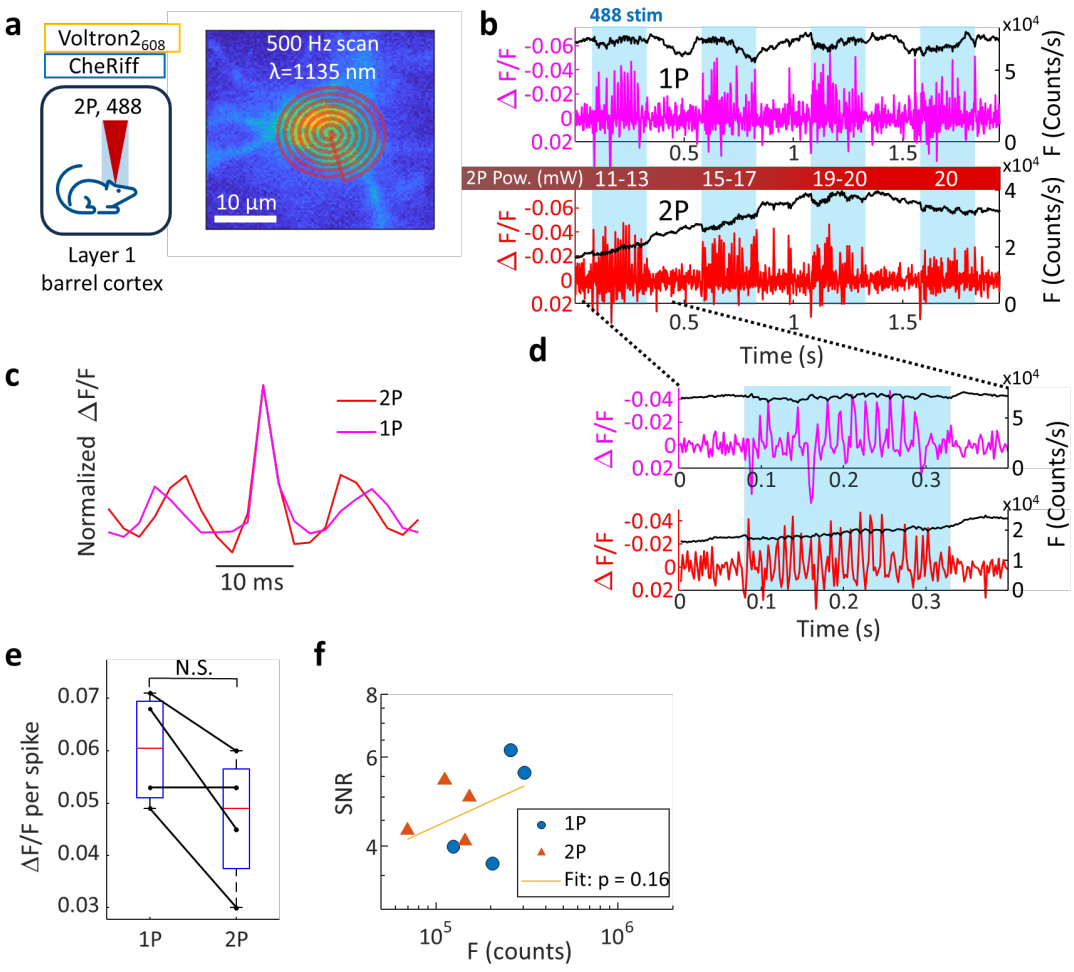

Figure 2.5: a) Cre-dependent Voltron2 and CheRiff were expressed by AAV injection in Layer 1 barrel cortex of Ndnf-Cre mice. JF_{608} dye was injected the day prior to the experiment, and neurons were imaged through a craniotomy under a 2P donut scan, 1135 nm, 500 Hz. b) Fluorescence traces (left axis, detrended ΔF/F; right axis, F) of from 1P (top) and 2P (bottom) epochs of a single recording. Pulses of blue light increasing from 0.2 to 0.35 mW/mm^2 evoked spikes. 1P: 30 mW/mm^2 594 nm excitation; 2P: 1135 nm excitation at slowly increasing power to counteract photobleaching. Optogenetic stimulation evoked spikes which were detectable via voltage imaging. c) Spike-triggered average traces from (b) were normalized and overlayed, demonstrating similar response kinetics for 1P and 2P recordings (1P: N = 49 spikes; 2P: N = 54 spikes). d) Response to a single blue pulse. e) Spike heights under matched 1P and 2P recordings were not significantly different (n = 4 cells). f) SNR vs. fluorescence (counts/cell/frame) for each recorded cell (n = 4 cells, slope p = 0.16 ± 0.35 95% confidence interval; R^2 = 0.18). Deviation from shot noise-limited SNR *in vivo* is likely due to contributions from background fluorescence, brain motion, and blood flow.

2.4 Discussion

The absence of 2P voltage sensitivity with FRET-opsin reporters has long been a barrier in the field of voltage imaging. Here we show that 2P voltage imaging with FRET-opsin GEVIs is feasible if the illumination populates the voltage-sensitive photocycle intermediates. Achieving this goal required selecting a 2P excitation wavelength (1135 nm) that efficiently populated the intermediate state and a dye that was efficiently excited at this wavelength while also undergoing efficient FRET with the opsin, and applying scan patterns which revisited each molecule frequently enough to overcome relaxation of the voltage-sensitive intermediates. These results open the door to 2P voltage imaging *in vivo* with FRET-opsin GEVIs.

Our spectroscopic studies point to strategies for rational improvement of both 1P and 2P FRET-opsin GEVIs and voltage imaging systems. For instance, there may be other dyes whose excitation peak better matches the peak of the 2P opsin sensitization spectrum while still engaging in productive FRET with the voltage-sensitive states. Protein engineering efforts to slow the kinetics of relaxation of the voltage-sensitive states could also enhance voltage sensitivity. Furthermore, one might engineer imaging systems in which 1P and 2P illumination are interleaved, with the 1P driving population of the voltage-sensitive states and the 2P providing the excitation for optically sectioned imaging.

2P voltage imaging still faces difficulties as a practical tool for *in vivo* neural imaging. We recently compared the power budgets of 1P and 2P excitation: to achieve useful count rates for voltage imaging with a standard 80 MHz source, 2P excitation requires $\sim 10^4$-fold greater power per cell compared to 1P excitation.[95] The maximum biologically safe laser power for 2P voltage imaging can be set by either average or peak illumination intensity. The time- and space-average power into the sample should be capped to avoid temperature rises greater than a few °C (5 °C can induce permanent damage, but smaller temperature rises may alter neural firing patterns).[98] The peak intensity at

the laser focus should not exceed ~1 nJ/pulse, the saturation intensity of most fluorophores.[99] At higher intensities, nonlinear photodamage might occur.

Our brightest 2P voltage recording was obtained at a power of just under 10 mW (0.125 nJ/pulse at 80 MHz), which induced bleaching with a time constant as short as 2.5 s (with scan-to-scan variation). Increases in peak pulse energy, offset by decreases in laser repetition rate, may enable brighter overall fluorescence signals and improvements in SNR, provided that the thermal and peak-intensity limits are respected. We discuss the optical and molecular constraints on 2P voltage imaging in detail in chapter 3.

Our results also have important implications for use of Voltron2 under 1P excitation. For very long-term recordings, a natural inclination is to decrease the illumination intensity to avoid photobleaching or phototoxicity. However, our results show that this strategy may unintentionally lead to a loss of voltage sensitivity. A better strategy would be to interleave epochs of intense (> 10 mW/mm^2) illumination with epochs of darkness. Similarly, for voltage imaging of large samples (e.g. an entire mouse heart), the excitation intensities may be low, leading to a loss of voltage sensitivity. To preserve sensitivity, one should either make an array of focal spots, or apply intermittent high-intensity illumination.

The complex photophysics of the FRET-opsin GEVIs suggest that future protein engineering efforts should be accompanied, at a minimum, by a quantification of intensity-dependent voltage sensitivity. An interesting avenue for future explorations would be to determine the photocycle basis for the intensity-dependent changes in voltage sensitivity and voltage step-response waveforms shown in Figs. 2.1 and 2.2.

2.5 Materials and Methods

2.5.1 Genetic constructs

Voltron1 and Voltron2 plasmids were obtained from Addgene (♯119033 and ♯172909, respectively). For lentiviral transduction, the Voltron sequence was cloned into a lentiviral backbone with a CMV promoter using standard Gibson Assembly. Briefly, the vector was linearized by double digestion using restriction enzymes (New England Biolabs). DNA fragments were generated by PCR amplification and then fused with the backbones using NEBuilder HiFi DNA assembly kit (New England Biolabs). Resulting plasmids were verified by sequencing (GeneWiz).

For experiments in neurons, we co-expressed Voltron2 with a blue-shifted channelrhodopsin, CheRiff by a self-cleaving p2a linker. For *ex vivo* slice experiments, we used a previously-published whole-cell-expressing construct[45] (Addgene ♯203228). For *in vivo* experiments, we generated a plasmid with soma-localized Voltron2 and soma-localized CheRiff under the hSyn promoter and flanked by LoxP sites for Cre recombinase-dependent expression. The genes were cloned into an adeno-associated virus (AAV) backbone using standard Gibson Assembly. AAV was produced by UNC Neurotools using the supplied plasmids.

2.5.2 HEK cell culture

HEK293T cells were maintained in tissue culture-treated culture dishes (Corning) at 37 °C, 5% CO_2 in Dulbecco's Modified Eagle Medium supplemented with 10% fetal bovine serum, 1% GlutaMax-I, penicillin (100 U/mL), streptomycin (100 mg/mL). For each imaging experiment, cells in one 35 mm dish were either transiently transfected with the construct to be imaged using TransIT-293 lipofection reagent (Mirus Bio) or were virally transduced with a lentivirus. We saw no difference in voltage sensitivity or photophysics between the lipofected vs. virally transduced

HEK cells. For lipofection, the construct was diluted 1:5 with empty pUC19 vector (New England Biolabs) and then transfected with 7.5 μL of TransIT-293 and 2.5 μg of DNA. Cells were replated 36-60 hours after transfection on glass-bottomed dishes (Cellvis, Cat. ♯ D35-14-1.5-N) that were previously coated in poly-D-lysine to aid in cell adhesion.

2.5.3 Lentiviral transduction

All the lentivirus preparations were made in house. HEK293T cells were co-transfected with the second-generation packaging plasmid psPAX2 (Addgene ♯12260), envelope plasmid VSV-G (Addgene ♯12259) and transfer plasmids at a ratio of 9:4:14. For small batches, 5.6 μg total plasmids for a small culture (300k cells in 35 mm dish) gave sufficient yield of lentivirus. Lentivirus was not further concentrated. For lentiviral transduction, 100 μL of lentivirus were added to a single 35 mm dish. After 48-60 hours, cells were either replated onto glass for imaging or split and replated on 35 mm plastic dishes for continued growth. Virally transduced cultures could be used for up to three passages after transduction. For all experiments, imaging was performed 12-24 hours after replating on glass.

2.5.4 Electrophysiology and Buffers

Half an hour prior to imaging, the appropriate JF-HaloTag ligand dye was added to the medium in each dish of cells to a final concentration of 100 nM. Immediately prior to imaging, the medium was removed, and the cells were rinsed, then covered with dye-free extracellular (XC) buffer. The XC buffer contained 125 mM NaCl, 2.5 mM KCl, 3 mM $CaCl_2$, 1mM $MgCl_2$, 15 mM HEPES, 20 mM glucose, which was adjusted with NaOH to a pH of 7.3 and with sucrose to an osmolality of 305-310 mOsm, as measured by a vapor-pressure osmometer (Wescor). Filamented patch pipettes were pulled using an automated puller (Sutter P-1000) to a tip resistance of $\sim$6 MΩ and were filled

with an intracellular buffer (IC) containing (in mM) 6 NaCl, 130 K-aspartate, 2 $MgCl_2$, 5 $CaCl_2$, 11 EGTA, and 10 HEPES, with pH adjusted to 7.2 by KOH [100]. Whole-cell voltage clamp was acquired using a modified syringe to manipulate pressure, following Li. [100]

2.5.5 Microscope and illumination control

One-photon (1P) imaging experiments were performed on a custom-built inverted microscope with a computer-controlled patch amplifier (Axon Instruments, Multiclamp 700B). Once a whole-cell patch was established, acquisition was controlled using custom MATLAB/C++ acquisition software (https://www.luminosmicroscopy.com/, see chapter 4). The illumination path contained a 594 nm laser (Hübner Photonics, Cobolt Mambo) and a 561 nm laser (Hübner Photonics, Cobolt Jive). The laser outputs were modulated using a multichannel acousto-optic tunable filter (Gooch & Housego, TF525-250-6-3-GH18A with MSD040-150 driver), and imaging was performed through a high-NA 60x water-immersion objective (Olympus UPLSAPO60XW, 0.28 mm working distance, NA = 1.2) onto an sCMOS camera (Hamamatsu, ORCA-Flash 4.0). Imaging of JF_{549} and JF_{608} was performed through a 488/561/633 nm triband dichroic (Chroma) and a 405/488/594 nm triband dichroic (Semrock), respectively. A 594 nm long-pass emission filter was used for both dyes (Semrock, BLP01-594R-25). Electrical waveforms and measurements were transduced through a computer-controlled data acquisition device (National Instruments, PCIe-6343). The sample was placed on a 2-axis motorized stage (Ludl Electronic Products, MAC6000), and a 3-axis micromanipulator was used for patch pipette control (Sutter, MP-285).

Two-photon (2P) imaging experiments were performed on a custom-built upright microscope equipped with 1P and 2P illumination paths, a shared emission path to an sCMOS camera (Hamamatsu, ORCA-Flash 4.0), and a computer-controlled patch amplifier (Axon Instruments, Axopatch 200B). An 80 MHz tunable ultrafast laser (Spectra-Physics, InSight DeepSee) was modulated using an electro-optic modulator (ConOptics, 350-80-02 with 302RM driver) and directed using

a pair of galvanometric mirrors (Cambridge Technologies 6215H with 671HP driver). 488 nm (Coherent OBIS 488-100 LS), 532 nm (Laserglow LLS-05320PFM-00159-01), and 594 nm (Hübner Photonics Cobolt Mambo 0594-04-01-0100-500) lasers were combined and independently modulated using a multichannel acousto-optic tunable filter (Gooch & Housego PCAOM NIR-VIS with MSD040-150 driver). The 1P lasers were patterned using a digital micromirror device (Vialux V-7001). Imaging of HEK cells and brain slices was performed through a high-NA 25x water-immersion objective (Olympus XLPLN25XWMP2, 2 mm working distance, NA=1.05).

In vivo imaging was performed through a high-NA 25x water-immersion objective (Olympus XLPLN25XSVMP2, 4 mm working distance, NA = 1). A 785 nm long-pass dichroic (Semrock Di03-r785-t3) separated the 2P excitation from the 1P and imaging paths. A 594 nm long-pass dichroic (Semrock Di03-r594-t3) separated the 1P excitation light from the imaging path. Emission filters at 628/40 and 593/40 were used for imaging of JF_{608} and JF_{549}, respectively. Electrical waveforms and measurements were transduced through a computer-controlled data acquisition device (National Instruments, PCIe-6363). Galvo control and feedback waveforms were transduced through a second computer-controlled data acquisition device (National Instruments, PCIe-6343). The sample was placed on a motorized 2-axis stage, with focus controlled by objective displacement and a 3-axis micromanipulator used for patch pipette control (Sutter MPC-200 controller with MPC-78 stage and MP-285 manipulators).

Camera scaling was calibrated using a stage micrometer (Thorlabs, R1L3S2P), and illumination powers were calibrated using a power meter (Thorlabs, PM400) with either a photodiode (Thorlabs, S170C) or a thermal (Thorlabs, S175C) slide power sensor, for 1P and 2P, respectively.

2.5.6 Animals

All animal procedures adhered to the National Institutes of Health Guide for the care and use of laboratory animals and were approved by the Harvard University Institutional Animal Care and

Use Committee (IACUC).

In utero electroporation (IUE)

The IUE surgery was performed as described previously.[76] Timed-pregnant female CD1 mice (embryonic day 15.5, E15.5; Charles River) were deeply anesthetized and maintained with 2% isoflurane. The animal body temperature was maintained at 37 °C. Uterine horns were exposed and periodically rinsed with warm phosphate-buffered saline (PBS). Plasmid DNA was diluted in PBS (2 μg/μL; 0.05% fast green), and 1 μL of the mixture was injected into the left lateral ventricle of the embryos. Electrical pulses (40 V, 50 ms duration) targeting the hippocampus were delivered five times at 1 Hz using tweezers electroporation electrodes (CUY650P5; Nepa Gene). Injected embryos were returned to the abdominal cavity, and the surgical incision was closed with absorbable PGCL25 sutures (Patterson).

Cranial window surgery

Surgeries were conducted on NDNF-cre X NPY-GFP mice of both sexes, following the protocol outlined by[101]. The surgical procedure began by exposing the skull, followed by a 3 mm circular craniotomy at coordinates 3.3 – 3.4 mm lateral and 1.6 caudal relative to the bregma. The craniotomy was made using a dental drill. Following this, a stack of one 5 mm and two 3 mm round cover glass (Thomas Scientific, 1217N66), pre-glued by optical glue (Norland 61), was inserted into the opening. All subsequent experimental procedures were carried out at least one week post-surgery, ensuring that the health of each mouse was stable.

AAV injection

Following craniotomy, AAV virus (final titer ~4e12 GC/mL) was injected at a rate of 45 nL/min using a home-pulled micropipette (Sutter P1000 pipette puller) mounted in a microinjection pump (World Precision Instruments Nanoliter 2010) controlled by a micro-syringe pump controller (World Precision Instruments Micro4). The micropipette was positioned using a stereotaxic instrument (Sutter Instruments).

In Vivo Imaging

JF_{608}-HaloTag ligand solution was first prepared as previously described[97], and was then retro-orbitally delivered 24 hours before the imaging session. Mice were lightly anaesthetized (0.7-1% isoflurane) and head-fixed under the upright microscope using a titanium head plate. Eyes were kept moist using ophthalmic eye ointment. The body temperature was continuously monitored and maintained at 37°C using a heating pad (WPI, ATC-2000). A typical imaging session lasted 2-3 hours, after which the animals quickly recovered and were returned to their home cage.

2.5.7 Brain slice preparation

Coronal slices (300 μm) were prepared from CD1 mice of either sex between 2-4 postnatal weeks. Animals were anesthetized with isoflurane and euthanized by decapitation. The brain was then removed and placed in ice-chilled slicing solution containing (in mM): 210 sucrose, 3 KCl, 26 $NaHCO_3$, 1.25 NaH_2PO_4, 5 $MgCl_2$, 10 D-glucose, 3 sodium ascorbate, and 0.5 $CaCl_2$ (saturated with 95% O_2 and 5% CO_2). Acute slices were made using a Vibratome (VT1200S, Leica) while maintained in the slicing solution. Slices were recovered at 34 °C for 10 min in the imaging solution (artificial cerebrospinal fluid, ACSF) containing (in mM): 124 NaCl, 3 KCl, 26 $NaHCO_3$, 1.25 NaH_2PO_4, 2 $MgCl_2$, 15 D-glucose, and 2 $CaCl_2$ (saturated with 95% O_2 and 5% CO_2). Slices

were then incubated in ACSF containing JF_{608}-HaloTag ligand [102] (0.5-1 μM) for 30 min at room temperature, and moved to a fresh ACSF for another 30 min to wash out excess dye. Slices were maintained and recorded at room temperature, 24 °C.

2.5.8 Analysis

All analyses were performed using custom semi-automated MATLAB code. All automated analysis pipelines included a quality-control checkpoint at which key fits and values were manually checked. Analysis of 1P-only experiments began with manual selection of a membrane ROI from each cell. Analysis of experiments including 2P excitation began with automated selection of an ROI based on the 2P fluorescent signal. In both cases, the same ROI was used for each experiment from a given cell. Analysis proceeded by extracting a time trace of fluorescence by equal-weighted averaging of photon counts over the selected ROI followed by subtraction of the mean counts from a background region selected near the cell. The resulting one-dimensional time trace of fluorescence was used for all subsequent analyses. This trace was smoothed with a moving mean filter of window 20 ms for display of single voltage step responses and a moving mean filter of window 10 ms for calculation of the $\Delta F/F$ traces in Fig. 2.1l and Fig. 2.2d,e. Photobleaching was corrected using a bi-exponential fit to each illumination epoch. This fit provided the baseline from which values of ΔF were calculated, and which was used for normalization of $\Delta F/F$.

Neural spike recordings were detrended by smoothing the data with a moving mean filter of width 50 ms. This produced a smooth baseline from which $\Delta F/F$ could be calculated for the raw fluorescence trace. Spike heights, noise level, and fluorescence levels were manually extracted from all recordings before plotting. The logarithm of the SNR and per-cell counts were taken, and a linear fit was performed using MATLAB's curve fitting toolbox.

Significance of paired conditions was calculated using a two-tailed paired sample t-test, and significance of unpaired data was calculated using a two-tailed two-sample t-test, both using MATLAB's

machine learning and statistics toolbox.

2.6 Manuscript Information

2.6.1 Previously published as

A version of this chapter appeared in [103]:

Brooks, F. P., Davis, H. C., Park, P., Qi, Y., Cohen, A. E. Photophysics-informed two-photon voltage imaging using FRET-opsin voltage indicators. Preprint at https://doi.org/10.1101/2024.04.01.587540 (2024).

This work has been submitted for publication.

2.6.2 Acknowledgements

We thank Daniel Itkis, Andrew Preecha, Shahinoor Begum, David Wong-Campos, Byung Hun Lee, and Ethan Perets for technical assistance and helpful discussions. This work was supported by NIH grants 1R01NS133755, 1RF1NS126043, and NSF Quantum Sensing for Biophysics and Bioengineering (QuBBE) Quantum Leap Challenge Institute (QLCI) grant OMA-2121044.

2.6.3 The author's contributions

Frederick Brooks, Hunter Davis, and Adam E. Cohen designed the study and experiments. Frederick Brooks and Adam E. Cohen wrote the manuscript with input from all authors. Frederick Brooks collected the 1P data. Frederick Brooks and Hunter Davis collected the 2P HEK-293T data. Pojeong Park prepared the I.U.E construct, performed I.U.E, prepared brain slices, and assisted Frederick Brooks with data collection for 2P acute slice imaging. Yitong Qi prepared the AAV construct, conducted virus injection and cranial window surgery and assisted Frederick Brooks with

data collection for 2P *in vivo* imaging. Frederick Brooks performed all analyses with critical input from Hunter Davis and Adam E. Cohen. Adam E. Cohen supervised the work.

3

Optical constraints on two-photon voltage imaging

3.1 Abstract

3.1.1 Significance

Genetically encoded voltage indicators (GEVIs) are a valuable tool for studying neural circuits *in vivo*, but the relative merits and limitations of one-photon (1P) vs. two-photon (2P) voltage imaging are not well characterized.

3.1.2 Aim

We consider the optical and biophysical constraints particular to 1P and 2P voltage imaging and compare the imaging properties of commonly used GEVIs under 1P and 2P excitation.

3.1.3 Approach

We measure brightness and voltage sensitivity of voltage indicators from commonly used classes under 1P and 2P illumination. We also measure the decrease in fluorescence as a function of depth in mouse brain. We develop a simple model of the number of measurable cells as a function of reporter properties, imaging parameters, and desired signal-to-noise ratio (SNR). We then discuss how the performance of voltage imaging would be affected by sensor improvements and by recently intro-

duced advanced imaging modalities.

3.1.4 Results

Compared to 1P excitation, 2P excitation requires $\sim 10^4$-fold more illumination power per cell to produce similar photon count rates. For voltage imaging with JEDI-2P in mouse cortex with a target SNR of 10 (spike height:baseline shot noise), a measurement bandwidth of 1 kHz, a thermally limited laser power of 200 mW, and an imaging depth of > 300 μm, 2P voltage imaging using an 80 MHz source can record from no more 12 cells simultaneously.

3.1.5 Conclusion

Due to the stringent photon-count requirements of voltage imaging and the modest voltage sensitivity of existing reporters, 2P voltage imaging *in vivo* faces a stringent tradeoff between shot noise and tissue photodamage. 2P imaging of hundreds of neurons with high SNR at depth > 300 μm will require either major improvements in 2P GEVIs or qualitatively new approaches to imaging.

3.2 Introduction

A longstanding dream in neuroscience has been to record the membrane potential of hundreds or thousands of neurons simultaneously in a behaving animal. Such measurements could reveal functional connections, probe input-output properties of cells and of microcircuits, and help discern principles of neural computation. Recent advances in GEVIs have substantially improved their signal-to-noise ratio (SNR), enabling recordings from dozens of cells in superficial tissue using one-photon imaging[18,43,69]. There have also been improvements in instrumentation[68,104] and reporters[38] for 2P voltage imaging, enabling voltage imaging at depths up to 500 μm, though the number of simultaneously recorded cells at this depth remains < 3. Most applications of voltage

imaging *in vivo* have been with 1P excitation [16,73,105,106], whereas for Ca^{2+} imaging, 2P microscopy is the dominant approach. [107] This raises the question: what are the scaling properties and relative merits of 1P vs 2P voltage imaging *in vivo*? How can a researcher considering a voltage imaging experiment decide which approach to use?

The physical requirements of Ca^{2+} imaging and voltage imaging differ substantially, so intuitions may not transfer. For Ca^{2+} imaging, typical events last 100 – 500 ms and have amplitudes of $\Delta F/F$ ~100%. Signals come from the bulk cytoplasm. For voltage imaging, action potentials last ~0.3 – 2 ms, and typically have amplitudes of $\Delta F/F \sim$ 10 - 30%, though subthreshold events can be 100-fold smaller. Signals are localized to the cell membrane. Thus, the key challenge in voltage imaging is to acquire adequate SNR and imaging speed in the presence of shot-noise and motion artifacts, while maintaining tissue-safe laser powers.

Here we explore, with the support of mathematical models and data from representative voltage indicators, how molecular and optical parameters affect the balance between SNR, number of simultaneously recordable cells, and tissue damage. Many of the arguments about scaling of noise [108,109] and 2P signal [56,99] are found elsewhere in the literature, but with the recent publications seeking to reach [63–66,70,71,110] or transcend [67,111–114] these limits, we believe a consolidation of the arguments with a specific application to voltage imaging is warranted.

Our results support the preference for 1P over 2P imaging at shallow depths and the use of 2P voltage imaging at depths where 1P recordings are inaccessible due to light scattering. However, at depths beyond the 1P limit, 2P voltage imaging signals are severely constrained by thermal and shot-noise limits. We address the potential of advanced instrumentation and analysis techniques to improve performance beyond current limits.

3.3 Materials and Methods

3.3.1 HEK cell culture

HEK293T cells were maintained at 37 °C, 5% CO_2 in Dulbecco's Modified Eagle Medium supplemented with 10% fetal bovine serum, 1% GlutaMax-I, penicillin (100 U/mL), streptomycin (100 mg/mL). For maintaining or expanding the cell culture, we used 35 mm TC-treated culture dish (Corning). For each imaging experiment, cells in one 35 mm dish were transiently transfected with the construct to be imaged using PEI in a 3:1 PEI:DNA mass ratio. For all the imaging experiments, cells were replated on glass-bottomed dishes (Cellvis, D35-14-1.5-N) 36 hours after transfection. Imaging was performed ~6 hours after replating. Before optical stimulation and imaging, the medium was replaced with extracellular (XC) buffer containing 125 mM NaCl, 2.5 mM KCl, 3 mM $CaCl_2$, 1 mM $MgCl_2$, 15 mM HEPES, 30 mM glucose (pH 7.3). For BeRST1 experiments in HEK cells, cells were stained with 1 μN BeRST1 for 30 min prior to 3x wash with XC buffer before imaging.

3.3.2 Microscope and illumination control

All imaging was performed using Luminos bi-directional microscopy control software (see chapter 4) on a custom-built upright microscope equipped with 1P and 2P illumination paths and a shared emission path to an sCMOS camera (Hamamatsu, ORCA-Flash 4.0 v2). The 1P illumination path contained a 488 nm laser (Coherent OBIS), a 532 nm laser (Laserglow LLS-0532) and a 635 nm laser (Coherent OBIS). The outputs of the 488 nm and 532 nm lasers were modulated using a multichannel acousto-optic tunable filter (Gooch & Housego PCAOM NI VIS driven by G&H MSD040-150). The 635 nm laser was modulated using its analog modulation input and an external neutral density filter wheel (Thorlabs). The 488 nm and 532 nm lasers were patterned via a

Digital Micromirror Display (Vialux V-7001 V-module). To convert illumination intensity to power per cell, we approximated HEK cells as circles with a 10 μm diameter, e.g. an intensity of 1 W/cm2 corresponded to 0.8 μW per cell.

The two-photon illumination path comprised an 80 MHz tunable femtosecond laser (InSight DeepSee, Spectra Physics), an electro-optic modulator (ConOptics 350-80-02) and two galvo mirrors for steering (Cambridge Technology 6215H driven by 6671HP driver). Power calibration was performed with a Thorlabs PM400 power meter with a photodiode-based sensor (S170C) and a thermal sensor (S175C) for 1P and 2P illumination, respectively. Electrical stimuli and measurements were performed using a National Instruments 6063 PCIe DAQ. All imaging was performed with a 25x water immersion objective (Olympus XLPLN25XWMP2, 2mm working distance, NA 1.05). At each wavelength, the dispersion was adjusted to maximize the 2P fluorescence signal. The wavelengths for 2P excitation of QuasAr6a and BeRST1 were chosen to drive the S_0 to S_2 transition rather than the S_0 to S_1 transition because the S_2 transition was stronger.

3.3.3 Measuring voltage-sensitive fluorescence in vitro

All imaging and electrophysiology experiments were performed in XC buffer. Concurrent whole-cell patch clamp and fluorescence recordings were acquired on the microscope described above. Filamented glass micropipettes were pulled to a tip resistance of 5–8 MΩ and filled with internal solution containing 125 mM potassium gluconate, 8 mM NaCl, 0.6 mM $MgCl_2$, 0.1 mM $CaCl_2$, 1 mM EGTA, 10 mM HEPES, 4 mM Mg-ATP and 0.4 mM Na-GTP (pH 7.3), adjusted to 295 mOsm with sucrose. Whole-cell patch clamp recordings were performed with an Axopatch 200B amplifier (Molecular Devices). Fluorescence was recorded in response to a square wave from -70 mV to +30 mV.

3.3.4 In-house AAV packaging

AAV2/9 JEDI-2P vectors were packaged in house based on a published protocol.[115] Briefly, 50 ∼ 70% confluent HEK293T cells grown in Dulbecco's Modified Eagle Medium supplemented with 5% FBS were triple transfected with pHelper, pAAV ITRexpression, and pAAV Rep-Cap plasmids using acidified (pH 4) PEI (DNA:PEI ratio 1:3) in 1∼2 T175 flasks (∼2 x 10^7 cells/flask). The AAV-containing medium was harvested on Day 3, and the AAV-containing medium and cells were harvested on Day 5. For the second harvest, AAVs were released from the cells with citrate buffer (55 mM citric acid, 55 mM sodium citrate, 800 mM NaCl, 3 mL per flask). The two harvests were then combined and precipitated overnight with PEG/NaCl (5x, 40% PEG 8000 (w/v), 2.5 M NaCl) at 4 °C. The low-titer virus was then purified with chloroform extraction (viral suspension and chloroform 1:1 (v/v)), aqueous two-phase partitioning (per 1 g of the AAV-containing supernatant, add 5 g of 20% $(NH_4)_2SO_4$ solution and 1.5 g of 50% PEG 8000 solution, and iodixanol discontinuous gradient centrifugation (15%, 25%, 40%, and 54% iodixanol gradient prepared from OptiPrep (60% (w/v) Iodixanol, Axis-Shield PoC AS). The purified AAV titer was determined via qPCR (SYBR Green, primer for forward ITR: 5'-GGAACCCCTAGTGATGGAGTT-3'; primer for reverse ITR sequence 5'- CGGCCTCAGTGAGCGA-3').

3.3.5 *In vivo* imaging

All animal experiments were approved by the Institutional Animal Care and Use Committee of Harvard University. The cranial window surgery for *in vivo* imaging was based on previously published protocols[73]. Briefly, an adult CD1 mouse was injected with 50 nL viral mix in 4 sites in the whisker barrel cortex at 100, 200, 300, 400, and 500 μm below the tissue surface. Viral mix had a final concentration of 5e12 vg/mL pAAV-EF1a-DIO-JEDI-2P-Kv2.1motif and 1e11 CamKII-Cre in AAV 2/9. A cranial window and mounting plate were then installed over the injection sites.

Two weeks after surgery and injection, a head fixed CD1 mouse was imaged at 1.5% isoflurane with the dose adjusted to maintain a stable breathing rate. The mouse was kept on a heating pad (WPI ATC2000) to maintain stable body temperature at 37 °C and its eyes were kept moist using ophthalmic eye ointment. 2P imaging was performed at a wavelength of 930 nm. The mouse was imaged for 2 hours after which it recovered in less than 10 minutes.

Light for 1P imaging *in vivo* was patterned via a digital micromirror device to selectively illuminate the targeted cell body, as described above.

3.4 Results

3.4.1 Shot noise constrains functional fluorescence imaging

Shot noise imposes a fundamental limit on imaging performance. A source that generates, on average, N detected photons, will have fluctuations with standard deviation $\sqrt{N}$. To detect a 1 ms spike ($\Delta F/F \sim 10\%$) with an SNR of 10, requires determining fluorescence to 1% precision in 1 ms. We adopt 1% precision in 1 ms as a reasonable standard for a high-SNR voltage recording. Due to shot noise, this standard requires detecting at least 10^4 photons/ms, or 10^7 photons/s.

More generally, imaging an event of magnitude $\Delta F/F = \beta$ with a given SNR requires determining fluorescence to a precision of β/SNR. The photon flux (Γ) required for a measurement rate (f), signal level (β), and SNR is:

$$\Gamma = f \cdot (\frac{SNR}{\beta})^2 \tag{3.1}$$

If one wishes only to detect spikes in pyramidal cells, one might tolerate SNR = 3 and f = 400 Hz. A highly sensitive GEVI could give β = 0.2 for a spike.[38] Under these conditions, the minimum detection rate is $\Gamma = 9 \times 10^4$ photons/s. In comparison, for a typical calcium imaging scenario,

SNR = 10, β = 1 and f = 30 Hz,[47] implying Γ = 3000 photons/s, 30-fold less than even low-SNR spike detection via voltage imaging. Thus, the brief duration of voltage spikes and the low fractional sensitivity of existing voltage indicators conspire to make voltage imaging a very photon-greedy technique.

Filtering in space or time can increase the effective value of N at a given pixel, at the cost of lower spatial or temporal resolution, but filtering does not change the $\sqrt{N}$ shot noise scaling. We discuss advanced analysis techniques below.

3.4.2 1P vs 2P excitation of commonly used voltage indicators

We compared the brightness of commonly used voltage indicators in HEK293T (HEK) cells under alternating wide-field one-photon illumination and two-photon spiral illumination with an 80 MHz pulsed laser, using a shared detection path for both modalities to ensure equal photon detection efficiencies (Fig. 3.1a-c; Methods). We compared: a voltage sensitive dye (BeRST1[116]), an opsin-derived GEVI imaged via intrinsic retinal fluorescence (QuasAr6a[117]), a chemigenetic FRET-opsin GEVI (Voltron2[44]), and two GEVIs that couple a voltage sensitive phosphatase (VSP) to a circularly permuted partner fluorophore (ASAP3[104] and JEDI-2P[38]).

As expected, the fluorescence scaled linearly with 1P illumination intensity and quadratically with 2P intensity (Fig. 3.1d). For all but one indicator, 2P illumination required at least 10^4-fold greater time-averaged power per cell to achieve comparable counts to 1P illumination (Fig. 3.1e). The ratio of 2P to 1P powers for QuasAr6a was only ~300, due to the requirement for high intensity 1P illumination and selection rules which favor 2P over 1P excitation in opsins.[118] Consistent with prior reports,[43] we found that chemigenetic indicators were brighter under both 1P and 2P illumination than their purely protein-based counterparts, though our measurements did not assign the relative contributions of expression level vs. per-molecule brightness.

The huge difference in optical power requirement between 1P and 2P (80 MHz) excitation

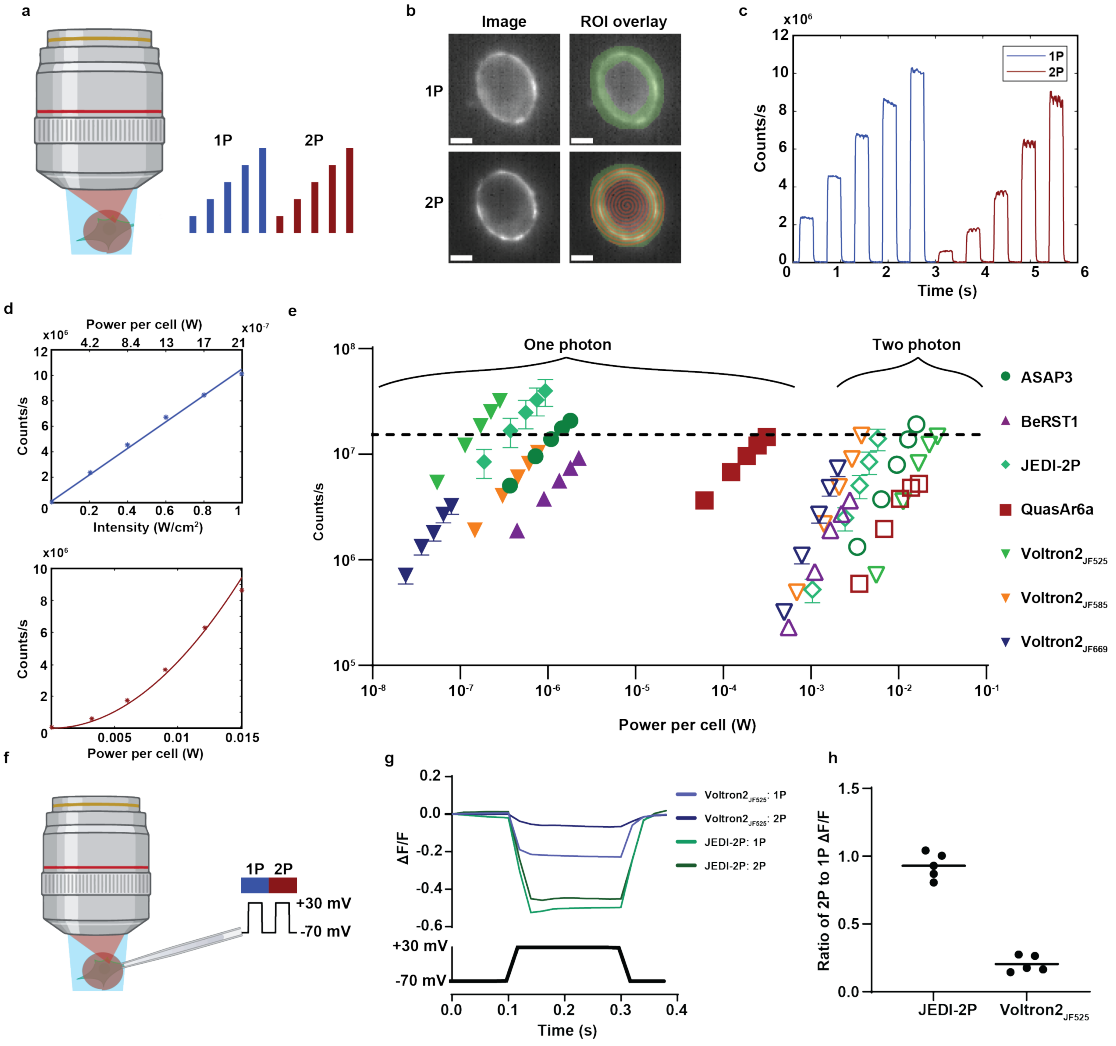

Figure 3.1: a) Diagram of experiment. HEK cells were sequentially illuminated with wide-field 1P light in steps of increasing intensity, then by spiral scan 2P steps of increasing intensity. b) Example HEK cell expressing the GEVI ASAP3. 2P spiral scan pattern shown in red and analysis ROI shown in green. Scale bars 5 μm. c) Example single-trial data for cell expressing ASAP3. d) Top: fluorescence in c as a function of 1P intensity with linear fit. Bottom: fluorescence as a function of 2P power with quadratic fit. e) Log-log plot of count rate vs. optical power on the cell for seven voltage indicators. 1P data: filled symbols, 2P data: empty symbols. Error bars are SEM from at least n = 8 cells. The excitation wavelengths used for 1P (2P) excitation of each of the reporters were: ASAP3 488 nm (930 nm), BeRST1 635 nm (850 nm), JEDI-2P 488 nm (930 nm), QuasAr6a 635 nm (900 nm), Voltron2$_{525}$ 488 nm (930 nm), Voltron2$_{585}$ 594 nm (1100 nm), Voltron2$_{669}$ 635 nm (1220 nm). A horizontal line is shown at 1.5x10^7 counts/s, equivalent on our camera to 10^7 impinging photons/s. f) Whole-cell patch clamp protocol for measuring voltage sensitivity under 1P and 2P excitation. g) Average voltage responses of JEDI-2P and Voltron2$_{525}$ under 1P and 2P illumination. h) Ratio of voltage contrast under 2P vs. 1P illumination for JEDI-2P and Voltron2$_{525}$, n = 5 cells per construct.

is consistent with published reports: 2P imaging of JEDI-2P was reported at a power of 9 – 12 mW/cell[38], whereas 1P imaging of similar GFP-based GEVIs is typically performed at 1 – 10 W/cm^2,[38,104] corresponding to 1 – 10 μW/cell. Estimates based on tabulated 1P and 2P absorption coefficients[119] give a similar factor of $\sim 10^4$ difference in power efficiency (Appendix A).

We then measured voltage sensitivity of one representative from each GEVI family, comparing 1P and 2P illumination. Using whole-cell voltage clamp in HEK cells (Fig. 3.1f), we found that the contrast (ΔF/F per 100 mV) of the VSP-based JEDI-2P was similar for 1P and 2P illumination. The opsin-based chemigenetic indicator Voltron2$_{525}$ showed voltage sensitivity under 1P but not 2P illumination (Fig. 3.1g-h). Loss of voltage sensitivity under 2P illumination of FRET-Opsin GEVIs has been reported previously[60], but the mechanism is unknown (see chapter 2).

3.4.3 Testing the dependence of 1P and 2P signal as a function of depth

To characterize the depth dependence of 1P and 2P voltage imaging in brain tissue, we sparsely expressed soma-localized JEDI-2P in mouse cortex. Chien et al. previously showed that for voltage imaging in brain tissue, restricting 1P illumination to the soma led to an $\sim$8-fold improvement in signal-to-background ratio compared to wide-field illumination, by minimizing background from off-target illumination.[84] We thus compared soma-targeted 1P imaging and raster-scanned 2P imaging at several depths (Fig. 3.2a-b; Methods).

With 1P illumination, JEDI-2P-expressing cells were resolvable down to $d \sim 200$ μm. The challenge for 1P imaging at greater depths was not shot noise, but rather decrease in signal-to-background ratio. At depths > 200 μm, cells were not distinguishable from background by 1P imaging with patterned 488 nm excitation (Fig. 3.2c).

With 2P illumination, cells were resolvable to d = 473 μm, the greatest depth we tested (Fig. 3.2b). As the cell depth increased, we increased the 2P laser power to maintain sufficient count rate to resolve the cells, up to P_o = 140 mW at d = 473 μm.

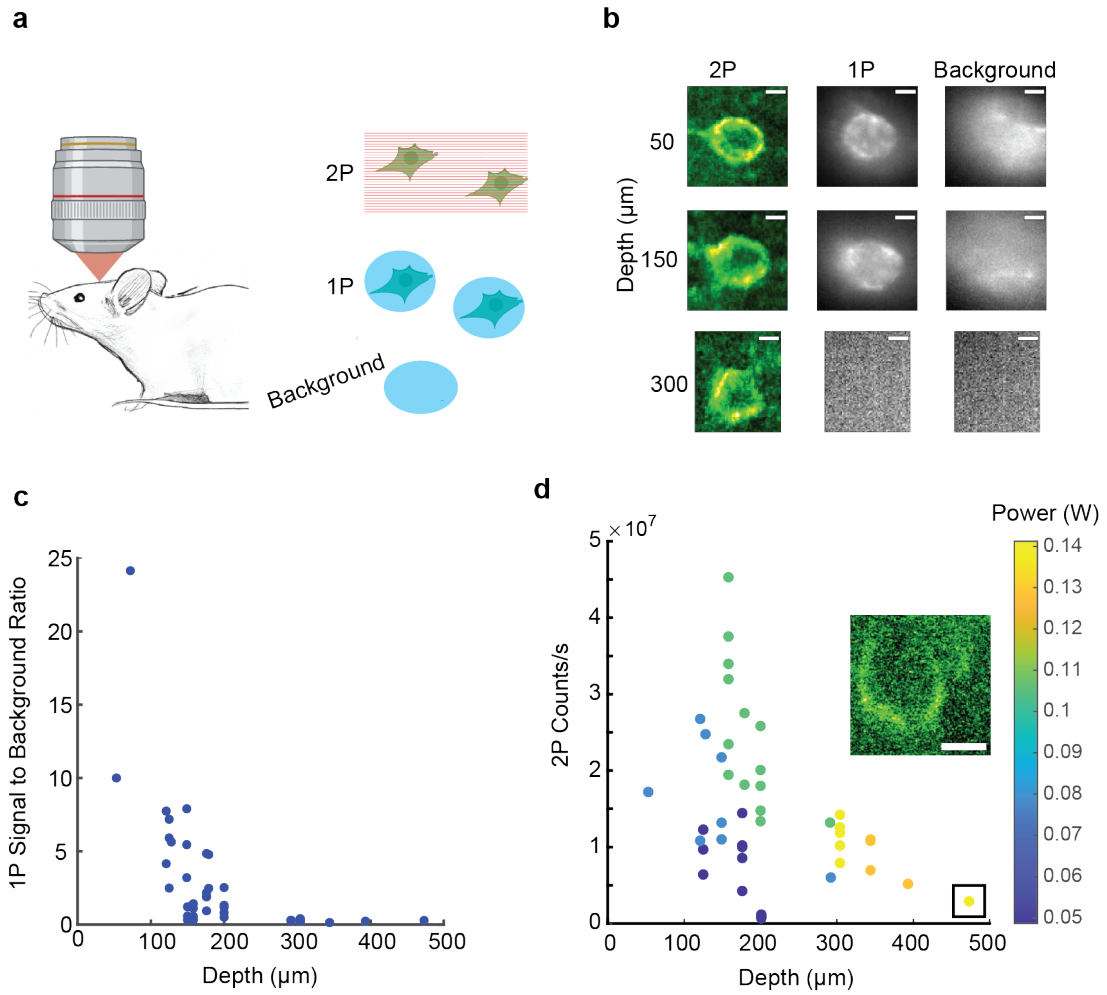

Figure 3.2: a) Experimental protocol. In a mouse expressing JEDI-2P, raster-scanned 2P (λ = 920 nm) and DMD-patterned 1P imaging (λ = 488 nm) were alternately applied to neurons at different depths. 1P illumination patterned to cell-free regions was used to estimate background signal. b) Example 1P and 2P images of cells at three depths. Scale bars 5 μm. c) Estimated signal-to-background ratio for n = 43 neurons under patterned 1P illumination. d) Mean count rate from the membranes of n = 43 neurons under 2P illumination. Color indicates excitation power. Inset shows cell at 473 μm depth. (Scale bar 5 μm).

3.4.4 Limits to 2P excitation power in brain tissue

The heating caused by 2P illumination can transiently perturb neural function, and at high levels can damage tissue. Most ion channel gating properties have a Q_{10} (i.e. ratio of rates at temperatures separated by 10 °C) between 1 and 3.[120] Changes of 1°C can cause changes in neuronal firing rates.[121] In rodents, brain temperature may fluctuate under physiological conditions by up to 4 °C.[122] Podgorski and Ranganathan[98] found lasting damage after continuous illumination of a 1 mm² scan at 250 mW, corresponding to a steady-state temperature change of ∼5 °C.

The relation between laser power and heating depends on scan area, scan pattern, and measurement duty cycle. For a 1 mm² square scan pattern, Podgorski and Ranganathan found steady-state temperature coefficients between 0.012 and 0.02 °C/mW at wavelengths from 800 – 1040 nm, equivalent to a temperature rise of < 2 °C at 100 mW illumination. They simulated the dependence of temperature rise on scan area and found a weak dependence. Their results predict a maximum temperature coefficient of 0.03 °C/mW for a square scan of side length 20 μm (representing a single neuronal soma). The precise value of this coefficient depends both on the brain region and the wavelength[54]. Finally, Podgorski and Ranganathan show that reducing the illumination duty-cycle to 10 s on, 20 s off, allowed brighter illumination to be used during "on" periods, while still keeping time-averaged heating beneath the damage threshold. Some experiments may permit low duty-cycle imaging while others may not. Hereafter we use 200 mW as a reasonable upper bound on the power, acknowledging that this limit may be higher (or lower) depending on many experimental details.

3.4.5 Estimating measurable cells as a function of depth

Shot noise places an upper bound, N_{cells}^{2P}, on the number of cells which can be measured simultaneously via 2P illumination with a given illumination power and SNR. Under a protocol which

sequentially visits single cells, N_{cells}^{2P} depends on both the brightness and voltage sensitivity (see Appendix A for derivation):

$$N_{cells}^{2P} = \frac{A \cdot \tau \cdot P^2 \cdot \beta^2 \varphi}{SNR^2} \tag{3.2}$$

Here A is the brightness coefficient derived from the HEK cell experiments (Eq. A.1), τ is the integration time, P is the laser power at the focus, β = ΔF/F per spike, φ is the fraction of the scan that intersects with the cell membrane (i.e. the imaging duty cycle), and SNR is the target ratio of the spike amplitude to shot noise. The value of A is specific to the laser repetition rate, pulse width, focal parameters, and detection optics. We discuss the effects of varying these parameters below. For an analysis that includes the effect of light scattering on depth-dependent collection efficiency, see [56].

The parameter φ approaches 1 for perfectly membrane-targeted illumination. To estimate φ for a raster scan over a bounding box around a single cell body, we examined 2P images of pyramidal cells with membrane-targeted fluorescent tags in cortex layer 2/3. In these images, the membrane-labeled area fraction within the bounding box was φ_{bb} = 0.18 ± 0.07 (mean ± std, n = 10 cells). For a raster scan over multiple sparsely expressing cells, φ is lower than φ_{bb} by a factor of the sparsity. The low values of φ for raster-scanned 2P imaging are a consequence of the membrane-localized signal and highlight the importance of membrane-targeted illumination. However, precise targeting of the illumination to the membrane increases sensitivity to motion artifacts. The ULoVE technique brackets the membrane with pairs of spots and thereby mitigates the effect of small motions. [104]

Eq. 3.2 can be used to predict the scaling of N_{cells}^{2P} as a function of depth, d, for 2P voltage imaging. The power at a laser focus decays exponentially with d, with an extinction length, l_e, in brain tissue. At λ = 920 nm l_e is between 112 [56,123] and 155 μm. [124] Due to the quadratic dependence of 2P signal on focal intensity, the 2P signal decays with a length constant of $l_e/2$. Substituting $P = P_0 e^{-d/l_e}$ into Eq. 3.2 implies a decay in N_{cells}^{2P} by a factor of 10 for every 130 - 180 μm increase

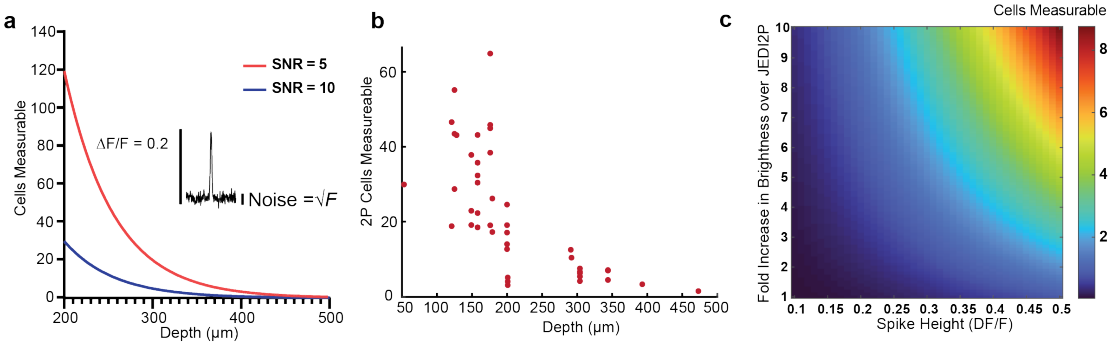

Figure 3.3: a) Predicted number of simultaneously measurable cells as a function of depth, based on brightness derived from HEK cells expressing JEDI-2P (Fig. 3.1). We assumed a spike contrast of β = 0.2, target SNR of 5 (blue) or 10 (red) in an integration time τ = 1 ms, a total power P_0 = 200 mW, targeting fraction φ = 1, scattering length l_e = 112 μm [123], and a detector with perfect quantum efficiency. b) Predicted number of simultaneously measurable cells at SNR=10 and 200 mW power for each experimentally-measured single-cell count-rate reported in (Fig. 3.2d). c) Number of simultaneously measurable cells under 2P illumination at a depth of 500 μm, assuming brightness and contrast improvements of future GEVIs, target SNR of 10, and all other parameters as in (a).

in d (Fig. 3.3a), assuming constant power P_0 into the tissue.

We applied Eq. 3.2 to the instantaneous count rates measured from the cell membranes (Fig. 3.2d) to estimate N^{2P}_{cells} for $\varphi \sim 1$, i.e., a perfectly membrane-targeted annular scan pattern. We converted the digital count rates to impinging photon rates to provide an upper bound of performance for a perfect detector. Modern scientific cameras come quite close to perfect detection efficiency. We assumed β = 0.2, based on the reported spike response of JEDI-2P [38] and a target shot noise-limited SNR of 10 in a 1 kHz bandwidth, and extrapolated the count rates to an input power of Po = 200 mW. The estimated number of measurable cells decreased quickly at d > 200 μm and dropped below three at d > 470 μm and input power 200 mW (Fig. 3.3b). These results are similar to the prediction from the simple model using the 2P count rates from our HEK cell experiments (Fig. 3.3a, blue line).

The palette of available voltage indicators is continually improving. [125] We therefore considered the scaling of N^{2P}_{cells} with changes of brightness and spike height (β). N^{2P}_{cells} depends linearly on A and quadratically on β (Fig. 3.3c). An order-of-magnitude increase in molecular brightness coupled with

a 2.5 fold increase in β compared to JEDI-2P could enable high SNR measurement of >8 cells at depths up to 500 μm.

3.4.6 Effect of GEVI kinetics

Some GEVIs have response times that are slow compared to the duration of a spike. On one hand, this blunts the amplitude of the spike response; on the other, it permits one to average for longer to detect whether a spike has occurred (assuming that the interval between spikes remains long compared to the response time of the GEVI). Here we analyze this tradeoff.

Consider a GEVI subjected to a voltage step which induces a steady-state change in fluorescence, $\frac{\Delta F}{F} = M$. Assume that the GEVI responds to a voltage step of length t with exponential response time constants τ_{on} and τ_{off} (Fig. 3.4a,b). We can then write the total integrated fractional response, R, as (see Appendix A for derivation):

$$R = M\left(t + \left(\tau_{off} - \tau_{on}\right)\left(1 - e^{-t/\tau_{on}}\right)\right) \tag{3.3}$$

Eq. 3.3 assumes collection of the entire tail of the decay. Collection will have to be truncated after a finite integration time, so Eq. 3.3 will provide an upper bound to signal. Assuming an integration time equal to $t + \tau_{off}$, we can express the SNR in terms of R as (see Appendix A for derivation):

$$SNR = \frac{RF\varphi}{\sqrt{F\varphi\left(t + \tau_{off}\right)}} \tag{3.4}$$

A large τ_{on} will decrease the magnitude of the response β to a short electrical spike, decreasing instantaneous SNR proportionally. A large τ_{off}, however, increases the duration of the impulse response function, increasing the duration of the signal that can be integrated, leading to an increase in SNR with the square root of τ_{off} (Eq. A.7, Fig. 3.4c). When τ_{on} and τ_{off} can be independently

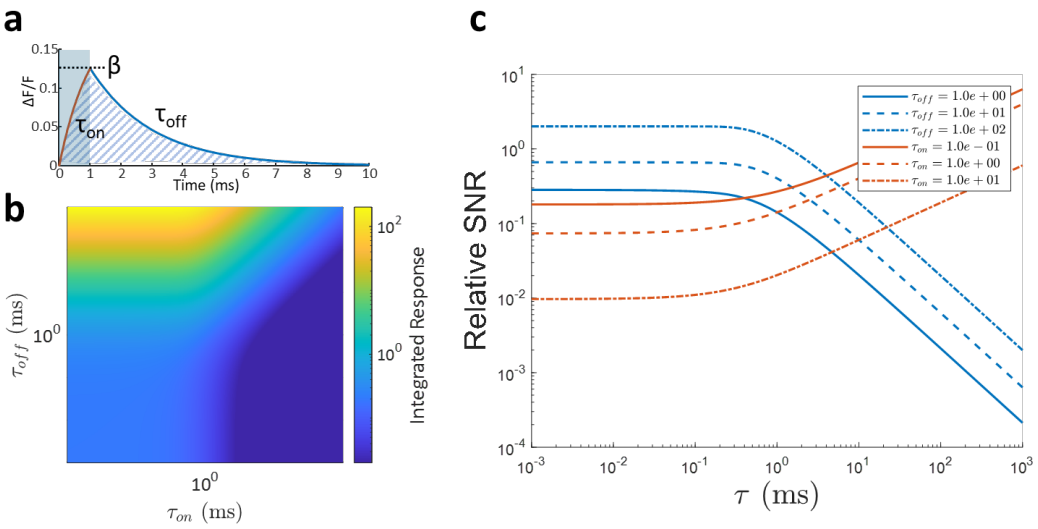

Figure 3.4: a) The response of a reporter to a 1 ms voltage stimulus. An exponential rise with time constant τ_{on} reaching a maximum of β followed by an exponential decay with time constant τ_{off}. The total area under both response phases (cross-hatched) is the total available response signal. b) The total area under the curve in (a) as a function of τ_{on} and τ_{off}. Increasing τ_{off} allows longer integration time, while increasing τ_{on} truncates the response. c) The effects on SNR of changing τ_{on} or τ_{off} with the other fixed. At large values, the dependence of SNR on τ_{on} has an exponent of -1, while at large values, the dependence of SNR on τ_{off} has an exponent of -1/2.

chosen, τ_{on} should be minimized (with diminished effect once τ_{on} is well below the spike width) and τ_{off} maximized subject to the inter spike interval. Often, these time constants are biophysically related. In the case of comparable $\tau_{on} \approx \tau_{off} = \tau$, it follows that $SNR \sim \tau^{-1/2}$ (see Eq. A.7). That is, faster GEVIs are better than slower ones in terms of shot noise-limited SNR, all else being equal.

3.4.7 Effect of optical parameters on 2P fluorescence

Advances in 2P voltage imaging typically have two aims: 1) increasing the number of cells, N, which are sampled with high enough revisit rate to capture all electrical dynamics; and 2) increasing fluorescence per cell to improve the shot noise-limited SNR. In many cases, these two aims are in tension.

Changing numerical aperture

We distinguish between numerical aperture of excitation (NA_e) and of collection (NA_c). Often, NA_c is set by the objective NA, while NA_e may be lower as a result of underfilling the objective back aperture. The photon detection efficiency, PDE, scales as $PDE \sim {NA_c}^2$. The effect of excitation numerical aperture (NA_e) on the 2P signal depends on the sample geometry. Within the Gaussian beam approximation (Fig. 3.5a), the width of the focus scales as

$$w_0 \propto \frac{1}{NA_e}$$

The intensity, I, at the focus scales inversely with the cross-sectional area (so $I \propto NA_e^2$), and the rate of 2P excitation per molecule, E, scales with the intensity squared. Hence

$$E \propto NA_e^4$$

The axial extent of the beam waist scales as

$$b \propto \frac{1}{NA_e^2}$$

The total signal from a volume element depends on the number of fluorophores excited. In a three-dimensional bulk solution, an approximation of 2P Ca^{2+} imaging when the beam waist is significantly smaller than a single cell, the volume scales approximately as $V \sim w_0^2\, b \propto \frac{1}{NA_e^4}$. The total fluorescence emission τ_{2P} scales as $V \times E$. Hence, in bulk solution, $\Gamma_{2P} \propto NA_e^0$, so that the total collected fluorescence, F, scales only with NA_c as $F \sim NA_c^2$.

In contrast, for 2P voltage imaging, the signal scales with NA_e raised to a power between 1 and 3, depending upon the orientation and geometry of the membranes in the focal spot (Fig. 3.5b, first row). This scaling argues strongly for maximizing the NA_e for 2P voltage imaging. On the other

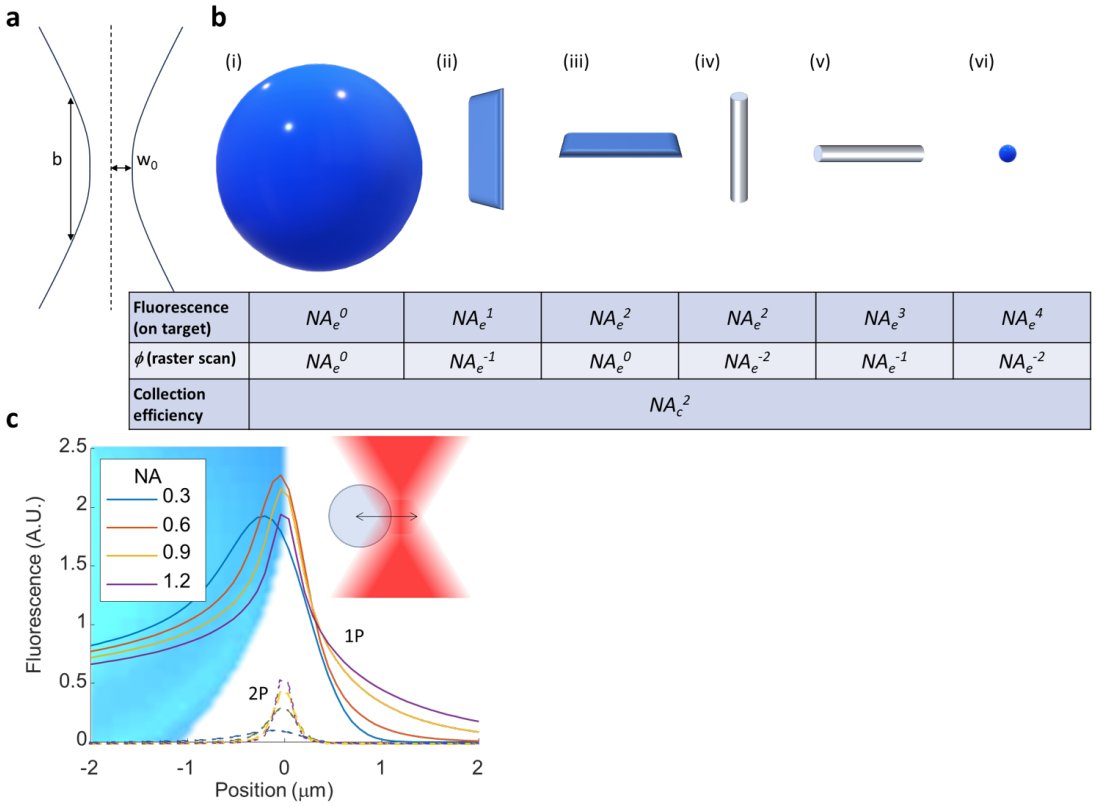

Fluorescence (on target)	NA_e^0	NA_e^1	NA_e^2	NA_e^2	NA_e^3	NA_e^4
ϕ (raster scan)	NA_e^0	NA_e^{-1}	NA_e^0	NA_e^{-2}	NA_e^{-1}	NA_e^{-2}
Collection efficiency	NA_c^2					

Figure 3.5: a) Geometry of a Gaussian beam, showing the width ($w_0 \sim 1/NA$) and waist ($b \sim 1/NA^2$). b) Scaling of total 2P fluorescence as a function of excitation NA_e for different sample geometries. All slender dimensions are assumed to be $\ll w_0$ and all extended dimensions are assumed to be $\gg b$. In a planar raster scan, the fraction of time that a sub-wavelength structure is excited, φ, depends on the focus width and hence the NA_e. In cases (iii), (v), and (vi) we assume that the object is perfectly in focus, i.e., in the axial plane where focus size is minimum. The collection efficiency for all geometries depends on the collection solid angle $\sim NA_c^2$. To calculate total signal for targeted illumination, multiply the first and third lines; for a raster scan, multiply all three lines. c) Total fluorescence evoked by the intersection of a laser focus and a spherical membrane, 10 μm diameter. We compared 1P and 2P excitation with equal NA_c and NA_e, with powers adjusted to match per-molecule excitation rates at the focus at NA = 1.2. The much smaller 2P focal volume led to 5.3-fold smaller maximum fluorescence at the highest NA (and even greater discrepancy at lower NA) and 3-fold greater sensitivity to misalignment, compared to 1P excitation.

hand, a smaller excitation spot leads to (a) a higher rate of photobleaching and (b) greater sensitivity to misalignment between the focus and the sample, e.g., from sample motion (Fig. 3.5c).

Advanced scanning modalities

State-of-the-art techniques for high-speed 2P microscopy often involve shaping and splitting the excitation in space and time[68,70,104,126,127]. While these techniques are powerful ways to increase the speed (f), targeting efficiency (φ), and robustness to motion of the microscope, they cannot surpass the SNR of a sequential point-focus scan at a given total power, pulse width and repetition rate. If, however, the system is limited not by the total power but by non-linear photodamage and saturation of the 2P excitation, splitting the pulse in space and/or time can allow more power to be safely delivered and can therefore increase SNR. This manuscript focuses on the optical SNR limits of voltage imaging. If the number of cells measurable is constrained to a lower limit by scanning speed, better performance may be achieved with a non-point-scanning technique. Here we discuss the effects on optical SNR of changes to instrumentation.

Spatial and temporal focal multiplexing

Both spatial and temporal splitting of a single focal pulse involve a reduction in per-focal-pulse energy (at constant total power) in return for a proportional increase in the number of focal pulses imaged per second. It is convenient to define an effective repetition rate, f_{eff}, as the product of the temporal repetition rate with the degree of spatial multiplexing. A system that performs 4x temporal and 2x spatial multiplexing of a 31.25 MHz laser will have an effective repetition rate of 250 MHz.[67] At a fixed power, increasing f_{eff} proportionally decreases the energy delivered to each focal pulse, ε (Fig. 3.6a). Since 2P fluorescence scales with the square of pulse energy, but only linearly with the number of focal pulses, fluorescence (and SNR) can be maximized by minimizing f_{eff} and

maximizing ε. An N-fold decrease in effective repetition rate will lead to a $\sqrt{N}$-fold increase in measurable cells at fixed power. This is consistent with a report that decreasing laser repetition rate 320-fold from 80 MHz to 250 kHz allowed an increase in the number of cells imaged from 1 cell/125 mW to 17 cells/125 mW.[68]

The same principle holds in the case of continuous focal volume expansion. An increase of spot area by a factor of N leads to a decrease in fluence by the same factor, assuming fixed pulse energy. Fluorescence is proportional to the area excited, fluence squared, and an axial expansion factor that represents a combination of the axial depth of focus and the axial distribution of the fluorophores. For a horizontal membrane, there is no axial expansion, assuming that the focus is larger than the membrane thickness. For a Gaussian focus on a vertical membrane, the axial expansion factor is proportional to N, while the lateral area excited only grows by $\sqrt{N}$, since the membrane only extends on one lateral direction. Therefore, a horizontal membrane will experience a fluorescence scaling

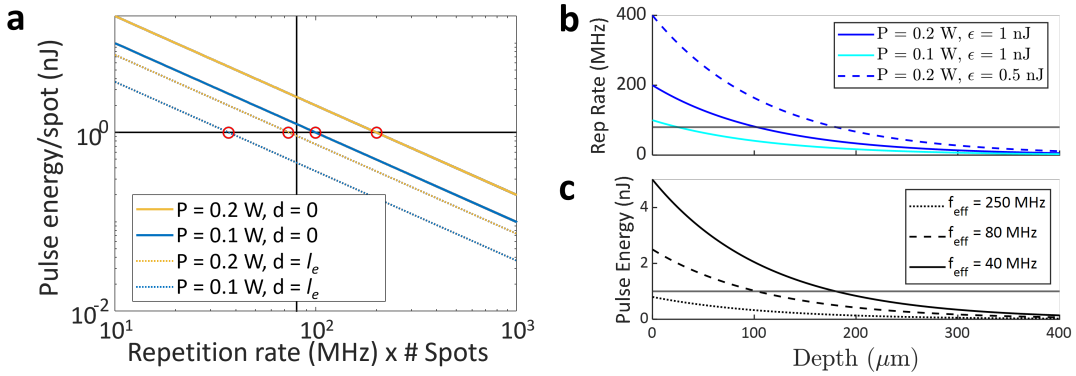

Figure 3.6: a) At fixed total power, per-spot pulse energy and effective repetition rate (rate x N_{spots}) are inversely proportional. Photophysics dictate that SNR can be increased by increasing pulse energy up to the threshold (1 nJ horizontal line shown). Therefore the optimal effective repetition rate can be found by finding the intersection of the iso-power line with the threshold (circled in red). At a non-zero depth (dotted lines), a lower repetition rate is needed to produce the same focal pulse energy. b) For a single spot, the optimal effective repetition rate crosses beneath 80 MHz (horizonal line) at ~100 μm depth for a total power of 200 mW and a pulse energy threshold of 1 nJ. Decreasing the threshold increases the optimal repetition rate at a given depth. c) For a fixed effective repetition rate, the focal pulse energy decays exponentially with depth. At a high rate of 250 MHz, a 1 nJ pulse is not achievable at any depth. For a low rate of 40 MHz, the pulse energy is above the threshold up to ~200 μm depth, beyond which the energy is sub-optimal.

of $\frac{1}{N}$, while a vertical membrane will experience a fluorescence scaling of $\frac{1}{\sqrt{N}}$ (Fig. 3.5b). A smaller focus on a cell membrane will therefore give more fluorescence for a fixed power budget and the number of cells measureable at a fixed SNR and power will scale with $N^{-1/2}$ to $N^{-1/4}$. Indeed, Sims et al. found that a whole-cell temporally-focused scanless system performed better with speckled illumination that approximated a point array than with more uniformly spread-out illumination.[68] Our model suggests that increasing spot area by a factor of ~100 to cover an entire cell would lead to a drop in N_{cells} of between 3 and 10, predicting fewer than 3-10 cells measureable with an 80 MHz laser with SNR of 10 at the brain surface. If the expanded spot only excites the 20% of the projected membrane area that is vertically oriented around the perimeter (see earlier estimates of φ), we would combine the 3x reduction in measurable cells for a vertical membrane with a φ factor of 0.2 to get a prediction of <2 measurable cells. This is consistent with the reported performance of a scanless system using a whole-cell spot.[68]

Trading repetition rate for pulse energy is only beneficial up to a certain maximum energy. Saturation of the 2P excitation typically occurs at pulse energies of ~1 nJ[99]. Furthermore, the peak intensity at the laser focus must not become too high or the sample may experience nonlinear photodamage.[128,129] For a fixed pulse width and spot size, this limit will be independent of f_{eff}. The optimal f_{eff} can therefore be found as the repetition rate at which pulse energy reaches but does not exceed this limit (Fig. 3.6a). Simultaneously approaching the 2P saturation energy (1 nJ) and the maximum power into the sample (~200 mW) implies a depth-dependent optimum laser repetition rate (Fig. 3.6b) of 1 – 10 MHz at depths of 5 l_e, where l_e is the exponential attenuation length.[99] Indeed a 2.5 MHz fiber-based soliton laser source was demonstrated to have 26-fold greater average signal than a matched 80 MHz Ti:Sa laser.[99] Effective repetition rate must be high enough to visit each measurement point at least once per measurement cycle. For example, an 800 kHz laser could visit 800 points at a 1 kHz revisit rate (assuming a suitable scanner existed) and would provide 100-fold higher time-average count-rate (and 10-fold higher shot noise-limited SNR) than the same laser

power delivered at 80 MHz, assuming a sub-saturation pulse energy.

Any system with a fixed value of f_{eff} will only perform optimally at one specific depth (Fig. 3.6c). Beyond the optimal depth, pulse energy will be decreased, while above that depth, power must be reduced to avoid exceeding the pulse energy limit. The f_{eff} of a system should therefore be tuned to the specific power limit, energy threshold, and depth required for a given experiment.

Optimizing the polarization

For membrane-localized chromophores, signal can be increased by aligning the excitation polarization with the transition dipole of the chromophore.[130] For 1P excitation, this effect scales as $\langle \cos^2 \theta \rangle$, where θ is the angle between the excitation polarization and the transition dipole, and the average is taken over the distribution of molecular orientations. The magnitude of the polarization-dependent effect is characterized by $(\Delta F/\bar{F})_{pol}$, where $\bar{F}$ is the fluorescence for unpolarized excitation and $\Delta F = F_{max} - \bar{F}$. At the cell periphery, where the optic axis lies in the plane of the membrane, this effect magnitude was $(\Delta F/\bar{F})_{pol}$ = 54% for the dye BeRST1, 20% for ASAP1, 13% for QuasAr3, 12% for ArcLight, and 4.5% for the FRET-opsin GEVI mNeon-Ace.[130]

For 2P excitation, polarization sensitivity scales as $\langle \cos^4 \theta \rangle$ [131] and can lead to large polarization-dependent changes in fluorescence signal from neurites with membrane-bound reporters.[132] Thus 2P voltage imaging systems could improve their power efficiency by ensuring linearly polarized excitation at the sample and selectively targeting cell membranes that have a favorable orientation relative to the laser polarization; or modulating polarization during a scan to match the orientation of the target membranes.

3.4.8 Can advanced analysis techniques overcome the shot noise limit?

Consider the goal of detecting whether a spike occurred (hypothesis $H^{(1)}$) or did not occur ($H^{(0)}$) during a measurement time τ. The mean number of detected photons in the case of a spike is n_1, and in the absence of a spike is n_0. The probability distributions for number of detected photons in the two cases are then given by Poisson distributions with means n_1 and n_0 respectively:

$$p\left(n\middle|H^{(1)}\right) = Poisson(n;\ n_1)$$

and

$$p\left(n\middle|H^{(0)}\right) = Poisson(n;\ n_0).$$

If the number of photons collected in either scenario is not large and the contrast $\beta = (n_1 - n_0)/n_0$ is also small, then the two probability distributions overlap: a given set of detected photons could have been produced by either the presence or absence of a spike. In such cases, no analysis algorithm can unambiguously determine whether a spike occurred; at best one can determine the relative probabilities of the two hypotheses. This argument is analyzed in detail in Ref. [108].

Voltage signals corresponding to spikes are typically correlated across multiple pixels, and sometimes across frames (depending on the frame rate and spike duration). Since the photon shot-noise is statistically independent between all pairs of pixels, the relative contribution of shot noise can be diminished by weighted averaging across pixels and possibly across frames. If the expected number of photon detections at pixel i is $\langle n_i \rangle$ and a filter assigns weight a_i to the pixel, then the expected signal is $S = \sum_i a_i \langle n_i \rangle$, and the variance in this quantity due to photon shot noise is $\sigma_S^2 = \sum_i a_i^2 \langle n_i \rangle$. The art in voltage imaging analysis comprises determining the a_i so as to maximize the difference between $p\left(S\middle|H^{(1)}\right)$ and $p\left(S\middle|H^{(0)}\right)$.

Determination of the weights a_i can be via simple manual or activity-based selections of regions of interest or via optimal detection algorithms, e.g. as in [41]. When signals from multiple sources overlap, a variety of unmixing algorithms are useful. [133–137] It is possible even to apply a filter during image acquisition to reduce the data burden. [138] Recently introduced machine learning algorithms [111,114] can help determine optimal weighting of pixel signals. None of these techniques overcomes the fundamental uncertainty resulting from the fact that different voltages can give identical photons arriving at the detector. Thus claims that these methods "overcome fundamental limits" [67] of shot noise are misleading.

3.5 Discussion

Eq. 3.2 places severe constraints on the number of cells that will be measurable at d > 300 μm with 2P voltage imaging, even with substantial improvements in GEVI brightness and voltage sensitivity (Fig. 3.3c). These findings indicate that 2P imaging of hundreds of neurons with high SNR at depth > 300 μm will require an order-of-magnitude improvement in 2P GEVIs or qualitatively new approaches to imaging. Given the current state of the art, one can maximize SNR and number of measurable cells at depth by using excitation with high numerical aperture, low repetition rate (1 – 10 MHz), short pulses (< 100 fs), and membrane-targeted illumination with real-time compensation for tissue motion. Optimal imaging can be achieved by customizing spatial multiplexing, temporal repetition rate, and/or excitation NA for the target imaging depth and power limit. Experiments that allow for intermittent imaging and/or distribute the measurements sparely in space can allow for peak illumination power, up to the limits set by fluorophore saturation and/or nonlinear photodamage.

Voltage imaging *in vivo* places stringent demands on the molecular, optical, and data analysis tools. We hope that a comprehensive understanding of these constraints will both shape realistic

expectations and guide efforts towards enhancing the performance of 2P voltage imaging.

———–

3.6 Manuscript Information

3.6.1 Previously published as

A version of this chapter appeared in[95]:

Davis, H. C., Brooks, F. P., Wong-Campos, J. D., Cohen, A. E. Optical constraints on two-photon voltage imaging. 2023.11.18.567441 Preprint at https://doi.org/10.1101/2023.11.18.567441 (2023).

3.6.2 Acknowledgements

We thank Andrew Preecha and Shahinoor Begum for technical assistance, and Simon Kheifets and Vicente Parot for helpful discussions. This work was supported by NIH grant R01-NS126043.

3.6.3 Data availability

Data are publicly available on the DANDI archive.

- Scaling of GEVI fluorescence with 1P and 2P illumination intensity: https://dandiarchive.org/dandiset/000537.
- 1P and 2P contrast of JEDI-2P and Voltron2$_{525}$: https://dandiarchive.org/dandiset/000538.

Data on the depth-dependence of fluorescence are in process of deposition.

3.6.4 Code availability

The instrument control code is available at www.luminosmicroscopy.com and https://github.com/adamcohenlab/luminos-microscopy/.

3.6.5 The author's contributions

Hunter Davis, Frederick Brooks, and Adam E. Cohen designed the study and experiments. Hunter Davis collected all of the data. J. David Wong-Campos performed all mouse surgery and preparation for imaging and assisted with *in vivo* data collection. Hunter Davis, and Frederick Brooks performed all analyses. Hunter Davis and Adam E. Cohen wrote an initial draft of the manuscript with input from all authors. Frederick Brooks and Adam E. Cohen significantly rewrote the entire manuscript, substantially expanding and clarifying all sections and adding in-depth discussions of reporter kinetics (Fig. 3.4), spatiotemporal splitting (Fig. 3.6), and advanced analysis techniques. Adam E. Cohen supervised the work.

4

Luminos: Open-source software for modular bi-directional microscopy

4.1 Introduction

The emerging field of all-optical electrophysiology provides powerful methods for interrogating neural organization and processing (e.g., [105]), but these techniques are currently only accessible to

a small number of researchers. The unique photophysical demands of optical electrophysiology[95] require degrees of speed, synchronization, and multi-dimensional control that are difficult to achieve using readily-available control software. For instance, a single digital micromirror device (DMD) may be used to independently pattern blue stimulation and orange imaging light by synchronizing acousto-optical tunable filter (AOTF) control waveforms with a pattern-switching DMD trigger (Fig. 4.1a). At the same time, analog control and feedback of light intensity, galvanometric scanners, and/or a patch-clamp amplifier may be required. All this must be performed while imaging at a 1 kHz frame rate, with stimulus and signal jitter of < 0.1% between frames.

The well-known μManager open-source modular microscope control package[139] is built around the demands of lower-speed loosely-synchronous acquisitions for which sequential real-time commands provide acceptable control synchronization. This model of sequential script-based experiment control is limited by unpredictable delays introduced by operating systems and packet-based communications and cannot produce consistent timing below tens of milliseconds.[140] While camera-frame-level synchronization can be achieved using an external hardware sequencing device, arbitrary sub-frame high-speed synchronization is not achievable without significant custom hardware or software development work.

ScanImage[59] is another popular microscope control package and can provide synchronization superior to μManager. It does not currently implement camera-based video acquisition, however, which prevents its use for most voltage imaging experiments. Our lab, and others in the emerging field, have therefore relied heavily on custom control software, which is difficult to maintain within a lab and nearly impossible to share in a useful way.

To make optical electrophysiology more generally accessible, we present Luminos, an open-source library for highly synchronized microscope control. While motivated by the demands of optical elecrophysiology, this library is general and is intended to be used for a wide range of experiments. In Table 4.1, we compare Luminos with existing microscope control solutions.

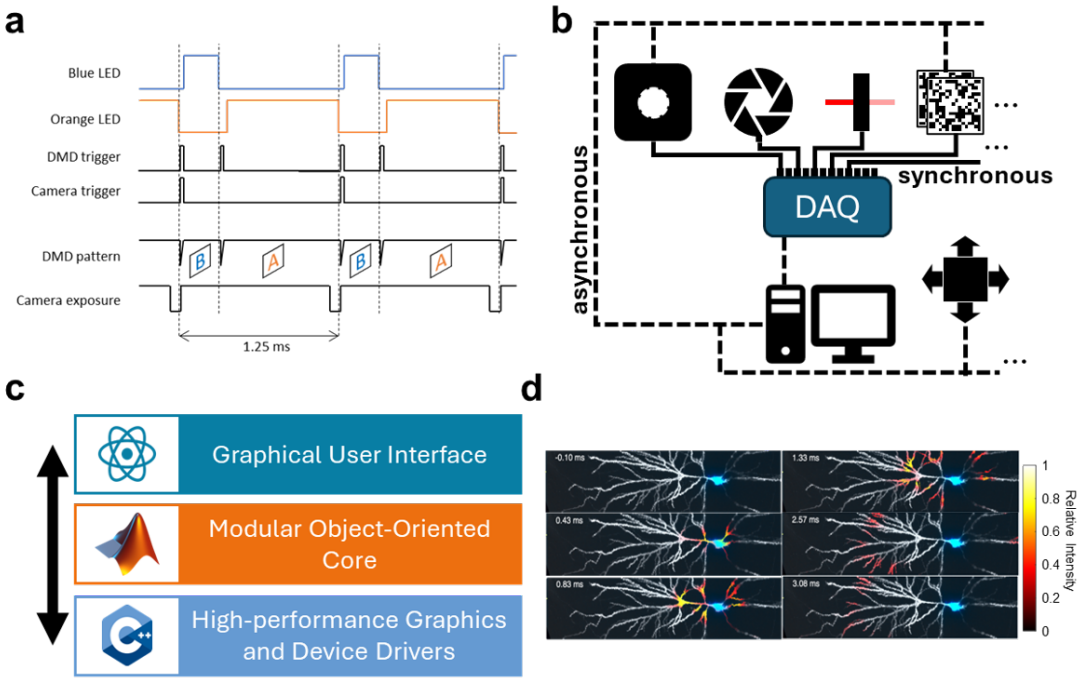

Figure 4.1: a) Example of highly-synchronized acquisition protocol involving alternating blue stimulus and orange imaging light patterned off of the same DMD, with pattern switching controlled by a trigger input to the DMD. Camera frames are synchronized by a trigger input to the camera. b) Functional diagram of Luminos control connectivity. The DAQ is the center of the system, exerting tight synchronous control of cameras, shutters, modulators, patterning devices, and other devices. The PC uses asynchronous loosely-timed communication to set up the DAQ and to control a partially overlapping set of devices. Some devices will have no direct connection to the PC, while others (such as motion controllers) may have no provision for synchronous communication and are necessarily controlled by the PC. c) Code-level hierarchy of Luminos. Information flows between low-level optimized drivers written in C++, the modular object-oriented configurable core written in MATLAB, and the top-level user interface written in ReactJS. MATLAB and the MATLAB logo are trademarks of Math Works. The C++ logo is a trademark of the Standard C++ Foundation. d) Examples of an analysis showing electric signal propagation through a neuronal dendritic arbor after targeted somatic optogenetic stimulation. Data acquired using Luminos. Figure adapted from[45].

Table 4.1: Comparison of Luminos and existing control solutions.

Name	Supports high-speed camera acquisition?	Timing CPU limited?	Hardware agnostic?	Source availability	Customization language
μManager [139]	Yes	Yes	Yes	Open source	Various
ScanImage [59]	No	No	Yes	Proprietary (Limited Open Source)	MATLAB
Scope [141]	No	No	Yes	Open Source	C++
Various Proprietary	Various	Various	No	Proprietary	Various/None
Luminos	**Yes**	**No**	**Yes**	**Open source**	**MATLAB**

4.2 Main Text

Luminos is based on the capabilities of a buffered Data AcQuisition system (DAQ). In fact, we find it useful to view the DAQ as the center of the control system, with the PC used only to set up the acquisition, stream the resulting data, and record the metadata (Fig. 4.1b). This is a paradigm shift from other open-source control packages like μManager, which view the PC as the center of the control system and are therefore limited by the latency and jitter of the PC's operating system (OS). Using the capabilities of National Instruments Data Acquisition devices (NI-DAQs), analog and digital control waveforms are pre-defined and loaded onto the NI-DAQ. Similarly, DMD control pattern sequences are pre-calculated and loaded onto the DMD local memory. The camera(s) is also pre-configured such that its acquisition is dependent only on the DAQ. Initiation of an experiment consists of starting the pre-loaded DAQ waveforms, handling any resulting data streams, and saving metadata once the DAQ has finished. Device synchronization is limited only by internal device response to digital/analog controls.

Luminos consists of three software layers (Fig. 4.1c). The center layer, at which most customization will be performed, is a modular MATLAB core with classes representing each device type and

acquisition scripts to set up and terminate each type of experiment. Experiments can in fact be run entirely from the MATLAB command line. This layer also handles referencing of all patterning and imaging devices to a common set of spatial coordinates. While open-source languages like Python are growing in popularity, we find that the combination of computational power, ease of use, and standardization of MATLAB is attractive. A compiled C++ driver layer supports performance-critical components like high-speed camera streaming, live video display, and DAQ configuration. At the top layer, a customizable user interface (UI) written in JavaScript with React provides an intuitive interface. Separate tabs for different device classes along with the ability to save and load custom configurations facilitate rapid implementation of complex protocols. Once the software is configured for a given microscope, most experiments will be performed entirely from this top-level interface.

In addition to a powerful control implementation, Luminos provides consistent logging of data and metadata. Upon completion of each acquisition, Luminos logs the complete state of the virtual microscope in a highly predictable MATLAB .mat file. The user does not have to decide which relevant metadata to record, and experiment data from different custom microscopes can be analyzed using the same code. The user can also record notes in a virtual notebook provided on the UI.

Luminos has been used in our lab and by collaborators for a wide range of experiments. We have performed simultaneous targeted optogenetic stimulation and high-speed voltage imaging of neuronal dendrites, using Luminos' DMD patterning abilities to target blue stimulus to the soma while imaging the entire cell (Fig. 4.1d).[45] In another experiment, simultaneous dual-plane patterned illumination combined with blue channelrhodopsin stimulus allowed simultaneous perturbation and monitoring of somatic and dendritic membrane potential dynamics in awake mice[46]. We have made an adapter for the ViRMEn virtual reality (VR) engine[142] to allow optical electrophysiology experiments in a VR environment. We hope that making this library broadly available will make these sorts of experiments accessible to many more scientists.

In the Implementation section we provide details of Luminos architecture and data flow, a list of currently supported hardware, and tutorials describing basic setup and use of the software. The source code and documentation for Luminos can be found at https://github.com/adamcohenlab/luminos-microscopy and https://www.luminosmicroscopy.com.

4.3 Implementation

4.3.1 Details of Luminos code architecture

Luminos' core functionality is implemented in modular object-oriented code in both Matlab and C++. On top of these functional core layers, a ReactJS layer provides a tab-based intuitive web interface.

The top-level unit of function of Luminos is an instance of a `Rig_Control_App` object. The `Rig_Control_App` superclass manages device initialization, JavaScript communication, experiment coordination, and metadata saving. Distinct subclasses of the `Rig_Control_App` are made for each microscope, and multiple subclasses (virtual microscopes) can share overlapping sets of hardware. Microscope-specific subclasses may, but need not, implement additional functionality.

Individual hardware devices or virtual devices (e.g., a single analog output from the DAQ) are represented by instances of the abstract `Device` superclass. We implement a multilevel class hierarchy so that, for example, functionality common to all types of patterning devices (calibration, ROI selection, etc.) is specified in a mid-level abstract `Patterning_Device` superclass, with the particular implementations given in device-specific subclasses. This allows for device-agnostic modular code so that, for example, a DMD patterning tab can be implemented without knowing which specific DMD device will be used.

Each device class consists of properties that will automatically be part of the archived metadata after an acquisition, transient properties that will not be saved, and methods that implement the rel-

evant device functionality. Device class instances are independent of the `Rig_Control_App` that loads them and of other devices. Device instances may be loaded without loading the app using the `Standalone_Device()` utility. This ensures that devices may be loaded in any order and maintains control over inter-device communications at the app level for more transparent and robust code.

Performance-critical device implementation that benefits from thread parallelization or lower-level device access is implemented in modular C++ code. We currently implement camera and live video streaming, DAQ communications, galvanometric scanners, and ALP DMDs at this level. Again, we make use of hierarchical class inheritance to specify a common interface in a high-level class while providing the device-specific implementation in a subclass. The high-level `Cam_Wrapper` class is currently subclassed by `Hamamatsu_Cam`, `Andor_Cam`, and `Kinetix_Cam`. We split the compiled code into two functional parts. The custom device drivers are compiled to C++ object files, which allows testing via compiled C++ testbenches. An adapter layer implements the MATLAB interface and is compiled into mex files which provide a library interface to MATLAB. This separation of the interface from the driver implementation would allow straightforward use of these drivers with a different high-level language, for instance Python, simply by writing a different adapter layer. For cross-hardware compatiblity, we do not implement any GPU-based computation, but we do implement optional optimized vectorized instructions for parallel computation using SSE 4.1 vector intrinsics on CPUs that support this (Intel after Penryn 2007/8; AMD after Bulldozer 2011).

The ReactJS user interface is based on the tab as the fundamental unit and communicates with Matlab via a local Node.JS server. A tab communicates with a set of devices, implements user device control and inter-device coordination, and may contain subpanels for specific sub-functionality. A tab may also communicate with components of other tabs. All apps will have a main tab (Fig. 4.2), which contains several subpanels, and a waveform tab (Fig. 4.3). Other tabs are optional, and

custom tabs can be created using the ReactJS framework.

The main tab (Fig. 4.2) contains a text entry field for naming each acquisition. Below is a panel that provides real-time control over all digital shutters, analog modulators, and filter wheels. For systems with a computerized stage connected, a stage controller panel provides control and readout of current stage position. A notes panel saves notes into an associated text file in real time. On the right, a button calls the associated acquisition script, and below that, the camera panel allows configuration of the camera, with a plot displaying a real-time plot of average intensity in a user-selected region of interest. When multiple cameras are present, the camera control panel will also be tabbed, with a tab for each camera. The advanced frame triggering mode dropdown allows configuration of the camera to synchronize each frame to a trigger pulse provided by the DAQ. The app exit button is present on all tabs and allows clean exit from the app. If configured, the app will automatically copy all data from that session to a pre-specified remote server directory that is independently configured for each user.

The waveform tab (Fig. 4.3) allows configuration of the buffered waveform that will be loaded onto and run from the DAQ. The plot at the top provides a preview of the waveform. The global properties panel allows setting of overall waveform duration, DAQ clocking rate (which must match the external clock rate if not using the internal DAQ clock), the clock connector, the trigger connector, and the triggering mode. Self-trigger mode allows the DAQ to start upon software command, sending a trigger pulse out on the trigger connector, while external-trigger mode instructs the DAQ to begin acquisition when it receives a pulse on the trigger connector. These triggering capabilities may be used to synchronize a Luminos-based system with a separate hardware or software acquisition sequencer or microscope. A single waveform is made up of one or more analog outputs, digital outputs, and analog inputs. A set of pre-defined waveform function files provide an expansible repertoire of basic waveform types that can be customized with several parameters each. Full waveform configurations can be saved and loaded with buttons at the top right, and a waveform-only

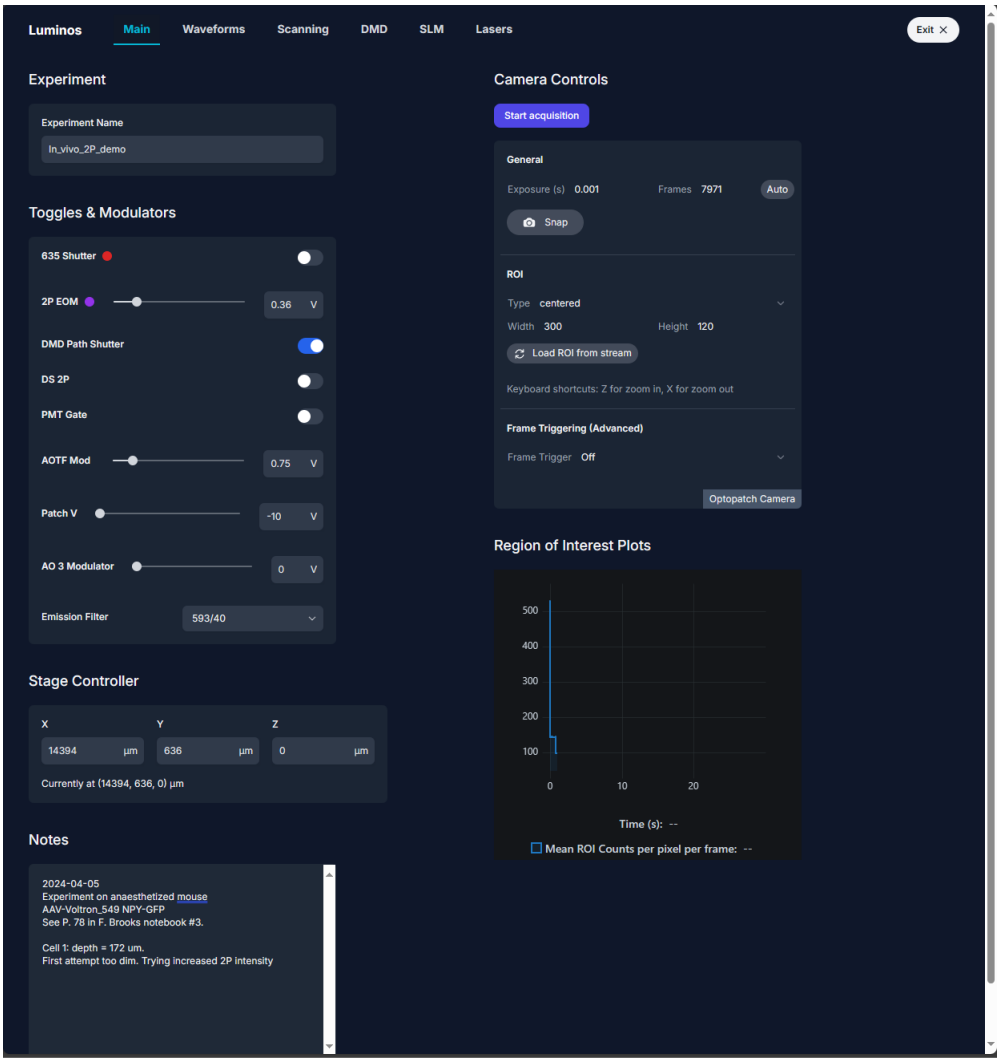

Figure 4.2: The main tab provides overall experiment control, with experiment naming, on-demand control of analog modulators, digital shutters, filter wheels, and motion control, and control of the camera. A live-updated plot shows a trace of the brightness in a user-selected region of interest from the live camera stream. A notes panel automatically saves any notes that the user adds. The tab bar at the top allows navigation to the other tabs.

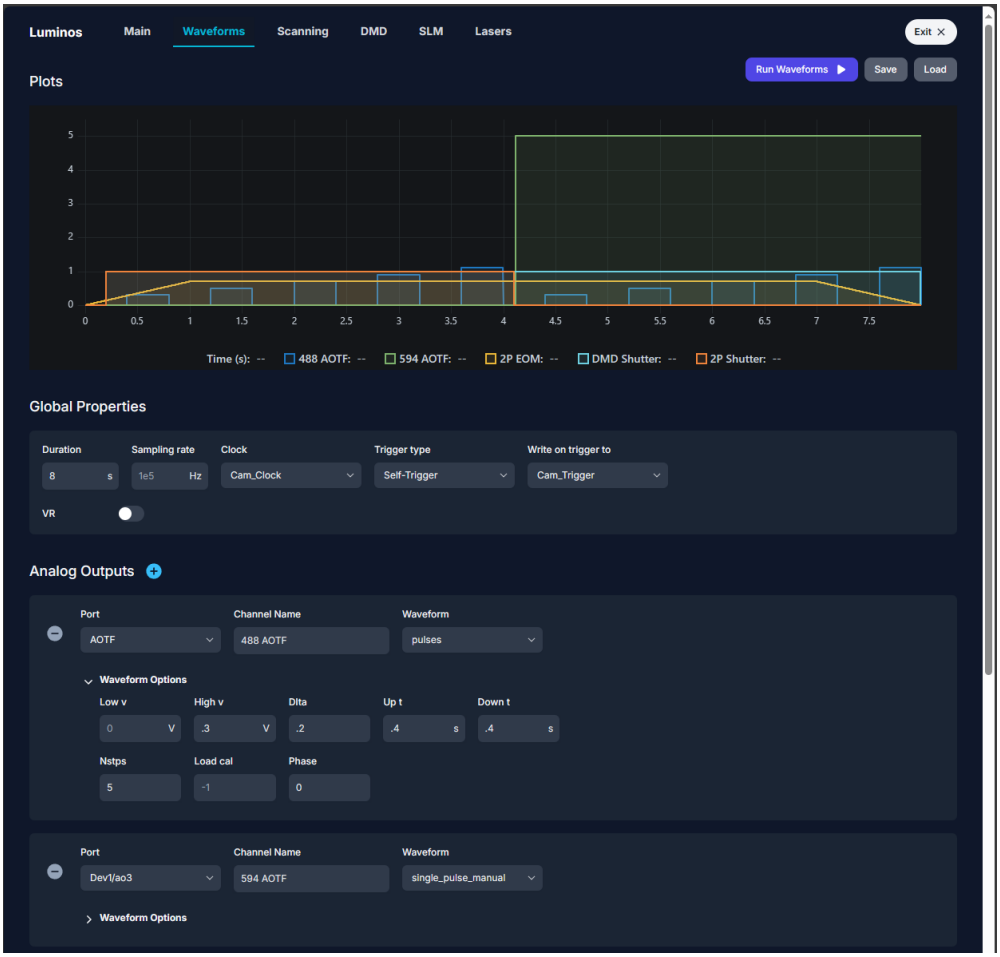

Figure 4.3: The waveform tab provides specification of custom buffered waveforms with the ability to save and load configurations. Clocking and triggering options provide essential control over timing, and the plot gives a preview of the waveform. The dropdown interface provides a large amount of control without clutter. When an external clock is used, the sampling rate must be set to match the external clock rate.

acquisition without video can be started with another button.

All patterning tabs (Fig. 4.4) allow loading and display of a reference image, a calibration button, and ROI selection tools. The specific ROI types available and any added functionality depend on the specific type of patterning device. The DMD tab allows creation of polygonal, circular, and freeform ROIs. Multiple ROIs can be combined, as in the case of targeting circular spots to neural soma shown here.

While the ReactJS user interface is the most intuitive way to configure an experiment, the full app functionality is present in the MATLAB layer. Devices and experiments can therefore be directly configured from MATLAB using scripts or the command line (Fig. 4.5). This allows more complex experiments to be configured. In fact, final configuration and intiation of all acquisitions is performed by experimental scripts that are triggered by the user interface acquisition buttons. These scripts set up the data directory, set up any necessary advanced timing, configure the master device that will define the end of an experiment, and send software triggers to the DAQ and camera. We provide seven example acquisition scripts, but arbitrarily complex acquisitions can be defined.

4.3.2 Details of Luminos information flow

There are two flows of information controlled by Luminos, asynchronous device configuration and synchronous device control (Fig. 4.1b).

The flow of asynchronous device configuration information begins with the rig initializer files. Each microscope app has a corresponding rig initializer file in JSON format. Upon initialization, the `Rig_Control_App` instance loads this initializer and initializes each device with the corresponding properties given in the file. This allows initialization of the microscope into a consistent predefined state. After initialization, asynchronous commands can be sent either from the user interface or from MATLAB to update device configurations. At the end of acquisition, devices that have been flagged for monitoring using the `Rig_Control_App.assignDevicesForMonitoring()`

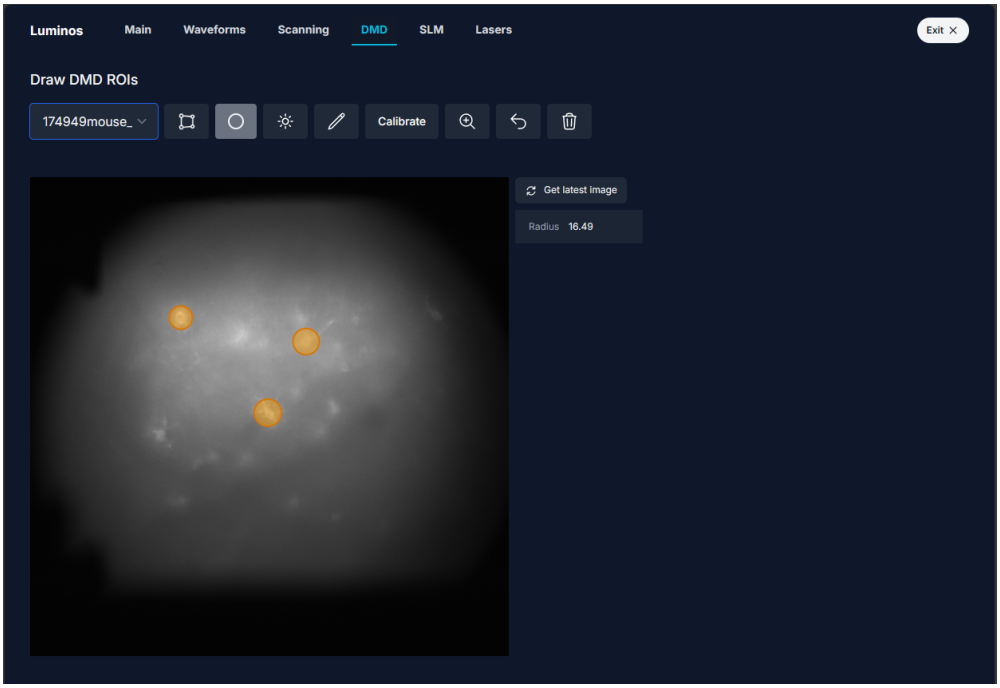

Figure 4.4: The patterning tab (a DMD tab in this case) provides various tools for drawing target regions of interest. First, an affine semi-automated calibration is performed using the "Calibrate" button. The user can then load a reference image using the dropdown selector, and can draw arbitrary polygons, circles, or curves (three circles over neural soma in this case. Image taken during data collection for chapter 2 [103]). The pattern is uploaded to the DMD automatically. The DMD tab does not currently provide the ability to load multiple patterns into a pattern stack in DMD memory, but this capability is present in the MATLAB code and may be easily scripted into an experimental protocol.

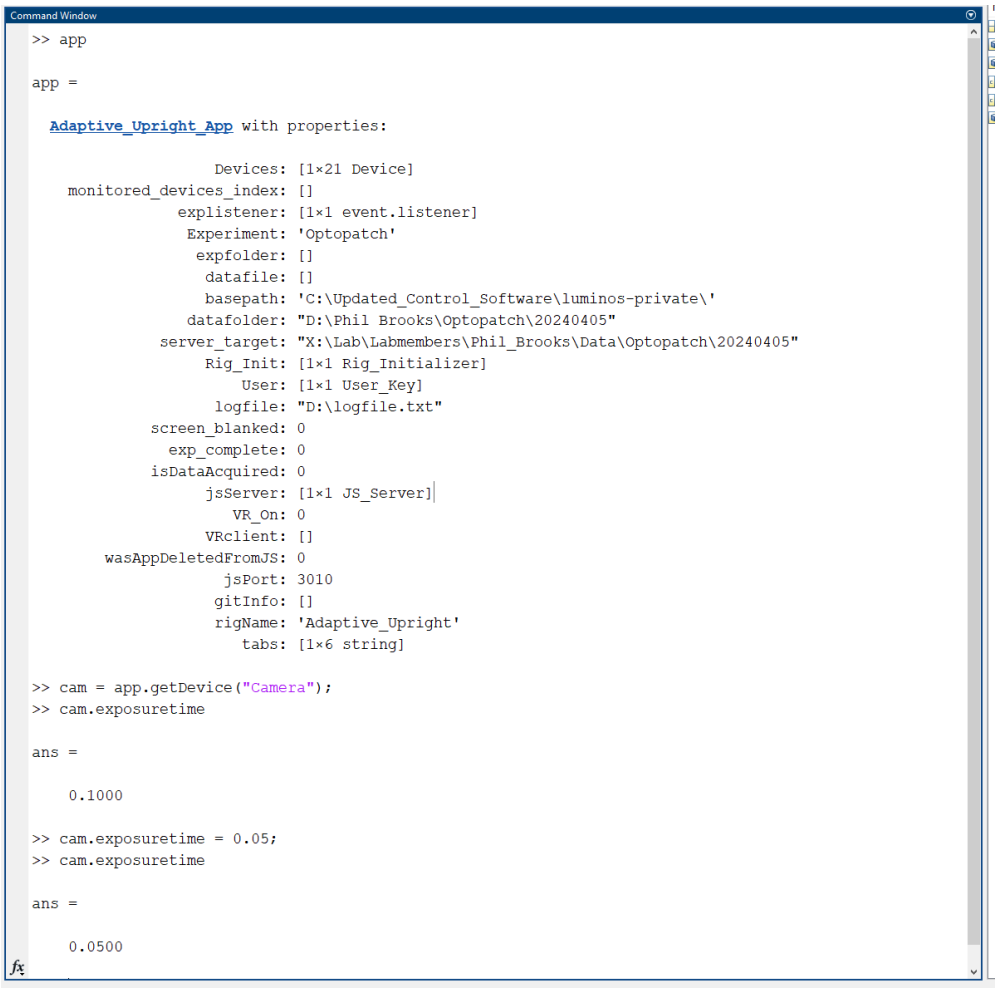

Figure 4.5: While the JavaScript UI offers powerful control, the entire control app exists as an object in the MATLAB workspace and can be interrogated and controlled directly from MATLAB either through scripting or through live commands. Here, we display a summary of the app state. We extract the camera device, query the current exposure time, change the exposure time, and then check that this change was effective. The updated exposure time will be reflected in the UI camera panel as well.

method will have all of their non-transient properties saved into the `outputdata.mat` metadata file for use in analysis. Patterning device calibrations are also separately saved in MATLAB .mat files, which are updated upon calibration. This allows calibration to be maintained between imaging sessions. Asynchronous device communication is implemented in a device-specific manner. Many devices implement ASCII serial command sets, while others come with driver libraries.

The flow of synchronous device control information begins on the waveform tab, where custom waveforms are defined. These waveforms can be saved and loaded for reuse. Before acquisition, the waveform is built and loaded into the DAQ buffer. Upon triggering, the DAQ begins synchronous buffered operation of all defined outputs and inputs until the predefined acquisition time is complete. Upon completion, the input and output buffers are saved with corresponding metadata into the outputdata.mat file. DAQ operation can be clocked either internally or externally. For highly synchronous camera acquisition, it is often necessary that the camera and DAQ share the same clock. Many modern scientific cameras, including Hamamatsu Flash and Fusion and Andor iXon cameras, provide a clock output that can be used to clock the DAQ. Similarly, for two-photon scanning systems, it is possible to clock the DAQ from the pulsed laser. It is generally not possible to ensure a shared clock for more than one device that does not have a clock input. All synchronous control is implemented as analog and digital input-output links between the DAQ and the hardware devices.

4.3.3 Configuring and using RAM-drive mode in Luminos

Modern NVMe SSD drives and/or RAIDed SSD arrays can support sufficient data throughput to record at high speed directly onto disk. Systems with slower storage must stream into RAM instead. Assuming sufficient RAM is installed to store a full acqusition while still leaving sufficient RAM for program execution, Luminos can be configured to stream high-speed video directly to RAM, copying the result over to the Data disk directory after the acquisition finishes. To do this, first in-

stall ImDisk Toolkit (https://sourceforge.net/projects/imdisk-toolkit/) and create a RAMdisk of the necessary capacity with drive letter R:. Then set the "rdrivemode" parameter to 1 in the camera device entry of the app initializer (see tutorial on initializers below). Acquisition will now not be limited by storage speed. We do not enable this by default because the added transfer step can cause slightly more frequent acquisition bugs, so we recommend fast disk storage systems in general.

4.3.4 Tutorial 1: Initial setup instructions

1. Install prerequisites
    (a) Windows 10/11
    (b) MATLAB r2021a or later (tested up to r2024a) with the following toolboxes
        i. Data Acquisition Toolbox
        ii. Image Processing Toolbox
        iii. Instrument Control Toolbox
        iv. Optimization Toolbox
        v. Statistics and Machine Learning Toolbox
    (c) Install the Data Acquisition Toolbox Support Package for National Instruments NI-DAQmx Devices from the MATLAB Add-Ons Manager.
    (d) `Node.js` (https://nodejs.org/en/download/). Default Options
    (e) Visual Studio Community (visualstudio.microsoft.com) Desktop C++ development.
2. Clone the Luminos repository by running this line in your terminal

```
> git clone https://github.com/adamcohenlab/luminos-microscopy.git
```

3. Build the libraries by running the following command in MATLAB from the Luminos directory

```
> build
```

4. Plug in your NI DAQ or set up a DAQ simulator (https://knowledge.ni.com/KnowledgeArticleDetails?id=kA03q000000x0PxCAI&l=en-US) and note the name (You can use NIMAX to view this easily). e.g., "Dev1"

5. Edit the initializer file

   (a) Open `Simulator.json` (type "`edit Simulator.json`" in MATLAB) and replace all instances of "Dev1" with the name of your DAQ

6. Run the app in MATLAB with the following command

```
> app = Simulator_App()
```

7. You should now see a simulated camera with diagonal stripes along with a browser-based simulator UI. Follow the next tutorial to configure Luminos for your specific hardware.

4.3.5 Tutorial 2: Customizing and initializer for your hardware

1. You will be modifying the `Example_App.m` and `Example.json` files for this. You can later rename the files and appropriate names in the files to any app name you'd like.

2. Open `/src/Applications/Example/Example.json` in a text editor

3. First, edit the "`dataDirectory`" field to a directory where you'd like Luminos to save your data. Luminos will create timestamped subfolders here for each experimental session.

4. Now edit the "tabs" list with one entry for each tab you want. You'll need at least "Main" and "Waveforms". Other options are "DMD", "SLM", "Scanning", "Lasers", "Hadamard", "SpinningDisk". (/src/User_Interface/frontend/src/tabs for a full list). Order does not matter.

5. Now, set up the "DAQ" and "Camera" device entries with the appropriate parameters.

6. Add any other device entries you need, following the examples given in Example.json. The required parameters for each device can be found in the corresponding initalizer. For instance, if you want to know the parameters you should specify for given deviceType, inspect the file called <deviceType>_Initializer.m and look at the properties the initializer expects. A list of supported devices in given in Supplementary Table 1.

7. Add required device drivers.

   (a) Since we can't distribute proprietary device drivers with our code, you'll have to install them yourself for any devices that require them (e.g. cameras).

   (b) For Hamamatsu cameras, download both DCAM-SDK and DCIMG-SDK (https://dcam-api.com/sdk-download/). You'll need to create a free account. Unzip both SDKs into /src/lib/Luminos_VS/inc/. You should have the following folders:

      i. /src/lib/Luminos_VS/inc/dcamsdk4

      ii. /src/lib/Luminos_VS/inc/dcimgsdk

   (c) For Andor cameras, download the appropriate Andor SDK (https://andor.oxinst.com/downloads/) and unzip into /src/lib/Luminos_VS/inc.

   (d) After adding all drivers, recompile the C++ code by running the "build" command in MATLAB.

Table 4.2: Currently supported hardware.

Software Requirements	
	Windows 10/11 with MATLAB r2021a or later
Camera	
	Hamamatsu (tested on Flash, Fusion) Andor (tested on iXon)
DAQ	
	National Instruments (tested on USB, PCIe)
DMD	
	ALP 4.1, 4.2, 4.3 TI DLP
SLM	
	Meadlowlark
Scanner	
	Any analog galvanometric scanner
Filter Wheel	
	Thorlabs Optec high speed filter wheel ASI FW1000
Shutter	
	Any analog or digital-controlled shutter
Modulator	
	Gooch & Housego 8-channel AOTF controller Any analog-controlled modulator Thorlabs motorized rotation mount with half-wave plate
Motion Control	
	Sutter MPC200 Scientifica SliceScope Ludl MAC5000/6000 Thorlabs TCube
Power Meter	
	Thorlabs PM400 Newport 84x_PE
Laser (software control optional)	
	OBIS Hubner SpectraPhysics DeepSee
Spinning Disk	
	Andor/Yokogawa
Optical Trap	
	Any analog galvo-based trap
Optical Parametric Amplifier	
	Amplitude Systems Mango
Other	
	Any device compatible with DAQ I/O

8. Test each device

    (a) After adding each device, test by running in standalone device mode. For example, the camera would be tested with:

        i. `cam = Standalone_Device("Example","Camera");`

9. Run the full app

    (a) After adding and testing devices separately, run the full app with:

        i. `app = Example_App();`

10. View the data

    (a) After an acquisition, you should see in your data directory a datestamped subfolder with a timestampled subfolder for each acquisition.

    (b) Within an acquisition folder you should see two files. The video is in `frames1.bin`, and the metadata in `output_data.mat`.

    (c) From MATLAB, you can load the results by running the following command:

        i. `[mov, avgImg, DeviceData] =`
        `Extract_Mov("path/to/data_directory");`

4.4 Manuscript Information

4.4.1 Acknowledgements

We thank Vicente Parot for helpful advice and frameworks for low-level camera drivers. We thank all members of the Adam Cohen lab for continual feedback, code contributions, and testing of this software.

4.4.2 The author's contributions

Hunter Davis led the software development team until June of 2023. Hunter Davis and Frederick Brooks designed and led implementation of the software. Frederick Brooks led the software development team from June of 2023, supervised the public code release, and wrote the manuscript. Raphael Hotter implemented the ReactJS user interface and organized the code repository for public release. Marley Xiong implemented the optional virtual reality interface. Hunter Davis, Frederick Brooks, Raphael Hotter, Daniel Itkis, David Wong-Campos, Rebecca Frank Hayward, Bill Jia, Marley Xiong, Madeleine Howell, Byung Hun Lee, and Adam E. Cohen contributed code to this project. Adam E. Cohen supervised the work.

5

Absolute voltage from dual fluorescent reporters: Theory and experiment

5.1 Introduction

Transmembrane potentials play important roles in neuronal computation, muscle activation, cell metabolism, and organism development, [1,4,5,143,144] but historically these potentials have been dif-

ficult to measure. Recent progress in genetically encoded voltage indicators[38,44,83,117,145] (GEVIs) has made it possible to map bioelectrical dynamics in cultured cells[20,24,146], intact tissues[68,78,80], and live animals[2,16–18,22,67,70,77,84,105,147]. Yet voltage imaging from GEVIs and conceptually similar voltage-sensitive dyes has traditionally yielded only relative, rather than absolute, voltage levels.

Two important classes of experiment remain out of reach of relative intensity-based voltage imaging. First are experiments in which absolute voltage levels are compared among cells or subcellular locations. Both reporter expression and fluorescence background can vary over space, leading to position-dependent (and *a priori* unknown) offset and scaling of the relation between fluorescence and voltage. Second are experiments in which slow voltage dynamics are tracked, e.g., during development, during disease progression, or during behavioral state changes in the brain. At these timescales, the dynamics of protein expression and trafficking become relevant, and cell membranes can move or change density. These dynamics, too, lead to a time-dependent and (*a priori* unknown) offset and scaling of the relation between fluorescence and voltage.

Several methods for absolute voltage imaging have been demonstrated or proposed[148], but these approaches have limitations on speed, sensitivity, or accessibility that prevented their broad adoption. These methods include fluorescence lifetime measurements[60,149,150], measurements of photocycle dynamics[94], two (or more) point drug-induced calibration[151], and ratiometric readout[152,153]. Ratiometric calibrations are confounded by differential photobleaching, uneven illumination intensity and varying background and therefore change significantly over time and from cell to cell.[154–156] Drug-induced calibration, while potentially useful *in vitro*, requires a level of biological perturbation not compatible with *in vivo* work. Measurements of photocycle dynamics require a complex and slow readout and have not been used after their initial publication. Fluorescence lifetime imaging (FLIM) perhaps has the most inherent potential for improvement if current limitations in detection speed could be overcome, but to date, lifetime imaging of absolute voltage has only been demonstrated with a sensitivity of ≥ 10 mV in a 1 s acquisition window, insufficient for

sampling many interesting biological systems. In addition, unlike intensity readout, FLIM requires an expensive pulsed laser source, limiting its broader accessibility. A technique for kilohertz-rate lifetime voltage imaging was recently demonstrated,[157] but was unable to provide absolute calibration due to mixing of the sensor lifetime signal with photobleaching background fluorescence.

Here we discuss the mathematical properties and shortcomings of single-indicator intensity-based voltage imaging. We then analyze experimentally and theoretically the possibility of absolute voltage imaging via two indicators with different slopes to their F vs. V curves. Finally, we analyze prospects for absolute voltage imaging with one linear-response GEVI and a second nonlinear GEVI.

5.2 Results

5.2.1 Relation between fluorescence and absolute voltage

Most voltage imaging relies on readout of fluorescence intensity from reporters in the cell membrane. Every such recording encounters two sources of uncertainty. First, there is an unknown background from out-of-focus sources, light scatter, and in-focus but not voltage-responsive fluorophores; and second there is uncertainty in the overall density of reporters in the membrane. This situation can be expressed as

$$F = ag(V) + b \tag{5.1}$$

where the overall fluorescence of a point, F, is related to the single reporter response curve $g(V)$ by the unknown scaling and offset a and b. High-resolution imaging, image processing, and optical sectioning techniques (e.g., confocal, light-sheet, or two-photon microscopy) can partially reduce or correct for the unknown offset to the extent to which it is not perfectly co-localized with

the reporter. The unknown scaling factor, a function of variable reporter expression, folding, and trafficking and of illumination and imaging conditions, remains unknown, preventing absolute voltage readout. Consider an indicator, such as Voltron1 [43,44] or the Arch-based GEVIs [117], whose response is approximately linear over the biologically relevant range -100 to +50 mV. We can express the molecular response curve of the pure GEVI as

$$g(V) = c(V - V^0) \tag{5.2}$$

with V^0 a biophysical constant representing the voltage at which the fluorescence extrapolated from the linear regime would reach zero. The fluorescence is:

$$F = a(V - V^0) + b. \tag{5.3}$$

The unknown scaling coefficient, a, includes the effect of the molecular scaling coefficient, c. As a and b are varied, we obtain a family of possible relations between F and V, among which it is not possible to determine the correct one without external information.

To convert raw fluorescence to a more useful measure, it is common to choose a baseline condition, e.g., when the sample is in a resting state, with fluorescence $F_{baseline}$. Assuming constant a and b, subtracting $F_{baseline}$ from each fluorescence measurement yields $\Delta F = a(V - V_{baseline})$ that is insensitive to background. Typically, this measure is then normalized by dividing by $F_{baseline}$, producing a measure:

$$\frac{\Delta F}{F} = \frac{a(V - V_{baseline})}{a(V_{baseline} - V^0) + b} \tag{5.4}$$

If the background has been removed from $F_{baseline}$, either by optical sectioning or by post acquisition image processing, then this simplifies to $\frac{\Delta F}{F} = \frac{(V - V_{baseline})}{(V_{baseline} - V^0)}$, a measure that is insensitive to the

unknown scaling factor. It is commonly assumed that $\frac{\Delta F}{F}$ of a given reporter has a fixed relationship to voltage across experiments, but this is generally not true. $V_{baseline}$ may vary from experiment to experiment, a and b may change over the course of an experiment, and the success of background removal will also vary. We urge caution in any analysis in which even relative amplitudes, rather than just temporal characteristics, are analyzed.

5.2.2 Calibration by readout from correlated indicators

Here we describe a novel and accessible approach to absolute voltage imaging. Rather than attempting independent readout at every timepoint as existing methods do, we treat the fluorescence traces from dual co-expressed indicators as a system of simultaneous equations that can be solved to give the absolute voltage at each time. We first explore the linear case and show that this does not result in a unique solution when b is non-negligible. We then describe a novel method by which the combined fluorescence traces of a linear and a highly nonlinear indicator allow for determination of absolute voltage. This method, though theoretically sound, is currently limited by the lack of bright, fast, and sensitive highly nonlinear reporters, which have not to this point been a target for optimization and screening efforts.

5.2.3 Scenario 1: Dual near-linear indicators

We first consider the linear case with indicators whose fluorescence in the biological voltage range can be represented as $F(t) = a(V(t) - V^0) + b$. V^0 is a fixed biophysical single-reporter property that is independent of imaging or expression conditions, but may depend on temperature, pH, membrane composition, and other physiological variables that may affect the single-molecule response. This constant can be determined by a single patch-clamp measurement in a separate experiment and then is known for all future experiments using that reporter in that cell-type under a

specific set of physiological conditions. Separate calibrations should be performed for different cell types or significantly different physiological conditions.

In the general case, with k spectrally distinguishable and simultaneously measured reporter types and N unique voltage values measured over time, the unknown indicator offsets and scaling and the unknown voltages combine to give $N + 2k$ unknown parameters and kN equations. Due to the linearity of the reporters, any voltage trajectory projected into the k-dimensional space of fluorescence measurements will result in a line. This means that two separate voltage measurements are sufficient to fully determine this trajectory and also that no more than two linearly independent measurements can be taken. In other words, once fluorescence has been recorded at two distinct voltages, further measurements of fluorescence at different voltages will not provide any additional information about the system. We can therefore restrict our analysis to $N = 2$. We can see that, with $2 + 2k$ unknowns and $2k$ independent equations, we cannot solve the system in this general linear case. However, if background is negligible, so that $F = a(V(t) - V^0)$, we reduce the number of unknowns to $2 + k$ while keeping the number of independent observations at $2k$. This results in a solution for $k \geq 2$. It is a matter of basic algebra to show that for two linear reporters with negligible background:

$$F_A(t) = a(V(t) - V_A^0); F_B(t) = b(V(t) - V_B^0) \tag{5.5}$$

measured at t_1, t_2, we can express the voltage at t_1 as:

$$V(t_1) = \frac{QV_B^0 - V_A^0}{Q - 1} \tag{5.6}$$

where $Q = \frac{F_A(t_1)\Delta F_B}{F_B(t_1)\Delta F_A}$ and $\Delta F = F(t_2) - F(t_1)$

Because standard semi-quantitative voltage imaging does not require precise characterization of or removal of static background contributions, it was not clear whether this 'negligible background'

linear solution might apply to real-world imaging conditions. We therefore collected data from two modern near-linear GEVIs and designed and tested several variations on an analysis pipeline optimized for background removal and estimation of absolute voltage. This process can be divided into three major phases: data collection, single-channel signal extraction, and absolute voltage estimation by combining information from each channel. In the following section we give an overview of each of these phases, with insight into particular considerations required for absolute voltage imaging, while leaving details of our implementations for the methods section.

5.2.4 Data collection

In addition to the typical considerations of voltage imaging, three further constraints must be considered for dual-indicator imaging. First, it is necessary to choose indicators and imaging filters such that cross-channel crosstalk is minimized. This is particularly important since the fluorescence of both indicators will be responding to the same underlying signal, and so will be inseparable by statistical methods. Second, it is necessary to image the reporters simultaneously relative to the voltage dynamics present in the sample. For samples with slowly varying voltage, it may be sufficient to perform interleaved time-multiplexed imaging by filter or excitation source switching, while for samples, such as spiking neurons, with fast voltage dynamics, it would be necessary to perform true simultaneous imaging either with split-frame dual-wavelength imaging or with synchronized dual-camera imaging. Third, since the robustness of the solution to noise increases with both the sensitivity (slope of F-V curve) of each individual indicator and the difference in sensitivity between the two indicators, it is desirable to choose indicators with significantly different, but large, slopes. These demands are best met with reporters of opposite response direction, but this is not required by the method. Unlike ratiometric reporters, whose expression ratios must be kept fixed, there is no fixed constraint placed on reporter expression ratios, although these ratios may be tuned if desired to produce similar total signal-to-noise ratios (SNR) from reporters with different per-molecule SNR. To

test this method, we expressed Quasar6a[117], a positively-going GEVI, and Voltron1$_{608}$, a negatively-going GEVI on separate plasmids in HEK-293T cells (Fig. 5.1a). Under whole-cell patch clamp, we applied a series of voltage steps and ramps while imaging in one channel, then immediately repeated the identical control waveform while imaging in the second channel.

5.2.5 Single-channel signal extraction

In order to perform accurate dual-channel absolute voltage estimation, it is first necessary to separately extract a high-fidelity representation of each reporter's fluorescence with photobleaching and background removed to negligible levels. These are both standard steps in fluorescent voltage indicator signal processing but must be performed to more stringent standards for absolute voltage imaging. Photobleaching is generally fit with an exponential, which once fit can be used to compensate fluorescence back to a flat baseline. We note that if illumination intensity is not constant across the field of view, photobleaching rates can vary across the sample, requiring separate photobleaching corrections for different pixels or image regions. For voltage dynamics with roughly symmetric variation from the mean, a simple exponential fit can provide good photobleaching correction, while for asymmetric voltage dynamics it may be appropriate to use a more customized fit method (Fig. 5.1b).

Background subtraction begins with subtraction of camera sensor dark counts, followed by subtraction of low-spatial-frequency components due to scattering and out-of-focus sources. In the case of two-dimensional surface-adhered cultured cells, out-of-focus sources are not a problem, so this could be achieved by capturing the fluorescence trace from a cell-free region adjacent to the cell of interest and subtracting this from the signal trace. There exist more complex procedures for general compensation for scattering and out-of-focus background.[137]

One type of background fluorescence that resists separation from signal is that arising from insensitive fluorophores spatially co-located with the sensitive reporters. Such background could result from other fluorophores in the membrane or from misfolded or otherwise blocked reporters

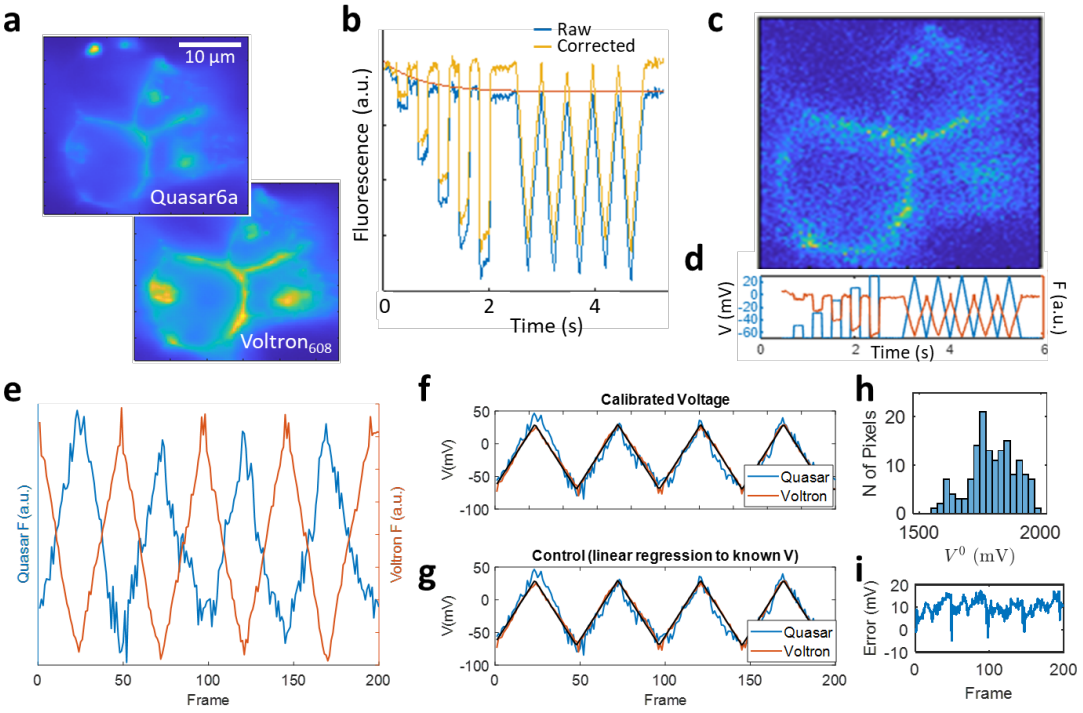

Figure 5.1: a) Image of the Quasar6a and Voltron1$_{608}$ channels of a whole-cell patch-clamped HEK-293T cell expressing Quasar6a and Voltron1$_{608}$. b) Raw Voltron1$_{608}$ fluorescence (blue) and photobleaching-corrected trace (yellow) from cell in (a) under voltage step and ramp stimulus. c) A map of correlation-based pixel weights used for signal extraction in the Voltron1$_{608}$ channel. Several bright agglomerates visible in (a) have low weights, indicating that these pixels contain insensitive background and have been removed from the analysis. d) Extracted Voltron1$_{608}$ signal (orange) overlaid on the control voltage waveform (blue). Only the triangle wave portion is used for further analysis. e) After the signal extraction steps in (a-d) have been performed on both indicators, we have two highly correlated fluorescence traces. f) Calibrated voltage traces predicted from the Quasar (blue) and Voltron1 (orange) fluorescence at the optimal solution at which the root-mean-squared distance (RMS) between the two predictions is minimized. The actual voltage is in black. The Voltron1 fluorescence trace has a higher SNR, so its prediction is taken as the best prediction. The calibrated Voltron1 trace has a systematic offset of 0.07 mV, an RMS error of 3.6 mV, and a scaling error of 0.8%. g) As a control, the fluorescence traces were separately fit to the known control voltage with a least-squares linear fit. The resulting traces are nearly identical to the results obtained via calibration without knowledge of the voltage (except to determine V^0). The linearly fit Voltron1 trace has a systematic offset of -0.06 mV, an RMS error of 3.6 mV, and a difference of standard deviation of 0.8% from that of the known voltage. h) Histogram of V^0 estimates from 1% of pixels from Voltron1$_{608}$ recording with highest voltage sensitivity. The distribution has a standard deviation of 180 mV. i) Systematic error resulting from a 10 mV perturbation in the V^0 estimate for Quasar6a. The predicted trace now has an offset of 10 mV.

in the membrane (e.g., Voltron1 with no retinal bound in the opsin core). In certain cases where such background is present in only a subset of membrane-pixels, it may still be possible to remove

it. Here, we use a previously described weighting method[41] to select the most sensitive (lowest background) pixels (Fig. 5.1c,d).

5.2.6 Estimating Absolute Voltage

While the explicit two-point linear solution described above can be extended into a many-point solution, we found that in practice a solution based on numerical optimization is more robust to the noise present in fluorescence traces. This optimization relies on the insight that the families of possible voltage solutions resulting from the two fluorescence channels coincide only at a single point in solution space, which is the absolute voltage solution to the system. Minimizing the error between the voltage predictions generated by the two channels over the space of possible scaling coefficients therefore provides a solution to the system that is robust to noise in the traces. On a calibration dataset (Fig. 5.1e) in which the background was assumed to be negligible and the effective V^0 was determined from the calibration data itself, this optimization produced a solution with a systematic offset error of < 0.1 mV, a systematic scaling error of <1%, and a root-mean-squared (RMS) error of <4 mV (Fig. 5.1f). This optimized solution is as good on all measures as a solution derived by fitting the fluorescence traces to the known voltage (Fig. 5.1g), indicating that remaining error is attributable to noise in the fluorescent traces.

In order to perform this analysis, the V^0 of each indicator must be known beforehand to a high level of precision, as error in V^0 propagates to an error of comparable absolute magnitude in estimated voltage. These values should be constant across cells and samples (although there may be some variation between cell types due to different membrane compositions and/or cytoplasm ionic composition) and can therefore be determined in separate calibration experiments. In real samples, though, we found that best estimates of V^0 vary widely between, and even within cells (Fig. 5.1h). This is likely the result of uncorrected background, as nonzero background appears in the fluorescence-voltage relation as $F = a(V - (V^0 - \frac{b}{a}))$, where the intercept of the F vs V curve on the

x axis will be $V^0_{eff} = V^0 - \frac{b}{a}$. For a reporter with a V^0 of ±1000 mV, an uncorrected 1% background contribution will perturb V^0_{eff}, and therefore estimated voltage, by ∼10 mV (Fig. 5.11). This leaves the dual-linear reporter method under-constrained, and leads us to propose a second, more robust technique that, while closely related to the first, is robust to non-negligible background.

5.2.7 Scenario 2: Combined near-linear and highly nonlinear indicators

The dual linear indicator approach fails because the low dimensionality of the fluorescence readout does not provide sufficient information to fix a unique solution when both arbitrary scaling and background are present. For every affine transformation of the fluorescence axis that transforms a linear voltage indicator response, we can find an affine transformation of the voltage axis that has exactly the same effect on the line, preventing us from assigning a unique calibration. This is not true for nonlinear indicators. If we replace one of the near-linear indicators with a highly nonlinear indicator, such as FlaSh[158], the trajectory in F-F space no longer falls on a line and can therefore provide enough information to solve the system for absolute voltage. A sigmoidal nonlinear response has certain features that are invariant to affine transformations of the fluorescence axis (e.g., inflection point and points of maximum curvature). We can therefore use these features to provide a calibration that is robust to arbitrary scaling and background.

The first two steps of this pipeline are nearly identical to the data collection and single-channel signal extraction steps of the dual linear indicator pipeline. While the requirements for the linear indicator are similar to those described above (linearity, sensitivity, avoidance of crosstalk, etc.), there are important additional considerations in the choice of the nonlinear indicator that may lead to different indicators being appropriate for different experiments. Not only are the overall brightness, sensitivity, and speed of the indicator important, but it is also necessary to match the horizontal scale and position of the nonlinearity to the voltage dynamics explored during the experiment. A nonlinearity that is too broad relative to the sampled voltage will appear linear within the sampled

domain, reverting to the linear case described above, while a nonlinearity that is too narrow will be sampled as a step function with all of the nonlinearity condensed to a single point, insufficient for calibration of both scaling and offset throughout the sampled voltage range. While removing background is not as critical as in the linear case, it is still good practice to remove as much noise, including background, as feasible before attempting absolute voltage estimation.

To test this method, we found an indicator, FlaSh[158], that has what appears to be an ideally-situated nonlinearity for measurements spanning -70 to 0 mV. The nonlinearity is centered on -40 mV and saturates about 20 mV from the inflection point. Unfortunately, we found that FlaSh does not traffic properly in HEK-293T cells and were unable to perform recordings. This is consistent with reports of poor mammalian expression and trafficking of FlaSh variants.[159] We therefore generated a simulated nonlinear trace by applying a FlaSh-like nonlinearity (Fig. 5.2a) to the Voltron1_{608} traces recorded earlier. We added scaled random noise and then applied our algorithm to the simulated nonlinear trace together with the original linear trace (Fig. 5.2b).

5.2.8 Estimating Absolute Voltage

Before a nonlinear indicator can be used for absolute voltage estimation, a calibration must be performed to obtain the shape of the indicator's F-V relationship (Fig. 5.2a). Typically, such a curve is obtained and reported during initial development of a voltage reporter, so it should not be necessary to repeat the calibration unless working in a cell type with significantly different membrane or ionic composition than that used in previous characterizations. No calibration is necessary for the linear indicator.

An absolute voltage readout can be performed from a linear/nonlinear pair of arbitrarily scaled and offset fluorescence traces as follows. Using the linear indicator fluorescence as the x axis and the nonlinear indicator fluorescence as the y axis, a scatterplot of all recorded timepoints from a single electrically compact unit is made (Fig. 5.2c). The known shape of the nonlinear indicator response

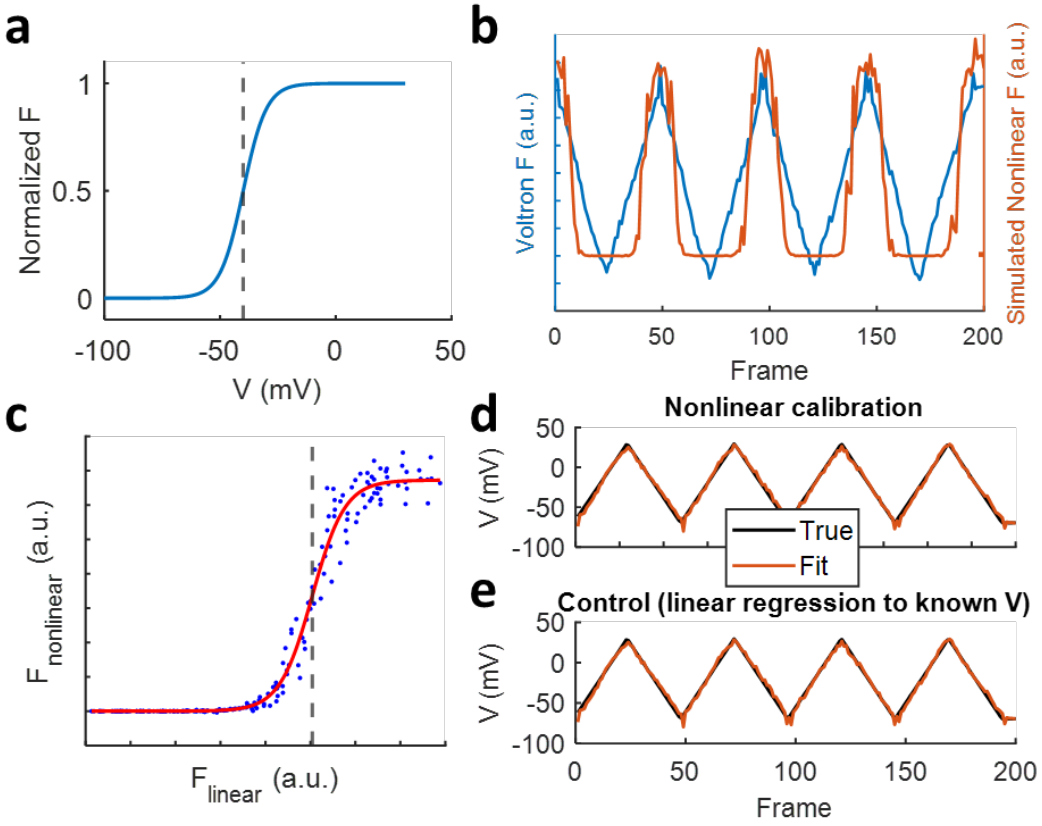

Figure 5.2: a) A simulated calibration for a nonlinear indicator with steep nonlinearity around -40 mV (dashed line) and high sensitivity. b) Experimental linear fluorescence from Voltron1$_{608}$ (left axis, see Fig. 5.1e) and simulated nonlinear fluorescence (right axis). Nonlinear fluorescence was generated by nonlinearly transforming the experimental linear fluorescence, then adding random noise scaled with the square root of the transformed signal. c) Scatter plot of nonlinear versus linear fluorescence at each time point. The sigmoidal calibration curve for the indicator from panel (a) is then fit to the scatterplot (fit inflection point dashed line), producing a calibration between the linear fluorescence and the absolute voltage. d) Resulting calibrated voltage trace (orange) compared to the actual control voltage (black). The calibrated Voltron1 trace has a systematic offset of -0.4 mV, an RMS error of 3.7 mV, and a scaling error of 1.1%. e) As a control, the linear fluorescence trace was fit to the known control voltage with a least-squares linear fit. The resulting trace (orange) is shown with the true control voltage (black) and is similar to the results of the nonlinear calibration performed without any knowledge of voltage. The linearly fit Voltron1 trace has a systematic offset of -0.06 mV, an RMS error of 3.6 mV, and a scaling error of 0.8%.

curve is fit to these data by allowing arbitrary scaling and offset in both dimensions. The optimal scaling and offset parameters for the linear indicator fluorescence (x) axis, if inverted, provide a mapping of the fluorescence of the linear indicator back to voltage on an absolute scale. The end result is a trace whose shape and high-frequency components are derived from a single fluorescent voltage indicator, as in standard voltage imaging, but whose absolute position and scaling on the voltage axis are determined from calibration by the nonlinear indicator (Fig. 5.2d).

Applying this algorithm to our partially simulated data produced a solution with a systematic offset error of < 0.5 mV, a systematic scaling error of <2%, and an RMS error of <4 mV (Fig. 5.2d). This optimized solution is similar to a solution derived by fitting the fluorescence traces to the known voltage (Fig. 5.2e), with slightly worse offset and scaling errors, indicating that most of the remaining error is attributable to noise in the fluorescent traces.

This summary assumes that the scaling factors and background are constant over time. If these components do vary over the course of a recording (e.g., in imaging of growing cells in developing embryos), it would be simple to divide the full recording into blocks, within which separate calibration fits are performed and interpolated while maintaining complete continuity in the resulting trace. The only restriction is that calibration requires sufficient sampling of the nonlinearity to perform a fit. Blocks in which voltage does not vary sufficiently can have their calibration interpolated from more active surrounding regions.

A variation of this method could be applied even to cells which do not exhibit voltage dynamics. By co-expressing an optogenetic channelrhodopsin actuator, one could periodically apply a brief light stimulus to force the cell to sample a sufficient range of voltage to perform the absolute voltage calibration. This would enable absolute determination of the resting voltage of electrically inactive cells with only sparse periods of disruption.

While we were able to perform simulations based on nonlinearly transformed experimental data from a linear indicator, we were not able to fully demonstrate this nonlinear calibration method

due to inadequate performance of existing nonlinear indicators. We found that the fast, bright, and sensitive reporters such as Voltron1 and ASAP that have resulted from extensive optimization efforts are too linear for such calibration, while older more nonlinear reporters such as FlaSh do not provide the signal-to-noise ratio necessary for robust imaging in mammalian cells. The Butterfly[74] GEVI shows desirable nonlinearity, sensitivity, and speed but relies on FRET between two fluorescent proteins, spectrally ruling out their use with a second fluorescent voltage reporter.

5.3 Discussion

Previously described methods for absolute voltage imaging have attempted to calibrate fluorescence traces on a point-by-point basis or by a separate and disruptive calibration step. We propose combining a near-linear voltage indicator with a highly nonlinear indicator selected for the voltage range under consideration. By considering the entire pair of fluorescence traces as a system of equations, a more robust estimation of absolute voltage may be performed. Unlike previously proposed ratiometric techniques, our method does not require fixed expression ratios and is not affected by differential photobleaching. Additional instrumentation complexity is minimal, as simultaneous two-channel imaging can be implemented in a straightforward manner by temporal multiplexing, spatial multiplexing over a single camera sensor, or dual-camera imaging.

One limitation of this technique is that the measured voltage must sample the range of the nonlinearity on a timescale faster than photobleaching, uncorrected sample motion, or changes to the scaling coefficient or background. This is likely not a problem for highly-active neurons, but could prevent calibration in silent neurons or in systems like developing embryos in which voltage changes are slow and subtle. One option in these cases would be to introduce intermittent voltage perturbations, whether optogenetically or pharmacologically, to force the system to sample a range of voltages at sparse intervals. This might be acceptable in some systems, but could cause unwanted

perturbation in others. For very slowly-varying voltages, fluorescence lifetime imaging-based techniques may be a better solution for absolute voltage imaging.

We were prevented from an experimental demonstration of this technique by a lack of suitable bright and sensitive nonlinear voltage indicators. We suspect that this lack is due not to any inherent difficulty in developing or discovering such reporters, but due to a bias towards developing and publishing reporters with higher linearity due to their more faithful reporting of the shape of voltage dynamics in standard semiquantitative voltage imaging. Although voltage indicator development is by no means an easy process, the vast improvements in linear voltage reporters over the past decade give us reason to believe that the development of nonlinear indicators suitable for absolute voltage imaging is well within the capabilities of the research community. In fact, we cannot discount the possibility that such an indicator has already been discovered but has not been optimized or published due to its unsuitability for standard relative voltage imaging. We hope that by publishing this work at an early stage we may encourage effort to be put into developing, improving, and sharing nonlinear indicators that may have been previously seen as unsuitable for voltage imaging.

5.4 Methods

5.4.1 Genetic constructs

Voltron1 plasmid was obtained from Addgene (#119033). The Voltron1 sequence was cloned into a lentiviral backbone with a CMV promoter using standard Gibson Assembly. Briefly, the vector was linearized by double digestion using restriction enzymes (New England Biolabs). DNA fragments were generated by PCR amplification and then fused with the backbones using NEBuilder HiFi DNA assembly kit (New England Biolabs). Resulting plasmids were verified by sequencing (GeneWiz). The Quasar6a plasmid is Addgene #178822.

5.4.2 HEK cell culture

HEK293T cells were maintained in tissue culture-treated culture dishes (Corning) at 37 °C, 5% CO2 in Dulbecco's Modified Eagle Medium supplemented with 10% fetal bovine serum, 1% GlutaMax-I, penicillin (100 U/mL), streptomycin (100 mg/mL). For each imaging experiment, cells in one 35 mm dish were transiently transfected with both Voltron1 and Quasar6a using TransIT-293 lipofection reagent (Mirus Bio). For lipofection, plasmids were combined and then diluted with empty pUC19 vector (New England Biolabs) to a final ratio of 1:1:3 Quasar6a:Voltron1:pUC19 by mass and then transfected with 7.5 μL of TransIT-293 and 2.5 μg of DNA. Cells were replated 36-60 hours after transfection on glass-bottomed dishes (Cellvis, Cat. # D35-14-1.5-N) that were previously coated in poly-D-lysine to aid in cell adhesion.

5.4.3 Electrophysiology and Buffers

Half an hour prior to imaging, JF_{608}-HaloTag ligand dye was added to the medium in each dish of cells to a final concentration of 100 nM. Immediately prior to imaging, the medium was removed, and the cells were rinsed, then covered with dye-free extracellular (XC) buffer. The XC buffer contained 125 mM NaCl, 2.5 mM KCl, 3 mM $CaCl_2$, 1mM $MgCl_2$, 15 mM HEPES, 20 mM glucose, which was adjusted with NaOH to a pH of 7.3 and with sucrose to an osmolality of 305-310 mOsm, as measured by a vapor-pressure osmometer (Wescor). Filamented patch pipettes were pulled using an automated puller (Sutter P-1000) to a tip resistance of 6 MΩ and were filled with an intracellular buffer (IC) containing (in mM) 6 NaCl, 130 K-aspartate, 2 $MgCl_2$, 5 $CaCl_2$, 11 EGTA, and 10 HEPES, with pH adjusted to 7.2 by KOH. Whole-cell voltage clamp was acquired using a modified syringe to manipulate pressure, following Li. [100]

5.4.4 Microscope and illumination control

One-photon (1P) imaging experiments were performed on a custom-built inverted microscope with a computer-controlled patch amplifier (Axon Instruments, Multiclamp 700B). Once a whole-cell patch was established, acquisition was controlled using custom MATLAB/C++ acquisition software (https://www.luminosmicroscopy.com/, chapter 4). The illumination path contained a 594 nm laser (Hübner Photonics, Cobolt Mambo) and a 635 nm laser (Dragon Lasers). Imaging was performed through a high-NA 60x water-immersion objective (Olympus UPLSAPO60XW, 0.28 mm working distance, NA = 1.2) onto an sCMOS camera (Hamamatsu, ORCA-Flash 4.0). Imaging of was performed through a 50:50 beam splitting prism instead of a dichroic to avoid disturbing the patch while changing dichroics. A 594 nm long-pass emission filter (Semrock, BLP01-594R-25) and a 700 nm long-pass emission filter (Thorlabs) were used for Voltron1$_{608}$ and Quasar6a imaging, respectively. Electrical waveforms and measurements were transduced through a computer-controlled data acquisition device (National Instruments, PCIe-6343). The sample was placed on a 2-axis motorized stage (Ludl Electronic Products, MAC6000), and a 3-axis micromanipulator was used for patch pipette control (Sutter, MP-285).

5.4.5 Analysis: Signal extraction

Analyses were performed using custom MATLAB code. Analysis of recorded fluorescence videos began with background subtraction by subtraction of a cell-adjacent region of interest (ROI). Photobleaching correction was performed in two steps. First, a biexponential decay was fit to the lower (Quasar6a) or upper (Voltron1) hull of the entire averaged cell ROI trace. This accounts for the asymmetric voltage deviations of our waveform. Afterwards, this global biexponential was individually scaled and applied to each pixel's trace to account for differential rates of photobleaching across a field of view. Bleaching appeared to affect mainly the non-voltage-sensitive background, decreas-

ing overall fluorescence without affecting the absolute magnitude of fluorescent response to voltage. We therefore applied the photobleaching correction additively.

Signal extraction used a previously described pixel-weighting technique.[41] Briefly, the whole cell ROI trace was assumed to correlate well with voltage. The correlation of each individual pixel to this trace was calculated, with more highly correlated pixels representing more voltage-sensitive pixels. The final weights were calculated by weighting the correlations according to the residual pixel noise level to emphasize lower-noise pixels. The final cell fluorescence trace was calculated by applying these weights to each frame of the recorded video.

5.4.6 Analysis: Linear voltage estimation with negligible background

Our analysis of voltage estimation from two linear indicators posits that the parameter V^0 is constant between cells and recording setups. In the negligible background case, this parameter is found by extrapolating the F vs V relationship to zero fluorescence. We calculated V^0 for each indicator and cell with a linear fit of fluorescence to the known control voltage. This is the only way in which we use the known control voltage during the entire analysis. In order to show the variation of V^0 among pixels, we linearly fit each pixel to the control voltage to find the intercept, then selected the 1% of pixels with the highest weights (see section on signal extraction) and plotted a histogram of the V^0 of these pixels. We did not use these pixelwise V^0 for further analysis.

We found that a numerical optimization algorithm gave more robust results than voltage estimation using the closed form solution. For each indicator, i, a given trial scaling factor, a_i, will predict a voltage trace with a certain offset and scaling. For zero-noise fluorescence traces, there is a unique solution of a_1, a_2 for which the predicted voltage traces, $V_1(t)$, $V_2(t)$, are identical, with the same offset and scaling. We therefore used the MATLAB global optimization toolbox pattern search optimizer to minimize the difference between the two voltage traces predicted on the space of possible scaling coefficients. Mathematically, the objective function was the temporal mean of the squared

difference between the two predicted traces, with the traces first normalized to the total range of the combined traces. Normalization was necessary to prevent the objective from simply minimizing the scale of the traces. The only constraints were on the sign of the scaling factors, consistent with the known direction of each reporter's response. Pattern search converged on a solution within twenty-six iterations. The total offset of the final solution was calculated as the difference between the mean of the predicted voltage and the mean of the true voltage. Total scaling error was calculated as the relative difference between the standard deviation of the predicted voltage and the true voltage. In order to test the robustness of the estimation to variation in V^0, we manually added an offset of 10 mV to the V^0 estimate for Quasar6a. This resulted in a shift of the estimated voltage by $\sim$10 mV (Fig. 5.11).

5.4.7 Analysis: Nonlinear voltage estimation simulation

We began with the same Voltron1 fluorescence trace used for linear voltage estimation. In order to generate a simulated nonlinear trace, we first back-calculated a noisy voltage trace using a linear fit of the Voltron1 fluorescence to the known voltage. We generated a sigmoidal nonlinearity with inflection point at -40 mV and slope of 0.2 based approximately on the response of FlaSh and applied this nonlinearity to the noisy voltage trace. We scaled the result so that its maximum value matched the maximum fluorescence of the original data. In order to remove spurious correlations with the original linear trace, we applied to each timepoint of the simulated trace additive Gaussian noise with a standard deviation of half of the square root of the simulated value (the weighted average traces do not represent real photon count numbers, so exact Poisson noise would be inappropriate).

Fitting of the sigmoid to the data was performed using MATLAB's curve fitting toolbox. A sigmoid of form $F_{NL} = \frac{A}{1+e^{B(F_L-I)}} + O$ was fit to the paired fluorescence traces on the space of A, B, I, O. The predicted voltage was then calculated as $V_{pred} = I_V + \frac{B}{B_V}(F_L - I)$, where I_V and B_V are the known inflection point and slope of the indicator's calibration curve on an absolute voltage abscissa.

Fit error was calculated in the same way as for the linear solution.

5.5 Manuscript Information

5.5.1 The author's contributions

Frederick Brooks, Hunter Davis, and Adam E. Cohen conceived this work. Frederick Brooks acquired and analyzed the data and performed all modelling. Frederick Brooks and Adam E. Cohen wrote the manuscript. Adam E. Cohen supervised the work.

6

Conclusion

This dissertation expands the quality and availability of tools for robust biological voltage imaging, with a focus on applications in the brain. While each chapter of this dissertation pursued a particular problem in the voltage imaging field, the greater thread that ties these chapters together is the aim of improving the quality and ease of use of voltage imaging tools to the point at which neuroscientists (and other biologists) will be able routinely to apply voltage imaging to their problems of interest, making scientific discoveries that are out of reach of other techniques.

In chapter one, I motivated this work by comparing the current state of the field to the similar field of neural calcium imaging and described three shortcomings that I would address in the following chapters. In chapter two, I addressed the first of these shortcomings by discovering the mechanism of loss of sensitivity of rhodopsin-based indicators under two-photon conditions and demonstrating successful *in vivo* two-photon imaging with an indicator that had previously resisted efforts at two-photon imaging. In chapter three, I discussed in depth the unique optical constraints on two-photon voltage imaging in order to provide a framework for design of optimal sensors and microscopes. In chapter four, I presented an open-source microscope control software package that is designed to make optical electrophysiology instrumentation accessible to a wider audience. In chapter five, I studied the possibility of calibrating intensity-based fluorescent voltage sensors by using a combination of two indicators. In this final chapter, I will discuss some of the implications, limitations, and future directions of this work, with focus on biologists, GEVI developers, and developers of voltage imaging instrumentation.

6.1 Implications for the biologist

A biologist should be cautious but optimistic in light of this work. Cautious because the optical limitations on two-photon voltage imaging set out in chapter three may prevent voltage imaging from fulfilling naïve expectations carried over from calcium imaging. Imaging of fast changes in voltage that are localized to cell membranes is inherently more difficult than imaging of slower signals that can be transduced through the volume of a cell. Voltage imaging will therefore likely always require greater effort or expense for a comparable number of measured cells. As we described, it will also face tighter biophysical limits on the number of cells measured. We also caution voltage imaging users to understand the effect of illumination intensity on reporter sensitivity, based on our discoveries in chapter two. Reporters used in intensity regimes significantly different from those under

which they were characterized may have significantly different sensitivity curves.

With that healthy bit of caution, a biologist should be excited about the field. Within the constraints explored in chapter three, there is still much room for improvement. Some possible avenues touched on in this dissertation involve decreasing laser repetition rate, improving targeting efficiency, and developing better methods for signal extraction. In addition, a biologist can look forward to high performance fast rhodopsin GEVIs for two-photon imaging based on the discoveries presented in chapter two, and to an easily applied technique for absolute voltage imaging based on the theoretical analysis in chapter five, once appropriate nonlinear indicators are published. Finally, a biologist desiring to perform high-speed optical electrophysiology in the lab need not create complicated custom instrumentation control code but can download and use the open-source modular control software presented in chapter four. The most significant remaining barrier is the lack of commercial hardware solutions for voltage imaging at this time. A biologist wishing to perform voltage imaging beyond very simple experiments will likely need a highly modified or fully custom microscope.

6.2 Implications for the GEVI developer

The central aim of the research presented in chapter two was to demonstrate two-photon imaging of a fast opsin-based GEVI *in vivo*. We achieved this aim, but the photophysical discoveries that enabled this success may have more long-term impact. First, our finding that Voltron sensitivity depends on illumination intensity prompts us to urge GEVI developers to publish sensitivities at a range of illumination intensities. Second, our results open avenues for development of improved two-photon rhodopsin GEVIs. Voltron2 was developed based on its optimal performance under one-photon excitation, which does not imply optimal performance under two-photon conditions. A better two-photon indicator could possibly be generated using a targeted screen or design process.

Given the high dimensionality of two-photon excitation parameters, however, such a screen would require either some starting point or a photophysical understanding of rhodopsin-GEVI sensitivity under two-photon conditions. Our results provide both an initial starting point (Voltron2$_{608}$ under 1 kHz scanning 1135 nm excitation) and a photophysical understanding of how sensitivity emerges in a rhodopsin indicator. We expect that future engineering or selection efforts to improve dye and retinal spectral overlap, decrease relaxation to the voltage insensitive state, or tune two-photon voltage sensitivity into the range of a standard titanium-doped sapphire (Ti:Sapph) laser could yield significantly better two-photon voltage indicators.

Other chapters should also inform the work of GEVI developers. The scaling laws developed in chapter three suggest that improvements in GEVI sensitivity would have a large impact on voltage imaging performance. Improvements in photostability, by dye [160,161] or fluorescent protein [162] engineering, would also have a large impact on performance by increasing the pulse energy threshold for sensors that are photobleaching-limited. Our discussion of kinetics suggests that development of indicators for neural spike detection should focus on improving the speed of response to positive voltage changes and that speed of response to re-polarization should be left just fast enough to avoid overlap of subsequent spike responses. Finally, our theoretical exploration of absolute voltage sensing in chapter five gives a new importance to nonlinear voltage indicators. We would urge GEVI developers not to discard indicators solely because of poor linearity. In fact, a spectrally diverse library of fast and sensitive GEVIs with nonlinearities of different slopes and offsets would be a powerful tool for absolute voltage imaging of different biological signals.

6.3 Implications for the instrumentation developer

The several chapters of this dissertation present specific opportunities, a set of guideposts, and a general challenge to developers of voltage imaging instrumentation. The demonstration of *in vivo*

two-photon imaging with Voltron2$_{608}$ invites development of two-photon microscopes tailored to the spectral and temporal requirements we discuss in that chapter. In particular, the 1135 nm pulsed excitation source we used is outside the wavelength range provide by most commercially available tunable-wavelength Ti:Sapph and fixed-wavelength fiber lasers.[163,164] Development of lower cost pulsed lasers capable of 1135 nm operation would allow broader adoption of the technique. In addition, our model suggests that interleaving orange (594 nm) photoactivation light with periods of two-photon excitation could enable voltage-sensitive imaging with a shorter-wavelength femtosecond laser. While we did not experimentally test this hypothesis, it would be a promising avenue for further research, accompanied by design of a microscope with built-in capabilities for interleaved one and two-photon excitation. A third specific opportunity is the design of two-photon imaging systems that provide high duty cycle illumination, minimizing the time between pulses when sensors are allowed to decay back to the voltage insensitive state. This could be accomplished either by efficiently-targeted point scanning to minimize off-target time or by scanless techniques[68] that allow revisit of each point at the laser repetition rate, though such scanless techniques may optically less efficient, as discussed in chapter three.

Chapter three provides a set of guideposts for voltage imaging instrumentation development. Our goal is not to argue for any specific ideal implementation, but rather to present the limits that any technique must face and the tradeoffs that must be made when optimizing for different performance parameters. Certain limits (e.g., the photon shot noise limit) are fundamental; the instrumentation developer's goal should not be to overcome such limits, but to come as close to the theoretical limit as practically possible given all other constraints. Other limits (e.g., point scanning speed, laser repetition rate) are not absolute; a microscope that could provide repetition-rate scanning of arbitrary points in a field of view would bring the field significantly closer to ideal two-photon imaging. Our discussion centered on optical constraints. These are of course not the only constraints. Besides the engineering constraints of available laser repetition rates and scanning

speeds, *in vivo* imaging also faces noise from motion and blood flow. While point-scanning is the optimal technique under hypothetical ideal shot-noise-limited conditions, a different technique may be optimal under any given set of real-world conditions. Any implementation will face the same fundamental limits and tradeoffs that we describe, and we believe that the comprehensive treatment we provide in chapter 3 will be a useful reference for those working on all types of voltage imaging microscopes.

Chapter four presents an accessible software package for voltage imaging microscope control. This software is only half of the solution. This dissertation challenges instrumentation developers to develop and disseminate, either commercially or open source, user-friendly microscope hardware for voltage imaging. While published implementations of high-speed microscopes suitable for voltage imaging abound, [38,63–71,110], recreating one of these microscopes typically requires significant optical expertise, to the extent that other instrumentation-development labs are hesitant to attempt to implement some of the more complex designs. Even a more basic microscope for one-photon voltage imaging requires components, such as micromirror patterning devices, that significantly complicate optical design and may put a self-build of a voltage imaging microscope out of reach of many neuroscience labs. Given the Luminos control software we present in chapter four, we believe that design, implementation, and distribution of a one-photon voltage imaging microscope with patterned illumination is within the reach of the field, and that an equivalent system designed for two-photon voltage imaging will likely be feasible within a slightly longer time window. We encourage instrumentation developers to focus now on designs that have potential for broader distribution, and to work with industry experts to make those designs available to labs that are eager to obtain ready-made voltage imaging microscopes.

The software presented in chapter four is not the product of trained software developers. Nor was it released only after attaining a completely stable state. We have been using this software internally on seven custom microscopes in our lab, with development going back to 2020. While there

are still known bugs and instabilities, we believe that Luminos is likely to provide an easier entry and more robust function than any alternative solution short of professional custom code now available for highly synchronized complex acquisition. We have released it publicly with two goals in mind. First, we hope that releasing this code now will encourage a significant part of the voltage imaging field to coalesce around a standardized system for recording and saving voltage imaging data. This would allow consistent sets of experimental metadata to be stored, and would enable standardized analysis and data archiving solutions to be developed later so that voltage imaging data can be usefully shared between labs using online repositories such as the BRAIN Initiative DANDI [165] archive. Second, we hope the quality and capabilities of Luminos will be increased by the feedback and code contributions of our users. We encourage any interested developers or neuroscientists to download, test, and contribute to Luminos, and to contact us with any feedback.

6.4 Conclusion

The voltage imaging field is exciting at all levels, combining cutting-edge protein and small-molecule engineering, cutting-edge optical design, and cutting-edge biology. This dissertation has focused on methods and tool development but offers relevant information to those engaged in all aspects of the field. I hope that this work may play a small part at least in enabling fascinating discoveries in neuroscience and biology using the tools and insights I have presented.

A

Supplemental Information for Chapter 3

A.1 Scaling of measurable cells with brightness and voltage sensitivity

Here we derive the dependence of the number of measurable cells on illumination intensity, fluorophore brightness, spike ΔF/F, measurement bandwidth, and target SNR (Eq. 3.2 in the main text). We assume a point-scanning 2P illumination system which has perfect targeting to cell membranes, and which can jump between cells with zero delay. This is a best-case scenario: motion ar-

tifacts, imperfect targeting, and scanner inertia or finite slew rates further degrade the SNR. We also assume a perfect camera, which converts impinging photons to detected counts with 100% efficiency. In order to derive limits on SNR from real-world measurements, we convert the recorded digitized count rate produced by our camera to the number of impinging photons by dividing by the quantum efficiency (QE = ~67% @ 525 nm) and multiplying by the conversion factor (CF = 0.46 photoelectrons/digital count) of our camera. Let F (counts/s) be the rate of photons collected by a perfect detector from a single cell, let P (W) be the laser power at the focus. We define the constant for GEVI brightness, A, empirically as the proportionality between squared laser power and fluorescence signal.

$$F = A \cdot P^2, \tag{A.1}$$

where we have assumed that P is changed by adjusting total laser power, keeping laser repetition rate, pulse width, and focal and scan parameters constant.

The number of photons collected during a spike of duration τ is:

$$N_{photons} = A \cdot P^2 \cdot \tau \cdot \varphi, \tag{A.2}$$

where φ is the fraction of the time that the laser focus intersects the cell membrane. Let β be the fractional change in fluorescence (ΔF/F) during a spike. If there is a contribution to the fluorescence from voltage-insensitive background, then β may be smaller than in the background-free case. The signal is:

$$S = \beta \cdot N_{photons} = \beta \cdot A \cdot P^2 \cdot \tau \cdot \varphi \tag{A.3}$$

Assuming that the voltage change does not substantially affect the shot noise (i.e. $|\beta| \ll 1$), then

the shot noise is:

$$Noise = \sqrt{N_{photons}} = \sqrt{A \cdot P^2 \cdot \tau \cdot \varphi}. \tag{A.4}$$

Thus,

$$SNR = \frac{\beta \cdot N_{photons}}{\sqrt{N_{photons}}} = \beta \cdot P \cdot \sqrt{A \cdot \tau \cdot \varphi} \tag{A.5}$$

This SNR calculation is applicable only when the laser is targeted to a single cell. If the laser sequentially visits N cells, then the duty cycle on each cell is $1/N$. Assuming zero transit time between cells, the number of photons collected per cell scales inversely with the number of cells:

$$N_{photons} = \frac{A \cdot P^2 \cdot \tau \cdot \varphi}{N_{cells}^{2P}}. \tag{A.6}$$

Therefore,

$$SNR = \beta \cdot P \cdot \sqrt{\frac{A \cdot \tau \cdot \varphi}{N_{cells}^{2P}}}, \tag{A.7}$$

and

$$N_{cells}^{2P} = \frac{A \cdot \tau \cdot P^2 \cdot \beta^2 \cdot \varphi}{SNR^2}. \tag{A.8}$$

Equation A.8 shows the strong dependence of the number of measurable cells on the voltage sensitivity, β. The proportionality of SNR and laser power for a single cell holds true for non-scanning excitation modalities as well.[68]

A.2 Scaling of SNR with on and off kinetics

We use the model shown in Fig. 3.4a. We calculate the endpoint, β, and the area under the rising edge, R_{on}, of the response to a stimulus of length t using a reporter with steady-state response, M, and on and off time constants of τ_{on} and τ_{off}.

$$\beta = M\left(1 - e^{-t/\tau_{on}}\right).$$

$$R_{on} = M\int_0^t 1 - e^{-T/\tau_{on}}dT = M\left(t - \tau_{on}\left(1 - e^{-t/\tau_{on}}\right)\right).$$

Similarly, we integrate the full area under the decaying response after the cessation of stimulus. We calculate the integral over the full half-space as the upper bound on response signal.

$$\frac{\Delta F_{off}}{F}(T) = \beta e^{-T/\tau_{off}}.$$

$$R_{off} = \beta\int_0^\infty e^{-T/\tau_{off}}dT = \beta\tau_{off} = M\tau_{off}\left(1 - e^{-t/\tau_{on}}\right).$$

The total response, R, is the sum of these two parts:

$$R = M\left(t + \left(\tau_{off} - \tau_{on}\right)\left(1 - e^{-t/\tau_{on}}\right)\right).$$

To express SNR, we recognize that R takes the place of $\beta \cdot \tau$ in Eq. A.3.

$$S = \beta \cdot \tau \cdot A \cdot P^2 \cdot \varphi = R \cdot F \cdot \varphi.$$

We also set the total integration time, τ, in Eq. A.4 to be $t + \tau_{off}$

$$Noise = \sqrt{A \cdot P^2 \cdot \tau \cdot \varphi} = \sqrt{F \cdot \varphi \left(t + \tau_{off}\right)} \ .$$

We combine to get:

$$SNR = \frac{RF\varphi}{\sqrt{F\varphi \left(t + \tau_{off}\right)}}.$$

A.3 Theoretical comparison of 1P vs 2P photon efficiencies

We use the properties of JEDI-2P as an exemplary GEVI which works under both 1P and 2P excitation. We assume that the 1P and 2P absorption cross sections of the JEDI-2P chromophore are the same as for eGFP. While this assumption may not be exact, modest variations in these cross sections will not change the conclusion that 2P voltage imaging requires 10^4-fold more power per cell.

First, we estimate the per-molecule excitation rate under 1P excitation. To achieve a per-cell detected digital count rate of 1.5×10^7 s^{-1} (equivalent to 10^7 impinging photons/s), required a mean per-cell laser power of 9.6×10^{-7} W, or equivalently an illumination intensity of ~1 W/cm² (Fig. 1; assuming a HEK cell is approximately 10 μm diameter). This intensity is in the middle of the range used for *in vivo* 1P voltage imaging: recordings of Voltron2 in flies used 200 – 1100 mW/cm²,[44] while high-speed recordings of PV cells in mice used up to 14 W/cm².[44]

The decadal molar absorption coefficient of eGFP is ε = 45,000 M-1 cm-1.[166] The per-molecule excitation rate is

$$\Gamma_{1P} = I\varepsilon \frac{\lambda}{h\,c} \frac{10^3 \ln 10}{N_A},$$

where I (W/cm2) is the incident intensity, ε (M-1 cm^{-1}) is the decadal molar absorption coefficient, λ (m) is the wavelength, h (6.63×10^{-34} J s) is Planck's constant, c (3×10^8 m/s) is the speed of light, and NA (6.02×10^{23} mol^{-1}) is Avogadro's number. We assume λ = 488 nm and find that at I =

1 W/cm², Γ_{1P}=430 s⁻¹; at 10 W/cm², Γ_{1P}=4300 s⁻¹.

Assuming an overall 10% total light collection efficiency (reasonable for a high NA optical system), 10^7 collected photons/s corresponds to 10^8 emitted photons/s. At a per-molecule emission rate of 430 s⁻¹, this implies 2.3×10^5 molecules/cell. At a typical HEK cell membrane surface area of 1000 μm², [167] the density of reporters is 230 μm⁻².

We now estimate the 2P power needed to match the emitted count rate of 10^8 s⁻¹. The probability that a fluorophore is electronically excited by a single pulse from a 2P optical system is: [55]

$$P_{2P} = \frac{\sigma_2 P_{avg}^2}{\tau_{2P} f_{2P}^2} \left(\frac{[NA]^2}{2\hbar c \lambda} \right)^2 ,$$

where σ_2 is the 2P absorption cross section (m⁴ s), P_{avg} (W) is the time-average power from the laser, τ_{2P} (s) is the pulse duration, f_{2P} is the laser repetition frequency, NA is the objective lens numerical aperture, and $\hbar$, c, and λ are as above. The per-molecule rate of excitation is $\Gamma_{2P} = f_{2P} P_{2P}$.

We assume parameters typical of a 2P imaging experiment: NA = 1, λ = 920 nm, τ_{2P} = 200 fs, f_{2P} = 80 MHz. The 2P absorption cross section of eGFP is σ_2 = 39 GM (39×10^{-58} m⁴ s). [166]

The brightest signal from the cell arises when the laser focus intersects an equatorial membrane, so the optical axis lies in the plane of the membrane, as in Fig. 4c. In this case the membrane area that is optically excited is approximately $A_{2P} = w_0 b$, where wo is the waist of the Gaussian focus and b is the depth of focus. The focus waist is approximately $w_0 = \frac{\lambda}{2NA}$, and the depth of focus is $b = 2\pi w_0^2 n/\lambda$, where n = 1.33 is the index of refraction. This estimate yields $A_{2P} \sim 1$ μm², implying that ~230 reporter molecules are in the 2P focus. To achieve a total emitted photon rate of 108 s-1 then implies a per-molecule emission rate of □2P = 4.3×10^5 s⁻¹. The time-average laser power to achieve this count rate is 8 mW, 10^4-fold higher than the 1P power to achieve the same count rate. In the minimal SNR limit of 2.5×10^5 detected photons/s/cell (corresponding to 2.5×10^6 emitted photons/s/cell), the minimum time-average 2P power per cell is 0.4 mW (assuming φ = 1).

References

[1] Bruce P. Bean. The action potential in mammalian central neurons. *Nature Reviews Neuroscience*, 8(6):451–465, 6 2007. publisher: Nature Publishing Group.

[2] Yuki Bando, Michael Wenzel, and Rafael Yuste. Simultaneous two-photon imaging of action potentials and subthreshold inputs in vivo. *Nature Communications*, 12(1):7229, 12 2021.

[3] Jacques Duchateau and Roger M. Enoka. Human motor unit recordings: Origins and insight into the integrated motor system. *Brain Research*, 1409:42–61, 8 2011.

[4] Emily Sempou, Valentyna Kostiuk, Jie Zhu, M. Cecilia Guerra, Leonid Tyan, Woong Hwang, Elena Camacho-Aguilar, Michael J. Caplan, David Zenisek, Aryeh Warmflash, Nick D. L. Owens, and Mustafa K. Khokha. Membrane potential drives the exit from pluripotency and cell fate commitment via calcium and mtor. *Nature Communications*, 13(1):6681, 11 2022. publisher: Nature Publishing Group.

[5] Jonatan M. Benarroch and Munehiro Asally. The microbiologist's guide to membrane potential dynamics. *Trends in Microbiology*, 28(4):304–314, 4 2020.

[6] Andrea Biasiucci, Benedetta Franceschiello, and Micah M. Murray. Electroencephalography. *Current Biology*, 29(3):R80–R85, 2 2019. publisher: Elsevier PMID: 30721678.

[7] Junseok A. Kim and Karen D. Davis. Magnetoencephalography: physics, techniques, and applications in the basic and clinical neurosciences. *Journal of Neurophysiology*, 125(3):938–956, 3 2021. publisher: American Physiological Society.

[8] Guosong Hong and Charles M. Lieber. Novel electrode technologies for neural recordings. *Nature Reviews Neuroscience*, 20(6):330–345, 6 2019. publisher: Nature Publishing Group.

[9] Roy V. Sillitoe, editor. *Extracellular Recording Approaches*, volume 134 of *Neuromethods*. Humana Press, New York, 2018. [Online; accessed 2024-04-12].

[10] Chaitanya Chintaluri, Marta Bejtka, Władysław Średniawa, Michał Czerwiński, Jakub M. Dzik, Joanna Jędrzejewska-Szmek, Kacper Kondrakiewicz, Ewa Kublik, and Daniel K. Wójcik. What we can and what we cannot see with extracellular multielectrodes. *PLOS Computational Biology*, 17(5):e1008615, 5 2021. publisher: Public Library of Science.

[11] Alexander D. Reyes. A breakthrough method that became vital to neuroscience. *Nature*, 575(7781):38–39, 11 2019.

[12] Yoshihiro Kubota, Shota Yamagiwa, Hirohito Sawahata, Shinnosuke Idogawa, Shuhei Tsuruhara, Rika Numano, Kowa Koida, Makoto Ishida, and Takeshi Kawano. Long nanoneedle-electrode devices for extracellular and intracellular recording *in vivo*. *Sensors and Actuators B: Chemical*, 258:1287–1294, 4 2018.

[13] Xingxing Liu, Dongxin Xu, Jiaru Fang, Yuheng Liao, Mingyue Zhang, Hongbo Li, Wenjian Yang, Yue Wu, Zhongyuan Xu, Ning Hu, and Diming Zhang. Sensitive and prolonged intracellular electrophysiological recording by three-dimensional nanodensity regulation. *VIEW*, 4(6):20230031, 2023.

[14] Dongxin Xu, Jingshan Mo, Xi Xie, and Ning Hu. In-cell nanoelectronics: Opening the door to intracellular electrophysiology. *Nano-Micro Letters*, 13:127, 5 2021. PMID: 34138366 PMCID: PMC8124030.

[15] Karl Deisseroth and Peter Hegemann. The form and function of channelrhodopsin. *Science (New York, N.Y.)*, 357(6356):eaan5544, 9 2017.

[16] Urs L. Böhm, Yukiko Kimura, Takashi Kawashima, Misha B. Ahrens, Shin-ichi Higashijima, Florian Engert, and Adam E. Cohen. Voltage imaging identifies spinal circuits that modulate locomotor adaptation in zebrafish. *Neuron*, 110(7):1211–1222.e4, 4 2022.

[17] Linlin Z. Fan, Simon Kheifets, Urs L. Böhm, Hao Wu, Kiryl D. Piatkevich, Michael E. Xie, Vicente Parot, Yooree Ha, Kathryn E. Evans, Edward S. Boyden, Anne E. Takesian, and Adam E. Cohen. All-optical electrophysiology reveals the role of lateral inhibition in sensory processing in cortical layer 1. *Cell*, 180(3):521–535.e18, 2 2020.

[18] Madhuvanthi Kannan, Ganesh Vasan, Simon Haziza, Cheng Huang, Radosław Chrapkiewicz, Junjie Luo, Jessica A. Cardin, Mark J. Schnitzer, and Vincent A. Pieribone. Dual-polarity voltage imaging of the concurrent dynamics of multiple neuron types. *Science*, 378(6619):eabm8797, 11 2022. publisher: American Association for the Advancement of Science.

[19] Rafael Pedrosa, Mojtaba Nazari, Majid H. Mohajerani, Thomas Knöpfel, Federico Stella, and Francesco P. Battaglia. Hippocampal gamma and sharp wave/ripples mediate bidirectional interactions with cortical networks during sleep. *Proceedings of the National Academy of Sciences*, 119(44):e2204959119, 11 2022. publisher: Proceedings of the National Academy of Sciences.

[20] Wu Tian, Luxin Peng, Mengdi Zhao, Louis Tao, Peng Zou, and Yan Zhang. Dendritic morphology affects the velocity and amplitude of back-propagating action potentials. *Neuroscience Bulletin*, 38(11):1330–1346, 11 2022.

[21] Helen H. Yang, François St-Pierre, Xulu Sun, Xiaozhe Ding, Michael Z. Lin, and Thomas R. Clandinin. Subcellular imaging of voltage and calcium signals reveals neural processing in vivo. *Cell*, 166(1):245–257, 6 2016.

[22] Bill Z. Jia, Yitong Qi, J. David Wong-Campos, Sean G. Megason, and Adam E. Cohen. A bioelectrical phase transition patterns the first vertebrate heartbeats. *Nature*, 622(7981):149–155, 10 2023. number: 7981 publisher: Nature Publishing Group.

[23] Peter Quicke, Yilin Sun, Mar Arias-Garcia, Melina Beykou, Corey D. Acker, Mustafa B. A. Djamgoz, Chris Bakal, and Amanda J. Foust. Voltage imaging reveals the dynamic electrical signatures of human breast cancer cells. *Communications Biology*, 5(1):1–14, 11 2022. publisher: Nature Publishing Group.

[24] Pin W. Liu, Hongkang Zhang, Christopher A. Werley, Monika Pichler, Steven J. Ryan, Caitlin L. Lewarch, Jane Jacques, Jennifer Grooms, Jean Ferrante, Guangde Li, Dawei Zhang, Nate Bremmer, Adam Barnett, Romina Chantre, Amy E. Elder, Adam E. Cohen, Luis A. Williams, Graham T. Dempsey, and Owen B. McManus. A phenotypic screening platform for chronic pain therapeutics using all-optical electrophysiology. *PAIN*, 165(4):922, 4 2024.

[25] Thomas Knöpfel and Chenchen Song. Optical voltage imaging in neurons: moving from technology development to practical tool. *Nature Reviews Neuroscience*, 20(12):719–727, 12 2019. number: 12 publisher: Nature Publishing Group.

[26] Rishikesh U. Kulkarni and Evan W. Miller. Voltage imaging: Pitfalls and potential. *Biochemistry*, 56(39):5171–5177, 10 2017. PMID: 28745864 PMCID: PMC5715730.

[27] Taylor H. Newton, Michael W. Reimann, Marwan Abdellah, Grigori Chevtchenko, Eilif B. Muller, and Henry Markram. In silico voltage-sensitive dye imaging reveals the emergent dynamics of cortical populations. *Nature Communications*, 12(1):3630, 6 2021. publisher: Nature Publishing Group.

[28] S. Chemla and F. Chavane. Voltage-sensitive dye imaging: Technique review and models. *Journal of Physiology-Paris*, 104(1):40–50, 1 2010.

[29] Rebecca W. Pak, Jeeun Kang, Heather Valentine, Leslie M. Loew, Daniel L. J. Thorek, Emad M. Boctor, Dean F. Wong, and Jin U. Kang. Voltage-sensitive dye delivery through the blood brain barrier using adenosine receptor agonist regadenoson. *Biomedical Optics Express*, 9(8):3915–3922, 7 2018. PMID: 30338164 PMCID: PMC6191611.

[30] Yuki Bando, Masayuki Sakamoto, Samuel Kim, Inbal Ayzenshtat, and Rafael Yuste. Comparative evaluation of genetically encoded voltage indicators. *Cell Reports*, 26(3):802–813.e4, 1 2019.

[31] Madhuvanthi Kannan, Ganesh Vasan, and Vincent Pieribone. Optimizing strategies for developing genetically encoded voltage indicators. *Frontiers in Cellular Neuroscience*, 13, 2 2019.

[32] Jelena Platisa and Vincent A. Pieribone. Genetically encoded fluorescent voltage indicators: are we there yet? *Current Opinion in Neurobiology*, 50:146 – 153, 2018.

[33] Yongxian Xu, Peng Zou, and Adam E Cohen. Voltage imaging with genetically encoded indicators. *Current Opinion in Chemical Biology*, 39:1–10, 8 2017.

[34] Helen H. Yang and François St-Pierre. Genetically encoded voltage indicators: Opportunities and challenges. *The Journal of Neuroscience: The Official Journal of the Society for Neuroscience*, 36(39):9977–9989, 9 2016. PMID: 27683896 PMCID: PMC5039263.

[35] Rosemary C. Challis, Sripriya Ravindra Kumar, Ken Y. Chan, Collin Challis, Keith Beadle, Min J. Jang, Hyun Min Kim, Pradeep S. Rajendran, John D. Tompkins, Kalyanam Shivkumar, Benjamin E. Deverman, and Viviana Gradinaru. Systemic aav vectors for widespread and targeted gene delivery in rodents. *Nature Protocols*, 14(2):379–414, 2 2019. publisher: Nature Publishing Group.

[36] Bok Eum Kang, Lee Min Leong, Yoonkyung Kim, Kenichi Miyazaki, William N. Ross, and Bradley J. Baker. Mechanism of arclight derived gevis involves electrostatic interactions that can affect proton wires. *Biophysical Journal*, 120(10):1916–1926, 5 2021.

[37] Víctor Fernández-Dueñas, Xavier Morató, Thomas Knöpfel, and Francisco Ciruela. Dynamic recording of membrane potential from hippocampal neurons by using a fluorescence resonance energy transfer-based voltage biosensor. In Rafael Lujan and Francisco Ciruela, editors, *Receptor and Ion Channel Detection in the Brain*, pages 523–530. Springer US, New York, NY, 2021.

[38] Zhuohe Liu, Xiaoyu Lu, Vincent Villette, Yueyang Gou, Kevin L. Colbert, Shujuan Lai, Sihui Guan, Michelle A. Land, Jihwan Lee, Tensae Assefa, Daniel R. Zollinger, Maria M. Korympidou, Anna L. Vlasits, Michelle M. Pang, Sharon Su, Changjia Cai, Emmanouil Froudarakis, Na Zhou, Saumil S. Patel, Cameron L. Smith, Annick Ayon, Pierre Bizouard, Jonathan Bradley, Katrin Franke, Thomas R. Clandinin, Andrea Giovannucci, Andreas S. Tolias, Jacob Reimer, Stéphane Dieudonné, and François St-Pierre. Sustained deep-tissue voltage recording using a fast indicator evolved for two-photon microscopy. *Cell*, 185(18):3408–3425.e29, 9 2022.

[39] Claire Deo, Ahmed S. Abdelfattah, Hersh K. Bhargava, Adam J. Berro, Natalie Falco, Helen Farrants, Benjamien Moeyaert, Mariam Chupanova, Luke D. Lavis, and Eric R. Schreiter. The HaloTag as a general scaffold for far-red tunable chemigenetic indicators. *Nature Chemical Biology*, 17(6):718–723, June 2021. Publisher: Nature Publishing Group.

[40] J. M. Kralj, D. R. Hochbaum, A. D. Douglass, and A. E. Cohen. Electrical spiking in escherichia coli probed with a fluorescent voltage indicating protein. *Science*, 333(Journal Article):345–348, 2011.

[41] Joel M Kralj, Adam D Douglass, Daniel R Hochbaum, Dougal Maclaurin, and Adam E Cohen. Optical recording of action potentials in mammalian neurons using a microbial rhodopsin. *Nature methods*, 9(1):90–95, 2012.

[42] Peng Zou, Yongxin Zhao, Adam D. Douglass, Daniel R. Hochbaum, Daan Brinks, Christopher A. Werley, D. Jed Harrison, Robert E. Campbell, and Adam E. Cohen. Bright and fast multicoloured voltage reporters via electrochromic fret. *Nature Communications*, 5(1):4625, 8 2014. number: 1 publisher: Nature Publishing Group.

[43] Ahmed S. Abdelfattah, Takashi Kawashima, Amrita Singh, Ondrej Novak, Hui Liu, Yichun Shuai, Yi-Chieh Huang, Luke Campagnola, Stephanie C. Seeman, Jianing Yu, Jihong Zheng, Jonathan B. Grimm, Ronak Patel, Johannes Friedrich, Brett D. Mensh, Liam Paninski, John J. Macklin, Gabe J. Murphy, Kaspar Podgorski, Bei-Jung Lin, Tsai-Wen Chen, Glenn C. Turner, Zhe Liu, Minoru Koyama, Karel Svoboda, Misha B. Ahrens, Luke D. Lavis, and Eric R. Schreiter. Bright and photostable chemigenetic indicators for extended in vivo voltage imaging. *Science*, 365(6454):699–704, 8 2019. publisher: American Association for the Advancement of Science section: Report PMID: 31371562.

[44] Ahmed S. Abdelfattah, Jihong Zheng, Amrita Singh, Yi-Chieh Huang, Daniel Reep, Getahun Tsegaye, Arthur Tsang, Benjamin J. Arthur, Monika Rehorova, Carl V. L. Olson, Yichun Shuai, Lixia Zhang, Tian-Ming Fu, Daniel E. Milkie, Maria V. Moya, Timothy D. Weber, Andrew L. Lemire, Christopher A. Baker, Natalie Falco, Qinsi Zheng, Jonathan B. Grimm, Mighten C. Yip, Deepika Walpita, Martin Chase, Luke Campagnola, Gabe J. Murphy, Allan M. Wong, Craig R. Forest, Jerome Mertz, Michael N. Economo, Glenn C. Turner, Minoru Koyama, Bei-Jung Lin, Eric Betzig, Ondrej Novak, Luke D. Lavis, Karel Svoboda, Wyatt Korff, Tsai-Wen Chen, Eric R. Schreiter, Jeremy P. Hasseman, and Ilya Kolb. Sensitivity optimization of a rhodopsin-based fluorescent voltage indicator. *Neuron*, 111(10):1547–1563.e9, 5 2023.

[45] Pojeong Park, David Wong-Campos, Daniel G. Itkis, Byung Hun Lee, Yitong Qi, Hunter Davis, Jonathan B. Grimm, Sarah E. Plutkis, Luke D. Lavis, and Adam E. Cohen. Dendritic voltage imaging maps the biophysical basis of plateau potentials in the hippocampus. *bioRxiv*, 3 2024.

[46] J. David Wong-Campos, Pojeong Park, Hunter Davis, Yitong Qi, He Tian, Daniel G. Itkis, Doyeon Kim, Jonathan B. Grimm, Sarah E. Plutkis, Luke Lavis, and Adam E. Cohen. Voltage dynamics of dendritic integration and back-propagation in vivo. *bioRxiv*, 5 2023.

[47] Christine Grienberger, Andrea Giovannucci, William Zeiger, and Carlos Portera-Cailliau. Two-photon calcium imaging of neuronal activity. *Nature Reviews Methods Primers*, 2(1):1–23, 9 2022.

[48] Michael J. Berridge, Martin D. Bootman, and H. Llewelyn Roderick. Calcium signalling: dynamics, homeostasis and remodelling. *Nature Reviews Molecular Cell Biology*, 4(7):517–529, 7 2003.

[49] Martin D. Bootman and Geert Bultynck. Fundamentals of Cellular Calcium Signaling: A Primer. *Cold Spring Harbor Perspectives in Biology*, 12(1):a038802, January 2020.

[50] G. Grynkiewicz, M. Poenie, and R. Y. Tsien. A new generation of ca2+ indicators with greatly improved fluorescence properties. *The Journal of Biological Chemistry*, 260(6):3440–3450, 3 1985.

[51] Roger Y. Tsien. New calcium indicators and buffers with high selectivity against magnesium and protons: design, synthesis, and properties of prototype structures. *Biochemistry*, 19(11):2396–2404, 5 1980.

[52] Atsushi Miyawaki, Juan Llopis, Roger Heim, J. Michael McCaffery, Joseph A. Adams, Mitsuhiko Ikura, and Roger Y. Tsien. Fluorescent indicators for ca2+based on green fluorescent proteins and calmodulin. *Nature*, 388(6645):882–887, 8 1997.

[53] Valerie A. Romoser, Patricia M. Hinkle, and Anthony Persechini. Detection in living cells of ca2+-dependent changes in the fluorescence emission of an indicator composed of two green fluorescent protein variants linked by a calmodulin-binding sequence: A new class of fluorescent indicators *. *Journal of Biological Chemistry*, 272(20):13270–13274, 5 1997.

[54] Jonathan Shapey, Yijing Xie, Elham Nabavi, Michael Ebner, Shakeel R. Saeed, Neil Kitchen, Neil Dorward, Joan Grieve, Andrew W. McEvoy, Anna Miserocchi, Patrick Grover, Robert Bradford, Yau-Mun Lim, Sebastien Ourselin, Sebastian Brandner, Zane Jaunmuktane, and Tom Vercauteren. Optical properties of human brain and tumour tissue: An ex vivo study spanning the visible range to beyond the second near-infrared window. *Journal of Biophotonics*, 15(4):e202100072, 2022.

[55] Winfried Denk, James H. Strickler, and Watt W. Webb. Two-photon laser scanning fluorescence microscopy. *Science*, 248(4951):73, 4 1990.

[56] Martin Oheim, Emmanuel Beaurepaire, Emmanuelle Chaigneau, Jerome Mertz, and Serge Charpak. Two-photon microscopy in brain tissue: parameters influencing the imaging depth. *Journal of Neuroscience Methods*, 111(1):29–37, 10 2001.

[57] Wanyi Tang, Derrick Boateng, Pan Cheng, Quanyu Zhou, Xunbin Wei, and Hao He. Investigation on the optimal wavelength for two-photon microscopy in brain tissue. *AIP Advances*, 8(6):065019, 6 2018.

[58] Rafael Yuste and Winfried Denk. Dendritic spines as basic functional units of neuronal integration. *Nature*, 375(6533):682–684, 6 1995.

[59] Thomas A Pologruto, Bernardo L Sabatini, and Karel Svoboda. Scanimage: flexible software for operating laser scanning microscopes. *Biomedical engineering online*, 2:1–9, 2003.

[60] Daan Brinks, Aaron J. Klein, and Adam E. Cohen. Two-photon lifetime imaging of voltage indicating proteins as a probe of absolute membrane voltage. *Biophysical Journal*, 109(5):914–921, 9 2015.

[61] Xiongbo Liu, Danying Lin, Wolfgang Becker, Jingjing Niu, Bin Yu, Liwei Liu, and Junle Qu. Fast fluorescence lifetime imaging techniques: A review on challenge and development. *Journal of Innovative Optical Health Sciences*, 12(05):1930003, 9 2019.

[62] Qiaole Zhao, Ian T. Young, and de Jan Geert Sander Jong. Photon budget analysis for fluorescence lifetime imaging microscopy. *Journal of Biomedical Optics*, 16(8):086007, 8 2011.

[63] Devin R. Beaulieu, Ian G. Davison, Kıvılcım Kılıç, Thomas G. Bifano, and Jerome Mertz. Simultaneous multiplane imaging with reverberation two-photon microscopy. *Nature Methods*, 17(3):283–286, 3 2020. number: 3 publisher: Nature Publishing Group.

[64] S. Chamberland, H. H. Yang, M. M. Pan, S. W. Evans, S. Guan, M. Chavarha, Y. Yang, C. Salesse, H. Wu, J. C. Wu, T. R. Clandinin, K. Toth, M. Z. Lin, and F. St-Pierre. Fast two-photon imaging of subcellular voltage dynamics in neuronal tissue with genetically encoded indicators. *Elife*, 6(Journal Article):e25690, 2017.

[65] Jeffrey Demas, Jason Manley, Frank Tejera, Kevin Barber, Hyewon Kim, Francisca Martínez Traub, Brandon Chen, and Alipasha Vaziri. High-speed, cortex-wide volumetric recording of neuroactivity at cellular resolution using light beads microscopy. *Nature Methods*, 18(9):1103–1111, 9 2021. publisher: Nature Publishing Group.

[66] Abbas Kazemipour, Ondrej Novak, Daniel Flickinger, Jonathan S. Marvin, Ahmed S. Abdelfattah, Jonathan King, Philip M. Borden, Jeong Jun Kim, Sarah H. Al-Abdullatif, Parker E. Deal, Evan W. Miller, Eric R. Schreiter, Shaul Druckmann, Karel Svoboda, Loren L. Looger, and Kaspar Podgorski. Kilohertz frame-rate two-photon tomography. *Nature Methods*, 16(8):778–786, 8 2019. publisher: Nature Publishing Group.

[67] Jelena Platisa, Xin Ye, Allison M. Ahrens, Chang Liu, Ichun Anderson Chen, Ian G. Davison, Lei Tian, Vincent A. Pieribone, and Jerry L. Chen. High-speed low-light in vivo two-photon voltage imaging of large neuronal populations. *Nature Methods*, 20(7):1095–1103, 7 2023. publisher: Nature Publishing Group.

[68] Ruth R Sims, Imane Bendifallah, Christiane Grimm, Aysha Mohamed-Lafirdeen, Xiaoyu Lu, François St-Pierre, Eirini Papagiakoumou, and Valentina Emiliani. Scanless two-photon voltage imaging. *Research Square*, 2023.

[69] Timothy D. Weber, Maria V. Moya, Jerome Mertz, and Michael N. Economo. High-speed, multi-z confocal microscopy for voltage imaging in densely labeled neuronal populations. *bioRxiv*, 12 2021. page: 2021.12.10.472140 section: New Results.

[70] Jianglai Wu, Yajie Liang, Shuo Chen, Ching-Lung Hsu, Mariya Chavarha, Stephen W. Evans, Dongqing Shi, Michael Z. Lin, Kevin K. Tsia, and Na Ji. Kilohertz two-photon fluorescence microscopy imaging of neural activity in vivo. *Nature Methods*, 17(3):287–290, 3 2020.

[71] Tong Zhang, Oscar Hernandez, Radosław Chrapkiewicz, Adam Shai, Mark J. Wagner, Yanping Zhang, Cheng-Hsun Wu, Jin Zhong Li, Masatoshi Inoue, Yiyang Gong, Biafra Ahanonu, Hongkui Zeng, Haruhiko Bito, and Mark J. Schnitzer. Kilohertz two-photon brain imaging in awake mice. *Nature Methods*, 16(11):1119–1122, 11 2019. publisher: Nature Publishing Group.

[72] Yoav Adam. All-optical electrophysiology in behaving animals. *Journal of Neuroscience Methods*, 353:109101, 4 2021.

[73] Yoav Adam, Jeong J. Kim, Shan Lou, Yongxin Zhao, Michael E. Xie, Daan Brinks, Hao Wu, Mohammed A. Mostajo-Radji, Simon Kheifets, and Vicente Parot. Voltage imaging and optogenetics reveal behaviour-dependent changes in hippocampal dynamics. *Nature*, 569(7756):413, 2019. publisher: Nature Publishing Group.

[74] W. Akemann, H. Mutoh, A. Perron, Y. K. Park, Y. Iwamoto, and T. Knopfel. Imaging neural circuit dynamics with a voltage-sensitive fluorescent protein. *Journal of neurophysiology*, 108(8):2323–2337, 2012. publisher-place: United States.

[75] Y. Gong, C. Huang, J. Z. Li, B. F. Grewe, Y. Zhang, S. Eismann, and M. J. Schnitzer. High-speed recording of neural spikes in awake mice and flies with a fluorescent voltage sensor. *Science (New York, N.Y.)*, 350(6266):1361–1366, 2015. publisher-place: United States publisher: American Association for the Advancement of Science.

[76] Andrew T Landau, Pojeong Park, J David Wong-Campos, He Tian, Adam E Cohen, and Bernardo L Sabatini. Dendritic branch structure compartmentalizes voltage-dependent calcium influx in cortical layer 2/3 pyramidal cells. *eLife*, 11:e76993, 3 2022. publisher: eLife Sciences Publications, Ltd.

[77] Negin Azimi Hashemi, Amelie C. F. Bergs, Christina Schüler, Anna Rebecca Scheiwe, Wagner Steuer Costa, Maximilian Bach, Jana F. Liewald, and Alexander Gottschalk. Rhodopsin-based voltage imaging tools for use in muscles and neurons of caenorhabditis elegans. *Proceedings of the National Academy of Sciences*, 116(34):17051–17060, 8 2019. publisher: Proceedings of the National Academy of Sciences.

[78] Leonardo Sacconi, Ludovico Silvestri, Esteban C. Rodríguez, Gary A. B. Armstrong, Francesco S. Pavone, Alvin Shrier, and Gil Bub. Khz-rate volumetric voltage imaging of the whole zebrafish heart. *Biophysical Reports*, 2(1):100046, 3 2022.

[79] Kiryl D. Piatkevich, Erica E. Jung, Christoph Straub, Changyang Linghu, Demian Park, Ho-Jun Suk, Daniel R. Hochbaum, Daniel Goodwin, Eftychios Pnevmatikakis, Nikita Pak, Takashi Kawashima, Chao-Tsung Yang, Jeffrey L. Rhoades, Or Shemesh, Shoh Asano, Young-Gyu Yoon, Limor Freifeld, Jessica L. Saulnier, Clemens Riegler, Florian Engert, Thom Hughes, Mikhail Drobizhev, Balint Szabo, Misha B. Ahrens, Steven W. Flavell, Bernardo L. Sabatini, and Edward S. Boyden. A robotic multidimensional directed evolution approach applied to fluorescent voltage reporters. *Nature Chemical Biology*, 14(4):352–360, 4 2018.

[80] Daniel R. Hochbaum, Yongxin Zhao, Samouil L. Farhi, Nathan Klapoetke, Christopher A. Werley, Vikrant Kapoor, Peng Zou, Joel M. Kralj, Dougal Maclaurin, Niklas Smedemark-Margulies, Jessica L. Saulnier, Gabriella L. Boulting, Christoph Straub, Yong Ku Cho, Michael Melkonian, Gane Ka-Shu Wong, D. Jed Harrison, Venkatesh N. Murthy, Bernardo L. Sabatini, Edward S. Boyden, Robert E. Campbell, and Adam E. Cohen. All-optical electrophysiology in mammalian neurons using engineered microbial rhodopsins. *Nature Methods*, 11(8):825–833, 8 2014. number: 8 publisher: Nature Publishing Group.

[81] Yiyang Gong, Mark J. Wagner, Jin Zhong Li, and Mark J. Schnitzer. Imaging neural spiking in brain tissue using fret-opsin protein voltage sensors. *Nature communications*, 5(Journal Article):e3674, 2014. publisher: Nature Publishing Group.

[82] Ahmed S. Abdelfattah, Rosario Valenti, Jihong Zheng, Allan Wong, Kaspar Podgorski, Minoru Koyama, Douglas S. Kim, and Eric R. Schreiter. A general approach to engineer positive-going efret voltage indicators. *Nature Communications*, 11(1):3444, 7 2020. number: 1 publisher: Nature Publishing Group.

[83] Shuzhang Liu, Chang Lin, Yongxian Xu, Huixin Luo, Luxin Peng, Xiangmei Zeng, Huangtao Zheng, Peng R. Chen, and Peng Zou. A far-red hybrid voltage indicator enabled by bioorthogonal engineering of rhodopsin on live neurons. *Nature Chemistry*, 13(5):472–479, 5 2021. number: 5 publisher: Nature Publishing Group.

[84] Miao-Ping Chien, Daan Brinks, Guilherme Testa-Silva, He Tian, F. Phil Brooks, Yoav Adam, William Bloxham, Benjamin Gmeiner, Simon Kheifets, and Adam E. Cohen. Photoactivated voltage imaging in tissue with an archaerhodopsin-derived reporter. *Science Advances*, 7(Journal Article):eabe3216, 2021.

[85] Richard W. Hendler, Richard I. Shrager, and Salil Bose. Theory and procedures for finding a correct kinetic model for the bacteriorhodopsin photocycle. *The Journal of Physical Chemistry B*, 105(16):3319–3328, 4 2001. publisher: American Chemical Society.

[86] Janos K. Lanyi. Bacteriorhodopsin. *Annual Review of Physiology*, 66(1):665–688, 3 2004.

[87] Halil Bayraktar, Alexander P. Fields, Joel M. Kralj, John L. Spudich, Kenneth J. Rothschild, and Adam E. Cohen. Ultrasensitive measurements of microbial rhodopsin photocycles using photochromic fret. *Photochemistry and Photobiology*, 88(1):90–97, 1 2012.

[88] D. Maclaurin, V. Venkatachalam, H. Lee, and A. E. Cohen. Mechanism of voltage-sensitive fluorescence in a microbial rhodopsin. *Proceedings of the National Academy of Sciences*, 110(15):5939–5944, 4 2013.

[89] Joachim Kübel, Manoop Chenchiliyan, Saik Ann Ooi, Emil Gustavsson, Linnéa Isaksson, Valentyna Kuznetsova, Janne A. Ihalainen, Sebastian Westenhoff, and Michał Maj. Transient ir spectroscopy identifies key interactions and unravels new intermediates in the photocycle of a bacterial phytochrome. *Physical Chemistry Chemical Physics*, 22(17):9195–9203, 2020. publisher: Royal Society of Chemistry.

[90] Alfons Penzkofer, Arita Silapetere, and Peter Hegemann. Photocycle dynamics of the archaerhodopsin 3 based fluorescent voltage sensor archon2. *Journal of Photochemistry and Photobiology B: Biology*, 225:112331, 12 2021.

[91] Alfons Penzkofer, Arita Silapetere, and Peter Hegemann. Theoretical investigation of the photocycle dynamics of the archaerhodopsin 3 based fluorescent voltage sensor archon2. *Journal of Photochemistry and Photobiology A: Chemistry*, 437:114366, 3 2023.

[92] Arita Silapetere, Songhwan Hwang, Yusaku Hontani, Rodrigo G. Fernandez Lahore, Jens Balke, Francisco Velazquez Escobar, Martijn Tros, Patrick E. Konold, Rainer Matis, Roberta Croce, Peter J. Walla, Peter Hildebrandt, Ulrike Alexiev, John T. M. Kennis, Han Sun, Tillmann Utesch, and Peter Hegemann. Quasar odyssey: the origin of fluorescence and its voltage sensitivity in microbial rhodopsins. *Nature Communications*, 13(1):5501, 9 2022. number: 1 publisher: Nature Publishing Group.

[93] V. Venkatachalam, D. Brinks, D. Maclaurin, D. Hochbaum, J. Kralj, and A. E. Cohen. Flash memory: photochemical imprinting of neuronal action potentials onto a microbial rhodopsin. *Journal of the American Chemical Society*, 136(6):2529–2537, 2014. publisher-place: United States.

[94] Jennifer H. Hou, Veena Venkatachalam, and Adam E. Cohen. Temporal dynamics of microbial rhodopsin fluorescence reports absolute membrane voltage. *Biophysical journal*, 106(3):639–648, 2014. publisher: Elsevier.

[95] Hunter C. Davis, F. Phil Brooks, J. David Wong-Campos, and Adam E. Cohen. Optical constraints on two-photon voltage imaging. *bioRxiv*, 11 2023. page: 2023.11.18.567441 section: New Results.

[96] Robert R. Birge and Chian-Fan Zhang. Two-photon double resonance spectroscopy of bacteriorhodopsin. assignment of the electronic and dipolar properties of the low-lying

1a*−g-like and 1b*+u-like π, π^* states. *The Journal of Chemical Physics*, 92(12):7178–7195, 6 1990.

[97] Jonathan B. Grimm, Anand K. Muthusamy, Yajie Liang, Timothy A. Brown, William C. Lemon, Ronak Patel, Rongwen Lu, John J. Macklin, Philipp J. Keller, Na Ji, and Luke D. Lavis. A general method to fine-tune fluorophores for live-cell and in vivo imaging. *Nature Methods*, 14(10):987–994, 10 2017. number: 10 publisher: Nature Publishing Group.

[98] Kaspar Podgorski and Gayathri Ranganathan. Brain heating induced by near-infrared lasers during multiphoton microscopy. *Journal of neurophysiology*, 116(3):1012–1023, 2016.

[99] Kriti Charan, Bo Li, Mengran Wang, Charles P Lin, and Chris Xu. Fiber-based tunable repetition rate source for deep tissue two-photon fluorescence microscopy. *Biomedical optics express*, 9(5):2304–2311, 2018.

[100] Chenhong Li. A reliable whole cell clamp technique. *Advances in Physiology Education*, 32:3, 2008.

[101] Glenn J. Goldey, Demetris K. Roumis, Lindsey L. Glickfeld, Aaron M. Kerlin, R. Clay Reid, Vincent Bonin, Dorothy P. Schafer, and Mark L. Andermann. Removable cranial windows for long-term imaging in awake mice. *Nature Protocols*, 9(11):2515–2538–2515–2538, 10 2014.

[102] Dingchang Lin, Xiuyuan Li, Eric Moult, Pojeong Park, Benjamin Tang, Hao Shen, Jonathan B. Grimm, Natalie Falco, Bill Z. Jia, David Baker, Luke D. Lavis, and Adam E. Cohen. Time-tagged ticker tapes for intracellular recordings. *Nature Biotechnology*, 41(5):631–639, 5 2023.

[103] F. Phil Brooks III, Hunter C. Davis, Pojeong Park, Yitong Qi, and Adam E. Cohen. Photophysics-informed two-photon voltage imaging using fret-opsin voltage indicators. *bioRxiv*, 2024.

[104] Vincent Villette, Mariya Chavarha, Ivan K Dimov, Jonathan Bradley, Lagnajeet Pradhan, Benjamin Mathieu, Stephen W Evans, Simon Chamberland, Dongqing Shi, Renzhi Yang, et al. Ultrafast two-photon imaging of a high-gain voltage indicator in awake behaving mice. *Cell*, 179(7):1590–1608, 2019.

[105] Linlin Z. Fan, Doo Kyung Kim, Joshua H. Jennings, He Tian, Peter Y. Wang, Charu Ramakrishnan, Sawyer Randles, Yanjun Sun, Elina Thadhani, Yoon Seok Kim, Sean Quirin, Lisa Giocomo, Adam E. Cohen, and Karl Deisseroth. All-optical physiology resolves a synaptic basis for behavioral timescale plasticity. *Cell*, 186(3):543–559.e19, 2 2023.

[106] Tony Hyun Kim and Mark J Schnitzer. Fluorescence imaging of large-scale neural ensemble dynamics. *Cell*, 185(1):9–41, 2022.

[107] Weijian Zong, Horst A Obenhaus, Emilie R Skytøen, Hanna Eneqvist, Nienke L de Jong, Ruben Vale, Marina R Jorge, May-Britt Moser, and Edvard I Moser. Large-scale two-photon calcium imaging in freely moving mice. *Cell*, 185(7):1240–1256, 2022.

[108] Brian A Wilt, James E Fitzgerald, and Mark J Schnitzer. Photon shot noise limits on optical detection of neuronal spikes and estimation of spike timing. *Biophysical journal*, 104(1):51–62, 2013.

[109] Bernd Kuhn and Christopher J Roome. Primer to voltage imaging with annine dyes and two-photon microscopy. *Frontiers in Cellular Neuroscience*, 13:321, 2019.

[110] Guanghan Meng, Jian Zhong, Qinrong Zhang, Justin S. J. Wong, Jianglai Wu, Kevin K. Tsia, and Na Ji. Ultrafast two-photon fluorescence imaging of cerebral blood circulation in the mouse brain in vivo. *Proceedings of the National Academy of Sciences*, 119(23):e2117346119, 2022. Publisher: Proceedings of the National Academy of Sciences.

[111] Minho Eom, Seungjae Han, Pojeong Park, Gyuri Kim, Eun-Seo Cho, Jueun Sim, Kang-Han Lee, Seonghoon Kim, He Tian, Urs L Böhm, et al. Statistically unbiased prediction enables accurate denoising of voltage imaging data. *Nature Methods*, 20(10):1581–1592, 2023.

[112] Jérôme Lecoq, Michael Oliver, Joshua H Siegle, Natalia Orlova, Peter Ledochowitsch, and Christof Koch. Removing independent noise in systems neuroscience data using deepinterpolation. *Nature methods*, 18(11):1401–1408, 2021.

[113] Jérôme A Lecoq, Kaspar Podgorski, and Benjamin F Grewe. Ai to the rescue of voltage imaging. *Cell Reports Methods*, 3(6), 2023.

[114] Chang Liu, Jelena Platisa, Xin Ye, Allison M Ahrens, Ichun Anderson Chen, Ian G Davison, Vincent A Pieribone, Jerry L Chen, and Lei Tian. Deepvid: A self-supervised deep learning framework for two-photon voltage imaging denoising. In *Optics and the Brain*, pages BTu4C–4. Optica Publishing Group, 2022.

[115] Toyokazu Kimura, Beatriz Ferran, Yuko Tsukahara, Qifan Shang, Suveer Desai, Alessandra Fedoce, David Richard Pimentel, Ivan Luptak, Takeshi Adachi, Yasuo Ido, et al. Production of adeno-associated virus vectors for in vitro and in vivo applications. *Scientific Reports*, 9(1):13601, 2019.

[116] Yi-Lin Huang, Alison S Walker, and Evan W Miller. A photostable silicon rhodamine platform for optical voltage sensing. *Journal of the American Chemical Society*, 137(33):10767–10776, 2015.

[117] He Tian, Hunter C. Davis, J. David Wong-Campos, Pojeong Park, Linlin Z. Fan, Benjamin Gmeiner, Shahinoor Begum, Christopher A. Werley, Gabriel B. Borja, Hansini Upadhyay, Himali Shah, Jane Jacques, Yitong Qi, Vicente Parot, Karl Deisseroth, and Adam E. Cohen.

Video-based pooled screening yields improved far-red genetically encoded voltage indicators. *Nature Methods*, 20(7):1082–1094, 7 2023. publisher: Nature Publishing Group.

[118] Robert R Birge. Two-photon spectroscopy of protein-bound chromophores. *Accounts of Chemical Research*, 19(5):138–146, 1986.

[119] Chris Xu and Watt W Webb. Measurement of two-photon excitation cross sections of molecular fluorophores with data from 690 to 1050 nm. *JOSA B*, 13(3):481–491, 1996.

[120] Tamara Joëlle Buijs and Peter Anthony McNaughton. The role of cold-sensitive ion channels in peripheral thermosensation. *Frontiers in cellular neuroscience*, 14:262, 2020.

[121] TaeKen Kim, Herve Kadji, Andrew J Whalen, Arian Ashourvan, Eugene Freeman, Shelley I Fried, Srinivas Tadigadapa, and Steven J Schiff. Thermal effects on neurons during stimulation of the brain. *Journal of neural engineering*, 19(5):056029, 2022.

[122] Eugene A Kiyatkin. Brain temperature and its role in physiology and pathophysiology: lessons from 20 years of thermorecording. *Temperature*, 6(4):271–333, 2019.

[123] Anh Phong Tran and Steven L Jacques. Modeling voxel-based monte carlo light transport with curved and oblique boundary surfaces. *Journal of Biomedical Optics*, 25(2):025001–025001, 2020.

[124] Mengran Wang, Chunyan Wu, David Sinefeld, Bo Li, Fei Xia, and Chris Xu. Comparing the effective attenuation lengths for long wavelength in vivo imaging of the mouse brain. *Biomedical optics express*, 9(8):3534–3543, 2018.

[125] Yi Shen, Yusuke Nasu, Irene Shkolnikov, Anna Kim, and Robert E Campbell. Engineering genetically encoded fluorescent indicators for imaging of neuronal activity: Progress and prospects. *Neuroscience research*, 152:3–14, 2020.

[126] Adrian Cheng, J Tiago Gonçalves, Peyman Golshani, Katsushi Arisaka, and Carlos Portera-Cailliau. Simultaneous two-photon calcium imaging at different depths with spatiotemporal multiplexing. *Nature methods*, 8(2):139–142, 2011.

[127] Giulia Faini, Dimitrii Tanese, Clément Molinier, Cécile Telliez, Massilia Hamdani, Francois Blot, Christophe Tourain, Vincent de Sars, Filippo Del Bene, Benoît C Forget, et al. Ultrafast light targeting for high-throughput precise control of neuronal networks. *Nature Communications*, 14(1):1888, 2023.

[128] Gerald Donnert, Christian Eggeling, and Stefan W Hell. Major signal increase in fluorescence microscopy through dark-state relaxation. *Nature methods*, 4(1):81–86, 2007.

[129] Na Ji, Jeffrey C Magee, and Eric Betzig. High-speed, low-photodamage nonlinear imaging using passive pulse splitters. *Nature methods*, 5(2):197–202, 2008.

[130] Blox Bloxham, Daan Brinks, Simon Kheifets, and Adam E Cohen. Linearly polarized excitation enhances signals from fluorescent voltage indicators. *Biophysical Journal*, 120(23):5333–5342, 2021.

[131] Josef Lazar, Alexey Bondar, Stepan Timr, and Stuart J Firestein. Two-photon polarization microscopy reveals protein structure and function. *Nature methods*, 8(8):684–690, 2011.

[132] Mauro Pulin, Kilian E Stockhausen, Olivia A Masseck, Martin Kubitschke, Björn Busse, J Simon Wiegert, and Thomas G Oertner. Orthogonally-polarized excitation for improved two-photon and second-harmonic-generation microscopy, applied to neurotransmitter imaging with gpcr-based sensors. *Biomedical Optics Express*, 13(2):777–790, 2022.

[133] E Kelly Buchanan, Ian Kinsella, Ding Zhou, Rong Zhu, Pengcheng Zhou, Felipe Gerhard, John Ferrante, Ying Ma, Sharon H Kim, Mohammed A Shaik, et al. Penalized matrix decomposition for denoising, compression, and improved demixing of functional imaging data. *BioRxiv*, page 334706, 2018.

[134] Changjia Cai, Johannes Friedrich, Amrita Singh, M Hossein Eybposh, Eftychios A Pnevmatikakis, Kaspar Podgorski, and Andrea Giovannucci. Volpy: Automated and scalable analysis pipelines for voltage imaging datasets. *PLoS computational biology*, 17(4):e1008806, 2021.

[135] Eran A Mukamel, Axel Nimmerjahn, and Mark J Schnitzer. Automated analysis of cellular signals from large-scale calcium imaging data. *Neuron*, 63(6):747–760, 2009.

[136] Eftychios A Pnevmatikakis, Daniel Soudry, Yuanjun Gao, Timothy A Machado, Josh Merel, David Pfau, Thomas Reardon, Yu Mu, Clay Lacefield, Weijian Yang, et al. Simultaneous denoising, deconvolution, and demixing of calcium imaging data. *Neuron*, 89(2):285–299, 2016.

[137] Michael E. Xie, Yoav Adam, Linlin Z. Fan, Urs L. Böhm, Ian Kinsella, Ding Zhou, Marton Rozsa, Amrita Singh, Karel Svoboda, Liam Paninski, and Adam E. Cohen. High-fidelity estimates of spikes and subthreshold waveforms from 1-photon voltage imaging in vivo. *Cell Reports*, 35(1):108954, 4 2021.

[138] Johannes Friedrich, Weijian Yang, Daniel Soudry, Yu Mu, Misha B Ahrens, Rafael Yuste, Darcy S Peterka, and Liam Paninski. Multi-scale approaches for high-speed imaging and analysis of large neural populations. *PLoS computational biology*, 13(8):e1005685, 2017.

[139] Arthur Edelstein, Nenad Amodaj, Karl Hoover, Ron Vale, and Nico Stuurman. Computer control of microscopes using μmanager. *Current Protocols in Molecular Biology*, 92(1):14.20.1–14.20.17, 2010.

[140] Arthur D Edelstein, Mark A Tsuchida, Nenad Amodaj, Henry Pinkard, Ronald D Vale, and Nico Stuurman. Advanced methods of microscope control using μmanager software. *Journal of biological methods*, 1(2), 2014.

[141] Fabian F. Voigt, Jerry L. Chen, Roland Krueppel, and Fritjof Helmchen. A modular two-photon microscope for simultaneous imaging of distant cortical areas in vivo. In *Multiphoton Microscopy in the Biomedical Sciences XV*, volume 9329, pages 217–223. SPIE, March 2015.

[142] Dmitriy Aronov and David W Tank. Engagement of neural circuits underlying 2d spatial navigation in a rodent virtual reality system. *Neuron*, 84(2):442–456, 2014.

[143] Adam E. Cohen and Veena Venkatachalam. Bringing bioelectricity to light. *Annual Review of Biophysics*, 43(1):211–232, 5 2014.

[144] H. Grundfest. Bioelectric potentials. *Annual Review of Physiology*, 2(Volume 2, 1940):213–242, 3 1940. publisher: Annual Reviews.

[145] Yi Han, Junqi Yang, Yuan Li, Yu Chen, Huixia Ren, Ran Ding, Weiran Qian, Keyuan Ren, Beichen Xie, Mengying Deng, Yinghan Xiao, Jun Chu, and Peng Zou. Bright and sensitive red voltage indicators for imaging action potentials in brain slices and pancreatic islets. *bioRxiv*, 12 2022. page: 2022.12.01.518652 section: New Results.

[146] Hillel Ori, Marc Duque, Rebecca Frank Hayward, Colin Scheibner, He Tian, Gloria Ortiz, Vincenzo Vitelli, and Adam E. Cohen. Observation of topological action potentials in engineered tissues. *Nature Physics*, 19(2):290–296, 2 2023. publisher: Nature Publishing Group.

[147] Yuriy Shymkiv and Rafael Yuste. Aberration-free holographic microscope for simultaneous imaging and stimulation of neuronal populations. *Optics Express*, 31(20):33461–33474, 9 2023. publisher: Optica Publishing Group.

[148] Marco Canepari, Peter Saggau, and Dejan Zecevic. Combined voltage and calcium imaging and signal calibration. In Marco Canepari and Dejan Zecevic, editors, *Membrane Potential Imaging in the Nervous System: Methods and Applications*, pages 43–52. Springer, New York, NY, 2011.

[149] Julia R Lazzari-Dean, Anneliese MM Gest, and Evan W Miller. Optical estimation of absolute membrane potential using fluorescence lifetime imaging. *Elife*, 8:e44522, 2019.

[150] Anneliese M. M. Gest, Susanna K. Yaeger-Weiss, Julia R. Lazzari-Dean, and Evan W. Miller. Chapter twelve - voltagefluor dyes and fluorescence lifetime imaging for optical measurement of membrane potential. In Daniel L. Minor and Henry M. Colecraft, editors, *Methods in Enzymology*, volume 653 of *Ion Channels: Channel Production and Optical Methods*, pages 267–293. Academic Press, 1 2021. DOI: 10.1016/bs.mie.2021.02.009.

[151] R. S. Bedlack, M.-d Wei, and L. M. Loew. Localized membrane depolarizations and localized calcium influx during electric field-guided neurite growth. *Neuron*, 9(3):393–403, 9 1992. publisher: Elsevier PMID: 1524823.

[152] Richard S. Bedlack, Mei-de Wei, Stephen H. Fox, Eitan Gross, and Leslie M. Loew. Distinct electric potentials in soma and neurite membranes. *Neuron*, 13(5):1187–1193, 11 1994.

[153] Chang Xu and Leslie M. Loew. The effect of asymmetric surface potentials on the intramembrane electric field measured with voltage-sensitive dyes. *Biophysical Journal*, 84(4):2768–2780, 4 2003.

[154] A Bullen and P Saggau. High-speed, random-access fluorescence microscopy: Ii. fast quantitative measurements with voltage-sensitive dyes. *Biophysical Journal*, 76(4):2272–2287, 4 1999. PMID: 10096922 PMCID: PMC1300200.

[155] Stephen B. Knisley, Robert K. Justice, Wei Kong, and Philip L. Johnson. Ratiometry of transmembrane voltage-sensitive fluorescent dye emission in hearts. *American Journal of Physiology-Heart and Circulatory Physiology*, 279(3):H1421–H1433, 9 2000. publisher: American Physiological Society.

[156] Jing Zhang, Robert M. Davidson, Mei-de Wei, and Leslie M. Loew. Membrane electric properties by combined patch clamp and fluorescence ratio imaging in single neurons. *Biophysical Journal*, 74(1):48–53, 1 1998.

[157] Adam J. Bowman, Cheng Huang, Mark J. Schnitzer, and Mark A. Kasevich. Wide-field fluorescence lifetime imaging of neuron spiking and subthreshold activity in vivo. *Science*, 380(6651):1270–1275, 6 2023. publisher: American Association for the Advancement of Science.

[158] Micah S Siegel and Ehud Y Isacoff. A genetically encoded optical probe of membrane voltage. *Neuron*, 19(4):735–741, 10 1997.

[159] B. J. Baker, H. Lee, V. A. Pieribone, L. B. Cohen, E. Y. Isacoff, T. Knopfel, and E. K. Kosmidis. Three fluorescent protein voltage sensors exhibit low plasma membrane expression in mammalian cells. *Journal of Neuroscience Methods*, 161(1):32–38, 3 2007.

[160] Shuzhang Liu, Jing Ling, Peng Chen, Chang Cao, Luxin Peng, Yuan Zhang, Guangshen Ji, Yingna Guo, Peng R. Chen, Peng Zou, and Zhixing Chen. Orange/far-red hybrid voltage indicators with reduced phototoxicity enable reliable long-term imaging in neurons and cardiomyocytes. *Proceedings of the National Academy of Sciences*, 120(34):e2306950120, 2023. Publisher: Proceedings of the National Academy of Sciences.

[161] Jonathan B. Grimm, Liangqi Xie, Jason C. Casler, Ronak Patel, Ariana N. Tkachuk, Natalie Falco, Heejun Choi, Jennifer Lippincott-Schwartz, Timothy A. Brown, Benjamin S. Glick,

Zhe Liu, and Luke D. Lavis. A general method to improve fluorophores using deuterated auxochromes. *JACS Au*, 1(5):690–696, 2021.

[162] Jihwan Lee, Zhuohe Liu, Peter H. Suzuki, John F. Ahrens, Shujuan Lai, Xiaoyu Lu, Sihui Guan, and François St-Pierre. Versatile phenotype-activated cell sorting. *Science Advances*, 6(43):eabb7438, 2020.

[163] Samir Saidi and Matthew Shtrahman. Evaluation of compact pulsed lasers for two-photon microscopy using a simple method for measuring two-photon excitation efficiency. *Neurophotonics*, 10(4):044303, 2023.

[164] Thulasi Srinivasan and Murat Yildirim. Advances in ultrafast fiber lasers for multiphoton microscopy in neuroscience. *Photonics*, 10(12):1307, 2023. Number: 12 Publisher: Multidisciplinary Digital Publishing Institute.

[165] Yaroslav Halchenko, John T. Wodder II, Horea Christian, Satrajit Ghosh, Saksham Sharda, Dorota Jarecka, Cody Baker, Daniel Chiquito, Ben Dichter, Jacob Nesbitt, Kabilar Gunalan, Mary Elise Dedicke, Kyle Meyer, Mike VanDenburgh, Dan LaManna, Mike Grauer, Jonny Saunders, Garrett Michael Flynn, Julia Sprenger, LGTM Migrator, Michał Górny, and Nicole Lo. dandi/dandi-cli: 0.61.2, March 2024.

[166] Mikhail Drobizhev, Nikolay S Makarov, Shane E Tillo, Thomas E Hughes, and Aleksander Rebane. Two-photon absorption properties of fluorescent proteins. *Nature methods*, 8(5):393–399, 2011.

[167] Vera Bandmann, Ann Schirin Mirsanaye, Johanna Schäfer, Gerhard Thiel, Thomas Holstein, and Melanie Mikosch-Wersching. Membrane capacitance recordings resolve dynamics and complexity of receptor-mediated endocytosis in Wnt signalling. *Scientific Reports*, 9(1):12999, September 2019. Number: 1 Publisher: Nature Publishing Group.